THEORETICAL AND COMPUTATIONAL STUDIES OF THE MECHANICAL STRENGTH AND FRACTURE TOUGHNESS OF ADHESIVELY BONDED JOINTS AND POLYMER NANOCLAY COMPOSITES

A Thesis
Submitted to the Graduate Faculty
of the
North Dakota State University
of Agriculture and Applied Science

By

Uraching Chowdhury

In Partial Fulfillment of the Requirements
for the Degree of
MASTER OF SCIENCE

Major Department:
Mechanical Engineering

November 2018

Fargo, North Dakota

North Dakota State University
Graduate School

Title

Theoretical and Computational Studies of the Mechanical Strength and Fracture Toughness of Adhesively Bonded Joints and Polymer Nanoclay Composites

By

Uraching Chowdhury

The Supervisory Committee certifies that this ***disquisition*** complies with North Dakota State University's regulations and meets the accepted standards for the degree of

MASTER OF SCIENCE

SUPERVISORY COMMITTEE:

Dr. Xiangfa Wu
Chair

Dr. Long Jiang

Dr. AKM Bashir Khoda

Dr. Xinnan Wang

Approved:

12/07/2018
Date

Dr. Alan R. Kallmeyer
Department Chair

ABSTRACT

Increasing use of adhesively bonded joints (ABJs) and polymer nanoclay composites (PNCs) in modern vehicles and other industrial sectors has deeply shaped the design and manufacturing of advanced materials and structures for better mechanical stiffness, durability, and fracture toughness.

(1) A nonlinear fracture model is formulated for accurately extracting the fracture toughness of ABJs with large plastic deformations and springback and further validated by ABJ fracture data available in the literature.

(2) Cohesive zone model (CZM) is integrated into finite element method (FEM) to simulate the debonding process of ABJs at varying adhesive layer geometries and material properties.

(3) CZM is further utilized for exploring the failure mechanisms of PNCs under external loading at varying PNC geometries and material properties.

The present studies can be useful for effective and accurate data reduction and further improving the design and manufacturing of ABJs and PNCs with tailorable mechanical properties.

ACKNOWLEDGEMENTS

I would like to express my sincere thanks to my advisor, Dr. Xiangfa Wu, whose knowledge, expertise and guidance were crucial to my thesis research at NDSU. Dr. Wu's in-depth understanding and scientific seriousness in this field, timely response and constructive criticisms have added considerably to my thesis work. I would also like to give my sincere gratitude to the rest members (Dr. Long Jiang, Dr. AKM Bashir Khoda, and Dr. Xinnan Wang) of the supervisory committee of my graduate study for their time and valuable assistance during my graduate study at NDSU.

I was obliged to have the financial supports from the Department of Mechanical Engineering at NDSU and the US DOE. Without these supports, the research of this thesis would not be finished.

Finally, I would like to recall the support and confidence that my parents offered to me in pursuit of my Master of Science Degree at NDSU.

TABLE OF CONTENTS

LIST OF TABLES

LIST OF FIGURES

1. INTRODUCTION

The development of modern aerospace, aeronautical and ground vehicles eagerly demands innovative materials and structures of low-cost, lightweight, and high load-carrying capacities (e.g., high mechanical strength, stiffness, fracture toughness and fatigue durability, etc.) and related material/structural design and analysis methodologies. In the last two decades, two fast developing trends in materials and structures can be clearly identified, i.e., the increasing use of adhesively bonded joints (ABJs) in various aerospace and ground vehicles and the integration of high-performance polymer nanoclay composites (PNCs) in broad industrial sectors. The use of these novel ABJs and PNCs requires new material and structure design strategies and structural analysis methods for reliable design and accurate prediction of their mechanical performance and lifetime.

The research of this thesis was formulated to address the fracture toughness and failure mechanisms of ABJs made of adhesively bonded thin ductile metal adherends (i.e., mild steels and aluminum alloys) and PNCs via detailed theoretical fracture model development and cohesive-zone model (CZM) based finite element analysis (FEA). Specifically, the layout of the thesis work is tri-folded: (i) Formulation of a novel nonlinear elastoplastic fracture model to extract the fracture toughness of ABJs with large plastic deformations and springback, (ii) CZM-based FEA for determination of the characteristic load- displacement diagrams of ABJs at varying geometries and material properties of the adherends and adhesive layers, (iii) CZM-based computational micromechanics modeling of the full-range effective load-carrying performance and exploration of the failure mechanisms in PNCs. Below briefly introduce the three topics to be investigated in the present work.

Firstly, ABJs of various configurations have been integrated into broad structures due to their unique technological advantages including the low material and labor costs, high joining strength and fatigue durability, efficient load-transferring capability, and noticeable weight reduction of the joining parts. A number of linearly elastic fracture mechanics (LEFM) models have been developed in the literature for the analysis of the failure of ABJs where small scale yielding was assumed. Therein, the fracture of ABJs is treated as a fracture event only relevant to its local stress state, i.e., the *K*-controlled field, independent of the global deformation of the ABJs. Such LEFM treatment of ABJs can only hold for the failure analysis of ABJs made of adhesively bonded thick adherend, where no significant plastic deformation exists in the adherends and the fracture energy is dissipated by the adhesive layers.

With the increasing use of ABJs made of adhesively bonded thin ductile metal adherends in ground vehicles, experimental fracture studies of such ABJs involving large plastic deformations combined with substantial springback have been performed (for instance, Thouless et al., 1998). In order to extract the fracture toughness of such ABJs, several fracture models have been reported in the literature with various extents of deliberation (Thouless et al., 1998; Kinloch and Williams, 1999). Yet, these fracture mechanics models of ABJs have their intrinsic limitations as follows. First, these models oversimplify the ductile materials (i.e., mild steels and aluminum alloys) as simple power-law nonlinear elastic materials, while these ductile materials can be well modeled as elastoplastic solids following a power-law strain-hardening law (Pardoen et al., 2005). Second, these models simply ignore the significant springback of the specimen after fracture, which lead to the curvature at the maximum fracture bending moment noticeably smaller than the actual one. Third, to compensate the curvature loss due to the above improper assumptions,

artificial root rotation is introduced into the fracture models which complicate the modeling process.

Based on above analysis of the existing fracture mechanics models and the steady fracture tests of ABJs with large plastic deformations and springback (Thouless et al., 1998; Kinloch and Williams, 1999), the present studies establish an innovative nonlinear elastoplastic fracture models of these ABJs. During the process, the ductile metal adherends are modeled as elastoplastic solids following a power-law strain-hardening law (Pardoen et al., 2005); the large plastic deformations and noticeable springback of the ABJ adherends are taken into account to accurately determine the curvature at the maximum bending moment. As a result, an improved fracture toughness formula of the ABJs is formulated for accurate data reduction. The present theoretical modeling is validated by the experimental fracture results and the literature models. In addition, detailed numerical scaling analysis is made to explore the effects of geometries and material properties of the adherends on the extracted fracture toughness, plastic deformations and springback of the ABJs.

Secondly, a variety of analytical and computational ABJ models are available in the literature for stress analysis of ABJs with different extents of deliberation. Among others, Dr. Xiangfa Wu's research group at the North Dakota State University (NDSU) has successfully formulated a robust, high-efficient semi-analytical stress-function variational method (Wu and Jensen, 2011; Wu and Zhao, 2013), which is capable of accurately determining the interfacial stresses in ABJs and validated by detailed FEA. The main advantages of Wu's stress-function variational method are: The shear and peeling stresses on each bonding line of the ABJs are assumed to be two independent stress functions to be determined via triggering the principle of the minimum complementary strain energy of the joint; the shear stresses on the bonding lines can automatically satisfy the free shear-stress conditions at the ABJ edges, which were typically

broken in many analytic ABJ models in the literature including the classic ABJ models by Volkersen (1938), Goland and Reissner (1994), Delale et al. (1981). Nevertheless, all these ABJ models are unable to predict the crack initiation and propagation in ABJs. Thus, the present study is further to introduce CZM-based finite element method (FEM) to computationally simulate the crack initiation and propagation in ABJs based on commercially available FEA software package (ANSYS®), in which a linear cohesive zone model (CZM) is utilized to control the node release scheme in modeling the debonding growth in ABJs. In addition, computational scaling analysis is firstly performed for determination of a spectrum of the full-range characteristic load-displacement diagrams of ABJs with varying geometries and material properties of the adherends and adhesive layers. The computational results are useful for ABJ design and exploration of ABJ failure mechanism.

Thirdly, since Toyota successfully produced the pioneering high-performance PNCs in 1980s (Fukushima et al., 1998), the research of PNCs for controlled mechanical properties has become a focus of experimental and theoretical investigations in the community of materials science and engineering. The main interest of PNC research is to understand the mechanisms and effects of the exfoliation extent, volume fracture and nanoclay particle alignment on the stiffness, strength and fracture toughness of PNCs. A number of theoretical and computational micromechanics models has been formulated to determine the effective stiffness of PNCs, in which the distribution of the aligned clay nanoparticles is assumed to follow the stack and stagger models, respectively. Recently, Dr. Xiangfa Wu's research group at NDSU has performed a successful computational micromechanics modeling to investigate the effects of PNC processing parameters (i.e., clay nanoparticle aspect ratio and volume fraction) on the effective stiffness and the full-range effective stress-stain relationship of the PNCs, in which the polymer matrix is assumed to

be ideally elastoplastic solid, the clay nanoparticles are assumed to be linearly elastic solid, and the distribution of the clay nanoparticles follows the stack and stagger models, respectively (Rahman and Wu, 2017). Yet, the above computational micromechanics model is unable to determine the failure mechanisms and the failure process of PNCs. Therefore, in the present study, the above CZM-based FEM is further used to predict the full-range effective stress-strain relationship involving clay nanoparticle debonding. The stack and stagger models are used to approach the ideal aligned clay nanoparticle distribution. The effects of the PNC processing parameters such as the clay nanoparticle aspect ratio, volume fraction, interfacial debonding toughness (fracture toughness), edge roundness, etc. on the effective stress-strain relationship are computationally investigated. The obtained numerical results can be used for understanding the toughening and failure mechanisms of PNCs and optimization of the process parameters for controlled mechanical properties of PNCs.

The present theoretical and computational studies provide the rational understandings of the fracture of ABJs with large plastic deformations and springback, the entire failure process of ABJs and PNCs, which are particularly useful for data reduction of ABJ fracture tests to extract the accurate fracture toughness, the full-range load-displacement diagrams of ABJs for ABJ design, optimization and failure analysis, and the full-range effective stress-strain relations for controlled processing of PNCs for optimal mechanical properties. The present research also opens new research directions and strategies for the improvements of ABJ and PNC design and optimization for better mechanical behaviors.

2. LITERATURE REVIEW

2.1. Adhesively Bonded Joints

2.1.1. Adhesively Bonded Joints Technology

Adhesively bonded joints (ABJs) have found broad applications including bonding and connecting thin structural parts, repairing surface defects, increasing bonding strength and finally enhancing fatigue durability (Menard, 2005; Park et al., 2010; David & Bond, 1999; Higgins, 2000; Grant et el., 2009; Worlton, 1961). These ABJs have significant applications in aerospace, automobile, flexible electronics, and composites (Figs. 2.1, 2.2 and 2.3) due to their excellent compact design, mechanical durability and efficient load transfer abilities.

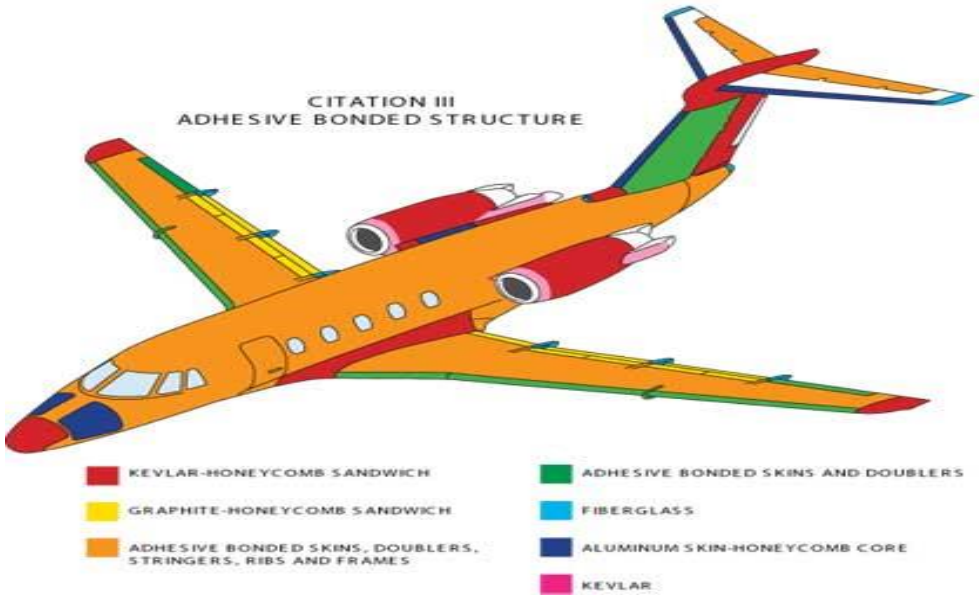

Figure 2.1. ABJs in modern aircraft (Worlton, 1961)

A number of robust joint models of ABJs have been formulated for typical stress-strength analysis (Da Silva et al., 2009; Da Silva et al., 2009; Wu & Jenson, 2014; Wu et al., 2014). The bonding strength and fatigue durability are considered as the two most dominating factors of the mechanical performance of ABJs. When subjected to an external loading, ABJs tend to show

complicated stress-strain state due to the unusual complex geometries and mismatch of the material properties of the adhesives and adherends at a localized area. Therefore, in-depth analysis and understanding of the stress state and strength of the ABJs is critically important to a better rational structural design and more predictable and reliable mechanical performance of ABJs. A significant number of efforts has been made till now to explore the toughening and failure mechanisms of ABJs and related composite materials (Wu et al., 2002; Johnson, 1988; Mittal, 2012; Wu & Yarin, 2013).

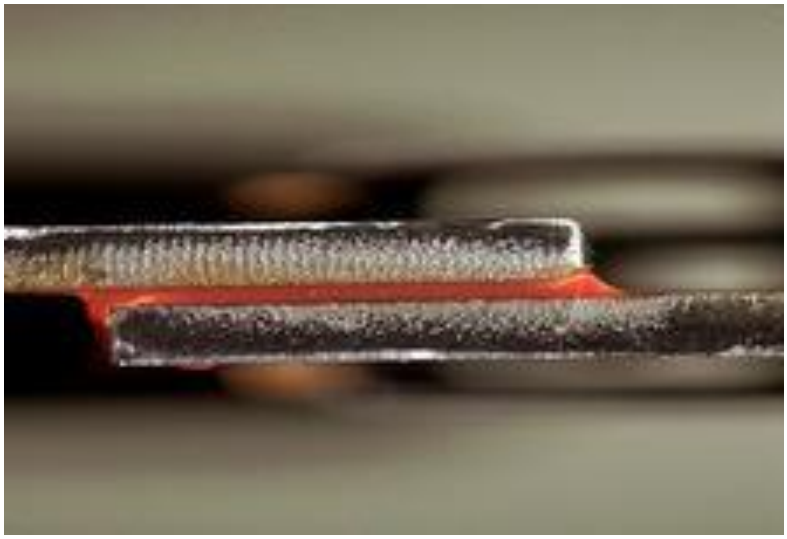

Figure 2.2. Adhesively bonded single-lap joint (online image)

One of the purposes of this thesis is to study the applicability of the ABJ models to determine the fracture toughness of ABJs with large plastic deformations and afterward springback. It is noted that, the purpose herein is not to formulate a new ABJ model to study the coupling between the fracture process and plastic deformations of the adherends. Rather, the key focus is to formulate an innovative ABJ model to explore the effects of the coupling between the adhesive layer and the plastic deformations of the thin-layered ductile metal adherends (e.g., mild steels and aluminum alloys). Therefore, the debonding failure of different ABJ geometries with

identical adhesive layers can be predicted. The applicability of the proposed model has been validated by comparing the model results with those experimental data available in the literature.

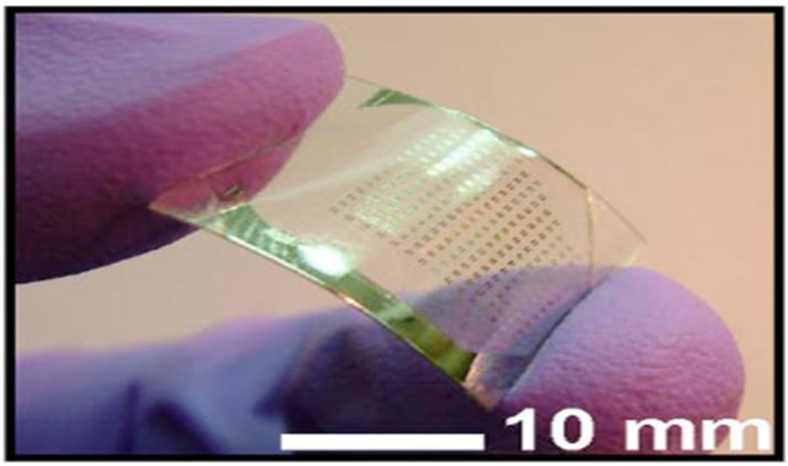

Figure 2.3. Flexible electronics (Menard, 2005)

In addition to the theoretical ABJ fracture model developed in this thesis work, a detailed cohesive-zone-model (CZM) based finite element analysis (FEA) was made to extract the characteristic full-range load-displacement behaviors of ABJs during the debonding process. In the computational process, it is assumed that the role of the adhesive layer is to provide the peeling and shearing separation law (i.e., cohesive law) between two adherends of the ABJs. The aim of this computational study is to provide the general guidelines of the influence of material geometries and properties on the debonding initiation and propagation in ABJs so that the failure mechanisms and full-range debonding failure process of ABJs can be predicted accurately.

2.1.2. Current Understanding

Considering the influence of ABJs in structural design, application and modification, many research studies have been performed on determining the fracture toughness of ABJs. Figs. 2.4 and 2.5 illustrates an example of debonded surface of adhesively bonded metallic joints (ABMJs)

under loading and the typical failure modes of ABJs respectively. Significant advances have been made on the fracture mechanics of layered geometries including those close to ABJs. One of such studies performed by Hutchinson and Suo (1990) and Hutchinson and Suo (1991), where element beam theory has been extensively used in determining the energy release rate of crack growth including crack initiation and propagation. The influence of the deformations at the crack tip on the fracture analysis of mixed-mode cracks was studied by Wang and Qiao (2005).

Figure 2.4. Failure surface of ABMJs under loading (Hafiz et al., 2010)

Most of the crack problems in fracture mechanics studied in the literature are based on linear elastic fracture mechanics (LEFM), where small scale yielding (SSY) assumption has been made at the crack tip. The fracture phenomenon associated with large plastic deformations is extremely complicated and is still not well resolved in both experimental and theoretical studies. In the process of measuring the fracture toughness of ABJs made of thin-layered metals, significant plastic deformations and afterward springback exhibit in the ductile metal adherends, which contribute substantially to the energy dissipation and needs to be considered (Thouless et al., 1998; Williams, 1998). Li and Lee et al. (2016) formulated an analytical fracture model of a double cantilever beam made of a power-law nonlinear elastic material for calculating the energy release

rate. Yet, this model shows the obvious deficiency in treating realistic fracture problems of ductile metal ABJs with large plastic deformations and afterward elastic springback due to the crack growth induced elastoplastic unloading.

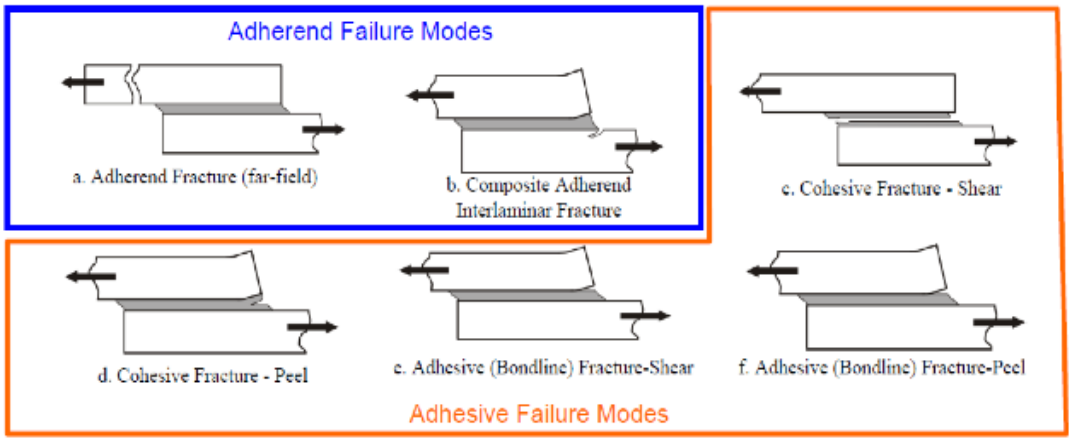

Figure 2.5. Typical failure modes of adhesively bonded joints (ABJs) (Heslehurst and Hart-Smith, 2002)

Though material plasticity has been considered in the adhesive layer properties, the fracture toughness of ABJs still has significant deviation due to the model simplification that the adherends are treated as linearly elastic solids. When the thickness of the adherends is less than a critical value approximated by Kim and Aravas (1988) as

$$h_c \approx 6E\Gamma/{Y_0}^2 , \tag{2.1}$$

where E is the elastic modulus, Y_0 is the yield strength and Γ is the fracture toughness of the adherends. A theoretical analysis along with the detailed finite element analysis is used in their study to examine the stress and deformation behaviors near the crack tip of an interfacial crack.

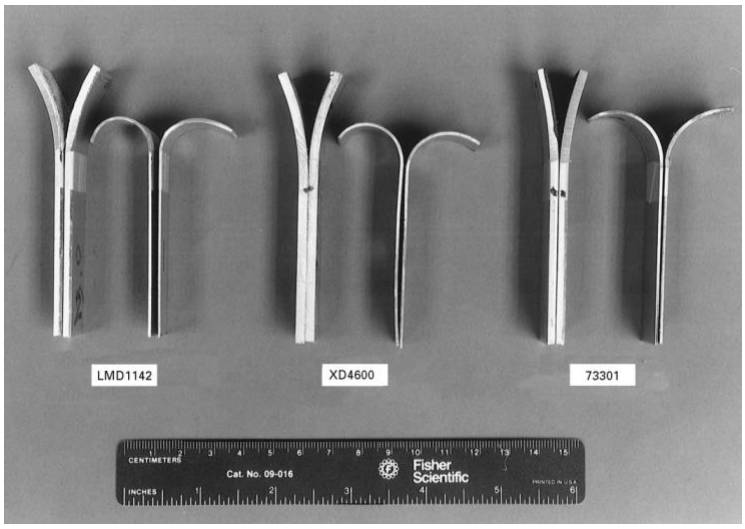

Figure 2.6. Experimental set up of an impact fracture test of ABJs (Thouless et al., 1998)

An energy balance is also used to correlate an experimental peel force to the specific fracture energy. When the adherend thickness h is below h_c, the ABJs will start to deform plastically prior to the fracture initiation in the joints (Kim & Kim, 1988). Thouless et al. (1998) performed an experimental study for determining the fracture toughness of adhesively bonded metal layers where symmetric configuration of fracture specimens had been used and the experimental set up and materials dimensions can be presented in Figs. 2.6 and 2.7 respectively. Identical aluminum alloy and mild steel sheets have been used as the ductile adherends. The fracture toughness of the ABJs was determined as

$$\Gamma = \frac{An(h)^{n+2}}{2^n(n+2)(n+1)}\left(\frac{1}{{R_1}^{n+1}} + \frac{1}{{R_2}^{n+1}}\right), \tag{2.2}$$

In the above expression, $R_1$and R_2 are respectively the measured radii of curvature of the two post-fracture arms of the specimen, h is the thickness of each arm, and A and n are the material constants of the power-law nonlinear elastic model:

$$\sigma = A\varepsilon^n \,, \tag{2.3}$$

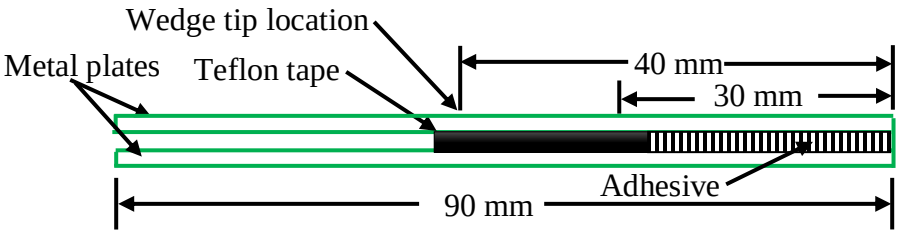

Figure 2.7. Schematic of the ABJ specimen used for the fracture test by Thouless et al. (1998)

Reviewing Thouless et al. (1998), the fracture toughness measured from (2.2) shows only the half of the actual experimental results by comparison with those obtained in other testing methods. Such a significant deviation of the fracture toughness could be attributed reasonably to the two potential factors (Yang et al., 2000; Yang et al., 1999; Kinloch & Williams, 1998; Kinloch & Williams, 1999; Yang & Thouless, 1999). Firstly, the significant elastic springback has not been considered in Thouless's model as the material model adopted in Thouless's data analysis is a nonlinear elastic model, and hence the radii of curvature measured from the post-fractured specimens are larger than the actual ones, at which debonding initiates. Secondly, due to the large elastic springback, the actual strain energy should be higher than that calculated without springback.

In addition, several computational studies have been performed on determining the mechanical properties and failure mechanism of bonded joints and ABJs. For instance, for the purpose of precise prediction of the mixed-mode crack growth in layered materials, finite element methods (FEMs) have been used by Schapery & Davidson (1990), Davidson et al. (1995), and Sundararaman & Davidson (1997), where crack tip elements have been integrated into FEM with a significant number of nodes and elements. Additionally, Wu and Jenson (2011) and Wu and

Zhao (2013) formulated a high-efficient semi-analytic stress-functional variational method for the interfacial stress analysis of bonded joints and ABJs under combined thermal and mechanical loads. The stress field predicted by this semi-analysis method has been validated by FEA. Although these models can predict the accurate interfacial shear and normal stresses which are responsible for the debonding failure of ABJs, accurate force-displacement behavior of the entire ABJs during the debonding process is still beyond the capabilities of these models. Therefore, CZM-based FEA of ABJs is needed in the present study in order to explore the debonding ignition and growth in ABJs and related full-range force-displacement behavior of the ABJs during the entire debonding failure process. As a matter of fact, fracture in ABJs is a common phenomenon and it is extremely challenging to conduct the nonlinear analysis within the framework of the conventional LEFM. CZM is regarded as the unique, broadly accepted, powerful model for computational analyses of fracture and crack growth in solid materials nowadays, which has been utilized for the explanation of the failure phenomena across the crack process zone with substantial plastic deformations. The applications of CZM-based FEA for determining the nonlinear failure analyses of ABJs will be further addressed in Section 2.3 and Chapter 4.

2.1.3. Outstanding Problems in Mechanical Strength and Fracture Toughness of ABJs

To date, intensive experimental, theoretical and computational investigations have been conducted for exploring the mechanical strength and fracture toughness of ABJs. By manipulating the loading and geometries of the ABJs, several types of structural ABJs can be identified and broadly structured in various industrial sectors as shown in Fig. 2.8.

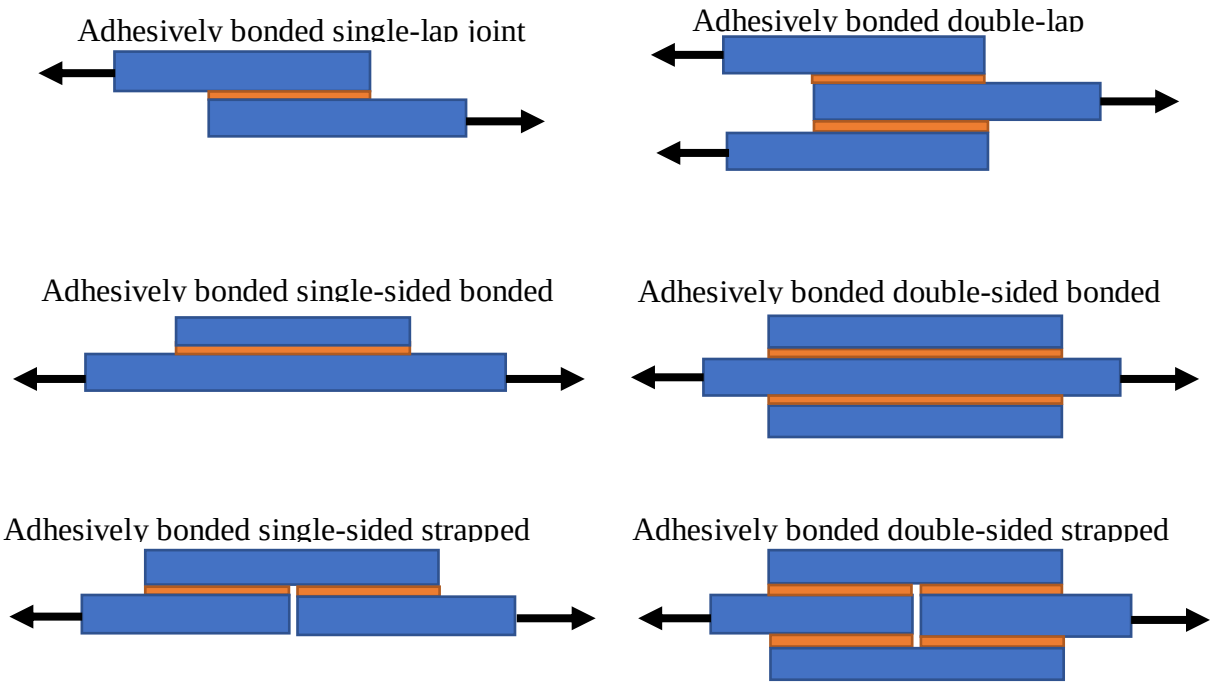

Figure 2.8. Examples of adhesively bonded joints (ABJs) types

In chapter 3, the present elastoplastic modeling of the debonding of ABJs is to reanalyze the disagreement between experimental results and the existing theoretical models available in the literature and then further take into account the elastoplastic material model with large plastic deformations and afterward springback. The radii of the curvature of the post-fractured arms are measured after springback, which are further utilized to determine the radii of the curvature of the arms at the instant of bending-moment driven bonding by establishing a nonlinear moment-curvature relation. Furthermore, the strain energy associated with the nonlinear bending process is calculated in three separate considerations, i.e., the linearly elastic portion, the strain-hardening portion, and the unloading portion. This model is used to compute the fracture toughness of ABJs with large plastic deformations based on the existing experimental data available in the literature (Thouless et al., 1998). Detailed numerical scaling analysis is further made to examine the effects

of Young's modulus, strain hardening index and geometries on the springback of the ABJ arms. Discussions of the present model and comparison with the existing models are further made.

In chapter 4, CZM-based FEM is used to predict the mechanical properties and failure behaviors of the ABJs. To demonstrate this process, adhesively bonded single-sided strap joints (ABSSSJs) with two different adherends are considered. Due to the symmetries of the ABJ structures and external loads, the entire simulation process was conducted only on the right half symmetric portion of the entire ABJ. Detailed computational scaling analysis indicates a major advantage of the proposed CZM-based FEM model for predicting the full-range debonding process of bonded joints and ABJs accurately.

2.2. Polymer Nanoclay Composites

2.2.1. Nanoclay in Polymer Composites

Polymeric matrix composites (PMCs) made of polymeric resins reinforced with organically modified montmorillonite (called nanoclay) have become a matter of serious interests in academia and industry (as for example, see Fig. 2.9) due to the fact that the addition of tiny amount of nanoclay can significantly increase the mechanical properties of the resulting polymer nanoclay composites (PNCs). Reinforcement at nanoscale has several advantages over those of macroscales, including more contact surface area per volume ratio, better threshold, and better matrix reinforcement bonds. These unique advantages contribute to the emergence of some physical and thermal properties like high tensile strength, high elastic modulus, high water resistance, and high fracture toughness and ductility.

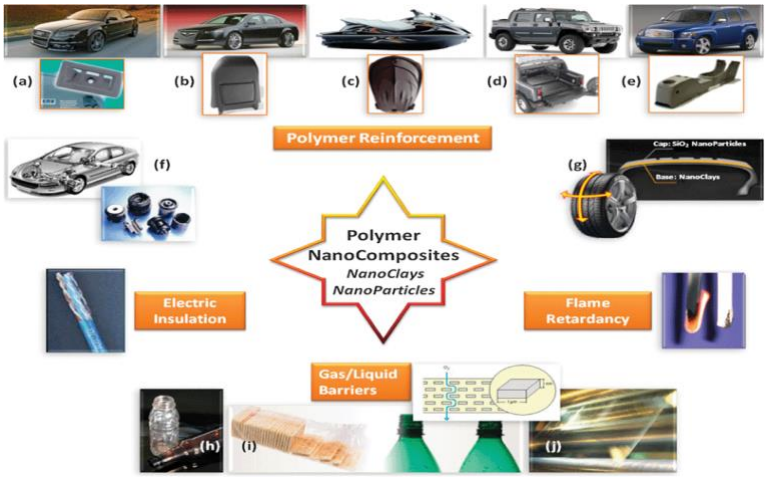

Figure 2.9. PNCs in broad cutting-edge applications (Guo et al., 2018)

Historically, Toyota Automobile Company was the pioneer in this field which made the first step to perform the seminal research on the polymeric matrices reinforced with clay platelets. Later on, substantial experimental investigations were then performed on examination of the impact of clay properties on the strength, durability and reliability of the resulting PNCs in composite industry (Usuki et al., 1993). It was discovered that the addition of 5 wt. % of nanoclay in a composite system can increase the effective Young's modulus and tensile strength of the resulting PNC up to 34% and 25%, respectively (Chan et al., 2011). PNCs can be used as powders in laser sintering applications for increasing the strength, elastic modulus and elongation at break for the entire system (Almansoori et al., 2017). Experimental evidences have clarified that exfoliated clay can be reshaped into a single clay platelets of nanosized by exchanging ion and then can be easily dispersed into polymeric matrix solutions for improving the mechanical properties such as the effective tangent modulus, tensile strength and stiffness of the resulting PNCs (Rahman and Wu, 2017). For example, nyon-6 based PNC, a kind of polymer nanocomposite, is prepared through ring polymerization of intercalated clay which can be further converted into exfoliated clay platelets and double the tensile properties of the nylon-6

nanocomposite (Kojima et al., 1993). Such significant improvement in tensile strength of PNCs could not be achieved if intercalated clay was used. Furthermore, PMCs reinforced with nanoclay have noticeable impact on tissue engineering as well. Nanoclay loaded polymer composite scaffolds show better protein absorption and hydrophobicity reductions in bone tissue system (Nitya et al., 2012).

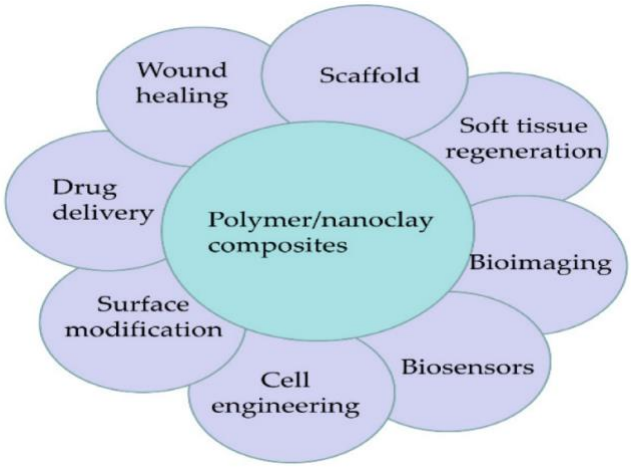

Figure 2.10. PNCs in biomedical applications (Guo et al., 2018)

Besides, PNCs has been used significantly in numbers of biomedical applications as well as shown in Fig. 2.10. One recent research study has shown that exfoliated clay at a weight content around 5% can significantly increase the tensile strength of the resulting PNC by 50% (Alexandre & Dubois, 2000). Other experimental investigations have also indicated that PNCs have high thermal stability, surface wettability and noticeable gas barrier properties which pave the way to replace conventional PMCs with PNCs (Alexandre & Dubois, 2000; Chen et al., 2013; Tjong, 2006; Schadler et al., 2007; Paul & Robeson, 2008). Understanding of the toughening and failure mechanisms in PNCs is important to PNC design, processing and application, while less theoretical and computational studies have been done yet. To address this issue, one of the aims of this thesis

is set to formulate CZM-based FEM for determining the properties and behaviors of nanoclay responsible for the toughening of PNCs.

2.2.2. Current Understanding

In the past several decades, remarkable efforts have been imposed on to model based analysis and computational simulation of the PNCs for determining the mechanical and thermal properties of the entire composite systems. Most recent investigations have been focused on the geometric properties of the clay-matrix, i.e. length of the particle, aspect ratio, volume fraction, etc., and emphasis has been placed on how these properties impact the physical and mechanical properties of the resulting PNCs. Research efforts have been dedicated to the understanding of the excellent mechanical properties of PNCs via forming various theoretical models based on existing models, such as Elsheby's equivalent model, Mori-Tanka models, Halpin-Tsai model, self-consistent models, and simple shear-lag model and its extensions, among others (Tucker & Liang, 1999). Tucker and Liang (1999) identified the optimal model for predicting the effective stiffness of short aligned composite based on detailed FEA. They concluded that Halpin-Tsai model provides reasonable effective stiffness for the short-fiber composites, while the simple shear-lag model is capable of predicting the most accurate effective longitudinal modulus of the composites when the aspect ratio is greater than 10. Weon and Sue (2005) used Halpin-Tsai and Mori-Tanaka micromechanics-based models for examining the effect of clay orientation and aspect ratio on the mechanical behavior of nylon-6 nanocomposites. Their studies showed that the decrease of clay aspect ratio and orientation contribute to the increase of fracture toughness and ductility of the PNCs. In addition, Tsai and Sun (2004) developed the shear-lag micromechanics models to predict the effects of clay platelet dispersions on the load transfer efficiency of the PNCs. It was demonstrated that the load transfer efficiency for uniformly dispersed platelets are excellent due

to the large aspect ratios of the platelets. Recently, Rahman and Wu (2017) conducted the computational micromechanics study on the effect of processing parameters on the elastoplastic behavior of PNCs and found that the increase of the clay particle volume fraction and aspect ratio contributes to the increase of ultimate tensile strength of the PNCs. Similar computational micromechanics studies were also performed by others in the composites community. For instance, Dong and Bhattacharyya (2010) used a simple micromechanical approach to determine the effective mechanical properties of PNCs in terms of the clay aspect ratio and the pattern of clay dispersion. Therein, three phase representative area element (RAE) was adopted to take into account the interphase between the clay particles and the polymeric resins. Their computational results indicated that the interphase properties do not have noticeable impact on the effective moduli of exfoliated PNCs, whereas in the case of intercalated PNCs, the interphase properties are quite independent of the pattern of clay dispersion. In order to describe the popularities of PNCs in recent years, Kumar et al. (2018) presented a pie chart describing about the share of publications in topics covering "nanocomposites and applications" out of a total of 2725 publications where polymer nanocomposites dominate the statistics with 48% publications rate as shown in Fig 2.11. Besides, more recent research efforts have been devoted to the characterization, modeling and optimization of the mechanical properties of PNCs as summarized in the recent review papers and in references therein (Alexandre & Dubois, 2000; Tjong, 2006; Schadler et al., 2007; Dong & Bhattacharyya, 2010; Hu et al., 2010; Nitya et al., 2012; Chen et al., 2013).

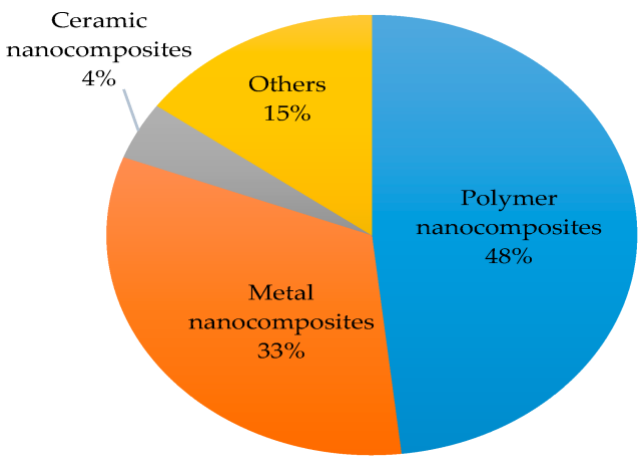

Figure 2.11. Publication statistics in topic: “nanocomposites and applications” (Kumar et al., 2018)

To date, all the computational studies on determination of the mechanical, physical and thermal properties of PNCs were based mainly on the simple micromechanics model, where CZM was not adopted for exploring the failure mechanism and debonding process. However, CZM is a powerful computational model capable of dealing with the nonlinear failure process and therefore is able to provide potential design guidelines for optimized mechanical properties of PNCs. The integration of CZM into FEM for determining the mechanical properties and failure behavior of the PNCs is addressed in detail in this thesis.

2.2.3. Outstanding Problems in Stress Analysis of PNCs

In the above, it can be observed that most research efforts were focused on the determination of the effective moduli and tensile strength of PNCs via mimicking the classic micromechanics and related computational models without CZM. Yet, no study has been reported on determining the effective stress-strain behaviors of PNCs using CZM-based computational approach.

Thus, in chapter 5 of this thesis, CZM is adopted to predict the effective mechanical properties and failure behaviors of PNCs. RAEs of both the typical stack and stagger model configurations are utilized, and the polymeric resins are treated as an ideal elastoplastic solid whereas the nanoclay particles are assumed as stiff elastic platelets. Besides, round shaped clay particles are considered for removing the stress singularity, and comparison of the stress field with those of RAEs of stack model with simple sharp-edged clay platelets. A family of the effective stress-strain diagrams are extracted based on the detailed computational studies at varying aspect ratios and volume fractions of the clay particles. Comparative study of the stack and stagger configurations of the PNCs is conducted. The influence of the CZM on determination of the mechanical properties of the PNCs is analyzed through in detailed nonlinear FEA. Conclusions of the present computational studies and relevant potential applications are sequenced in chapter 5 of this thesis paper.

In chapter 6, the summaries of the current research and the future work beyond the present works are enclosed in detail.

2.3. Cohesive Zone Model

2.3.1. Cohesive Zone Modeling Technique

Cohesive zone model (CZM) is a standard, widely accepted computational model, which is capable of exploring the failure mechanisms in the crack process zone due to the plastic deformations. The difference of CZM with classical LEFM is that a singular zone at the crack tip in LEFM is now replaced by a process zone of nonsingular cohesive stresses in CZM. CZM can reasonably predict the crack initiation and growth of un-cracked surfaces which is not possible in LEFM. CZM was originated from the inspiration of Dugdale (1960)-Barenblatt (1962) process

zone model. In the view of CZM, failure and cracking in any process system is explained by a cohesive law, which is nothing but the relation between the surface tractions (peeling and/and shearing forces) and the opening and/and sliding displacements.

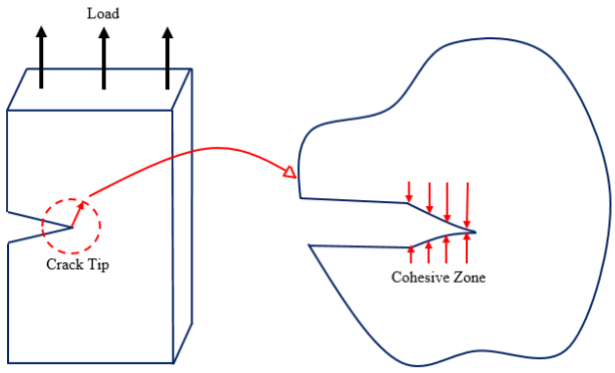

Figure 2.12. Cohesive Zone Model (CZM)

CZM can be described as a crack model where the entire body remains in elastic region until that nonlinearity attributes in the process zone. Therefore, the entire system can be summarized in three ways: (1) at the beginning, a linear elastic region involves, (2) crack initiates due to the increase of load, and finally (3) crack initiation to complete failure happens which is governed by the cohesive zone law.

CZM has plenty of advantages. It incorporates damage initiation and damage propagation in the same model, making the way to analyze both strength and fracture toughness altogether in one model effectively (Turon, 2006; Harper and Hallett, 2008). CZM carries one major advantage such that this model is capable to capture the configuration following the crack initiation and propagation till the final catastrophic failure of the body under investigation. (Da Silva and Campilho, 2012). The traction-separation law in CZM is relatively simple in nature and has both reversible and irreversible characteristics which allow to retain the non-damaged elements when complete cyclic loading is considered (Bosch et al., 2010). CZM does not require an initial crack

for the crack propagation due to the characteristics or natures of cohesive elements. Cracks in CZM can exhibit at any region or interface arbitrarily. Multiple crack paths can follow up and the analysis of the un-cracked structures can be conducted efficiently (Elices et al., 2002) by this micromechanics model based FEA tool.

2.3.2. Current Understanding

The relationship between the stress and opening displacement in CZM is characterized by the traction-separation law, i.e., the traction-separation curve (See Fig. 2.13). The peak value of the traction-separation curve is the cohesive strength and the area formed by the entire curve is the fracture toughness or cohesive fracture energy release rate. One key part of the CZM is the selection of proper shape of the process zone model of interest. Three popular shapes of the CZM are commonly used, i.e., bilinear (triangular), exponential, and trapezoidal, depending on the requirements of the use (Fig. 2.13).

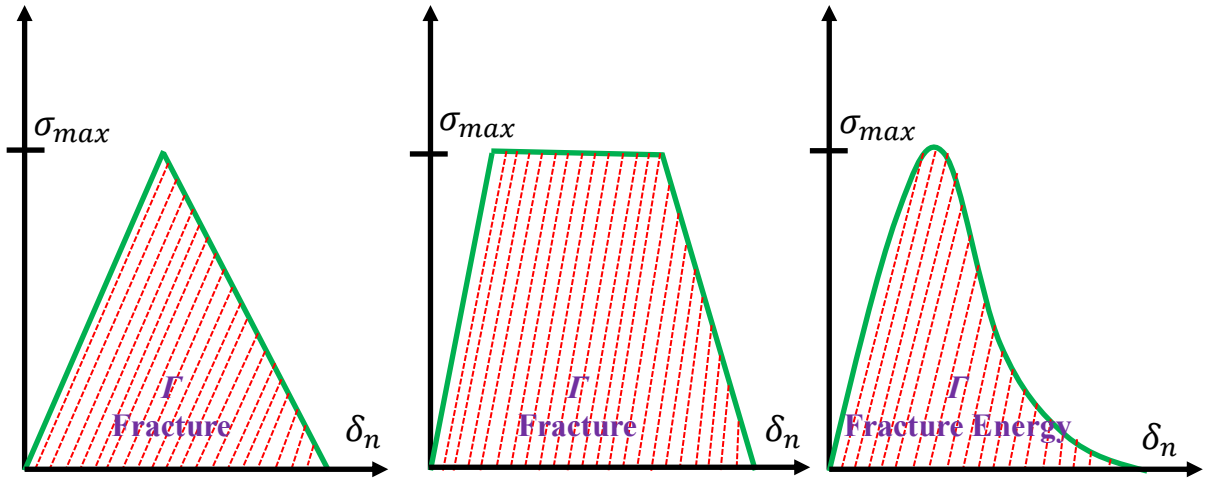

(a) Bilinear CZM (b) Trapezoidal CZM (c) Exponential CZM

Figure 2.13. Types of CZM

The critical normal and tangential fracture toughness of the bilinear CZM is

$$G_{cn} = \frac{1}{2}\sigma_{max}\delta_n{}^{c}\,, \tag{2.4}$$

where σ_{max} is the peak cohesive stress i.e., the cohesive strength, and $\delta_n{}^{c}$ is the critical opening displacement. One of the most popular way of defining of a mixed-mode debonding can be presented according to a power law energy based criterion

$$\left(\frac{G_n}{G_{cn}}\right)^2 + \left(\frac{G_t}{G_{ct}}\right)^2 = 1\,, \tag{2.5}$$

where,

$$G_n = \int P du_n \tag{2.6}$$

and

$$G_t = \int T_t du_t \tag{2.7}$$

are the normal and tangential fracture energies respectively with P and T_t are the normal and tangential contact stress respectively. CZM has broad applications in nonlinear failure analysis of various bonded joints and composites. It has become a favorable method for the prediction of damage initiation and propagation since the recent advances in FEMs. CZM was first applied in brittle material in a local approach during early 1990s (Xu and Needleman, 1994; Camacho and Ortiz, 1996). The broad applications of CZM in stress and strength analysis of composite materials were started in the last decade with fast development of modern finite element software packages, which is a major advance in failure or fracture mechanics (Cavalli and Thouless, 2001; Camanho et al., 2003; Li et al., 2005; Li et al., 2006; Turon et al., 2006). Since then, CZM and its introduction in finite element software has proven to be a high-efficient, effective computational tool for the simulation of the cracking and damage initiation and propagation in bonded joints and ABJs

(Blackman et al., 2003; Li et al., 2005; Alfano et al., (2007); Sun et al., 2008; Campilho et al., 2009; Campilho et al., 2009; Gustafson and Waas, 2009). For instance, Alfano et al. (2007) performed a CZM-based FEA to simulate the mode-I fracture of adhesively bonded double cantilever beam for exacting the load-displacement results, which were compared with those of experimental data retrieved from the literature. The comparative study showed a good agreement with the experiments and hence provided a computer aided design guideline for desired mechanical strength and properties of ABJs. In addition, CZM-based FEA has been also commonly used for modeling and characterizing the mechanical properties and fracture of concretes, polymers, metals and functionally graded materials (Li & Siegmund, 2002; Jin et al., 2003; Shim et al., 2006; Song et al., 2006; Song et al., 2006; Roesler et al., 2007).

2.3.3. Outstanding Problems in Failure Analyses of ABJs and PNCs with CZM

In the past few decades, extensive investigations have been conducted on determination of the mechanical properties and failure mechanisms of ABJs. Yet no systematic study has been initiated for predicting the full range failure process of bonded joints and ABJs. Similarly, many researchers have worked on the processing and characterization of PNCs. Yet, the outcomes of their works were unable to predict the elastoplastic failure process of PNCs. Therefore, one key goal of this thesis work was to provide some initial understandings of the nonlinear failure process and the mechanical behaviors of both ABJs and PNCs using CZM based computational tool for better design and optimization with desired mechanical properties.

3. THEORETICAL MODELING OF THE ELASTOPLASTIC FRACTURE OF ADHESIVELY BONDED JOINTS WITH LARGE PLASTIC DEFORMATIONS

3.1. Introduction

In this chapter, an elastoplastic model with the power-law strain hardening is to be formulated for determining the fracture toughness of ABJs with large plastic deformations and afterward springback where the experimental configuration can be presented as shown in Fig. 3.1. Both thin-layered ductile adherends (aluminum alloy and mild steel) are considered in the entire loading and unloading process during the event of fracture. The maximum plastic deformation occurs at the crack tip due to the working moment exerted by the advancing wedge in the fracture test. The radii of curvature of the adherends are measured from the post-fracture specimens after complete elastic springback, which are much greater than those corresponding to the maximum bending moment to advance the crack propagation. Such fundamental concepts for determining the fracture toughness of ABJs have been ignored in literature, where simply nonlinear elastic models without taking into account the elastic springback effect were used. As results, these oversimplified literature models typically induce substantial modeling errors to extract the fracture toughness based on fracture test data. Therefore, the theoretical study in this chapter will provide a more accurate fracture model to extract the fracture toughness of ABJs with large plastic deformations and springback.

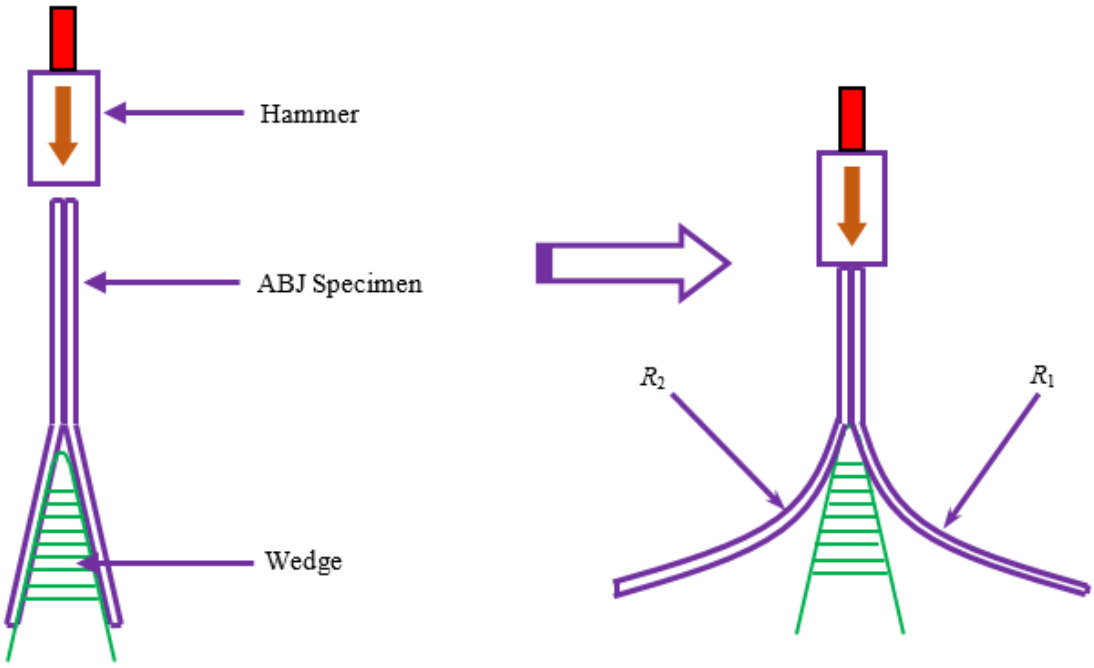

Figure 3.1. Experimental configuration of an impact fracture test of ABJs where a low-speed moving hammer is used to steadily drive the wedge induced debonding

3.2. Problem Statement and Solutions

The representative elastoplastic stress-strain diagram is illustrated in Fig. 3.2. The fracture toughness of ABJs made of both aluminum alloy and mild steel adherends are to be determined. The nonlinear properties of the ABJ adherends are assumed to be elastoplastic solids with power-law strain hardening behavior.

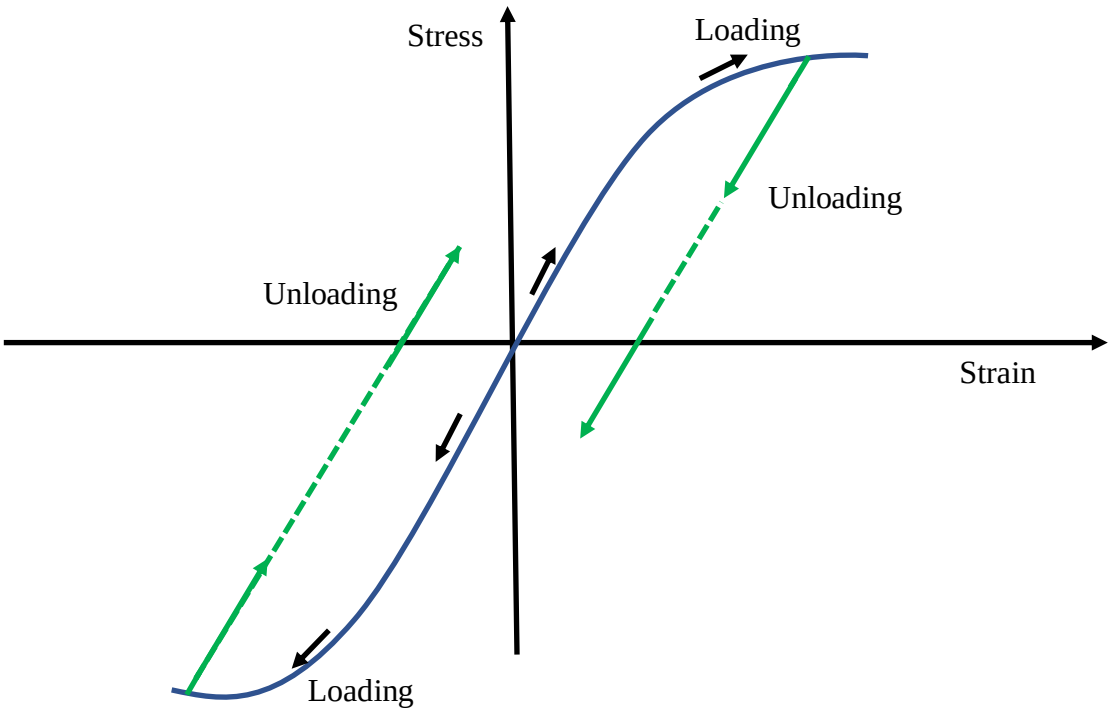

Figure 3.2. Schematic diagram of the stress-strain relation of elastoplastic materials with power-law strain-hardening under loading and unloading

The nonlinear elastoplastic stress-strain relation based on power-law strain-hardening is

$$\sigma = \begin{cases} E\varepsilon\,, & (\sigma \le \sigma_0) \\ \dfrac{\sigma_0}{\left(\dfrac{\sigma_0}{E}\right)^n}\varepsilon^n\,, & (\sigma > \sigma_0) \end{cases} \tag{3.1}$$

where, σ_0 is the yield strength for both compression and tension, E is the Young's modulus, and n is the power-law hardening index. In this model, when $n \to 1$, the material model recovers that of linearly elastic solids; when $n \to \infty$, the material model recovers that of ideally elastoplastic solids. The deformations of the adherends of ABJs during fracture are assumed to follow that of Euler-Bernoulli beams, i.e., the axial strain in the cross section of adherends can be expressed in terms of the radius of curvature ρ of the deflected arms as

$$\varepsilon = \frac{y}{\rho}. \tag{3.2}$$

Herein, y is the distance from a material point of interest of the cross section of the adherend to the neutral axis shown in Fig. 3.3. Elastic springback is considered such that once crack grows, unloading at the crack tip occurs. The critical point y_c, beyond which the plastic deformation is induced can be determined as

$$y_c = \rho\varepsilon_0 . \tag{3.3}$$

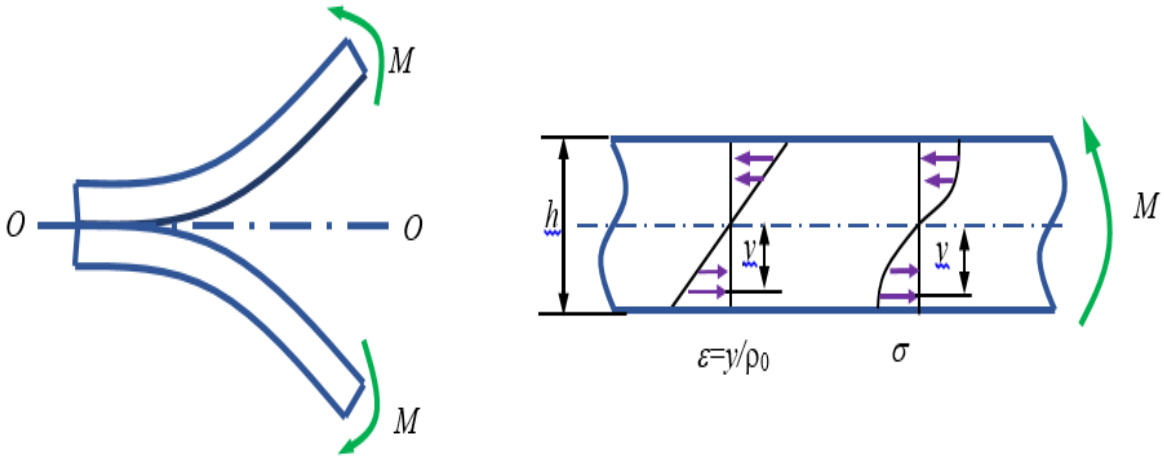

(a) (b)

Figure 3.3. Double cantilever beam (DCB) under pure bending moment M: (a) specimen loading configuration and (b) schematic stress-strain distributions across the beam thickness

Here, ρ is the radius of curvature of a given material. The critical bending moment to initiate the crack growth in each adherend is expressed as

$$M_c = \sigma_0 h^2/6 . \tag{3.4}$$

In this entire study, the power-law strain-hardening elastoplastic model is used to accurately approach the plastic deformations and springback of the ABJ adherends during the

fracture event. Therefore, accurate calculations of the strain energies stored in the adherends before and after the crack advance can result in the accurate fracture toughness of the ABJs.

3.2.1. Nonlinear Elastic vs Nonlinear Elastoplastic Material Models

A simple power-law strain-hardening elastoplastic model has been adopted for determining the fracture toughness of ABJs with large plastic deformations and afterward springback. The advantages of the present elastoplastic model [Fig. 3.5] superior to those linear and nonlinear elastic models [Fig. 3.4] are that both the plastic deformations and elastic springback of the ABJ adherends after complete unloading can be counted in the present elastoplastic model, which is capable of providing a more accurate and rational description of the fracture event of ABJs.

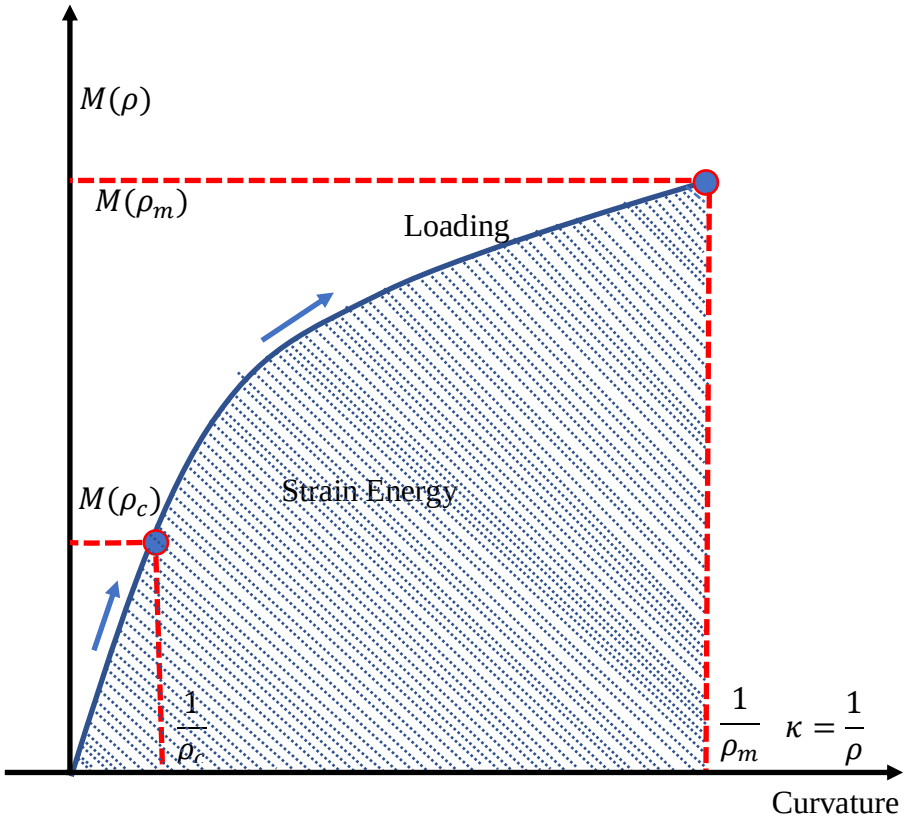

Figure 3.4. Schematic diagram of a nonlinear elastic model with the loading moment-curvature relation of the ABJ arms

The strain energy dissipation of a nonlinear elastoplastic beam during the entire loading and unloading cycle is exemplified in Fig. 3.5, in which the nonlinear moment-curvature diagram consists of a linearly elastic loading region at the beginning, then a nonlinear loading region corresponding to the strain-hardening loading region, and finally an elastic springback corresponding to the unloading region.

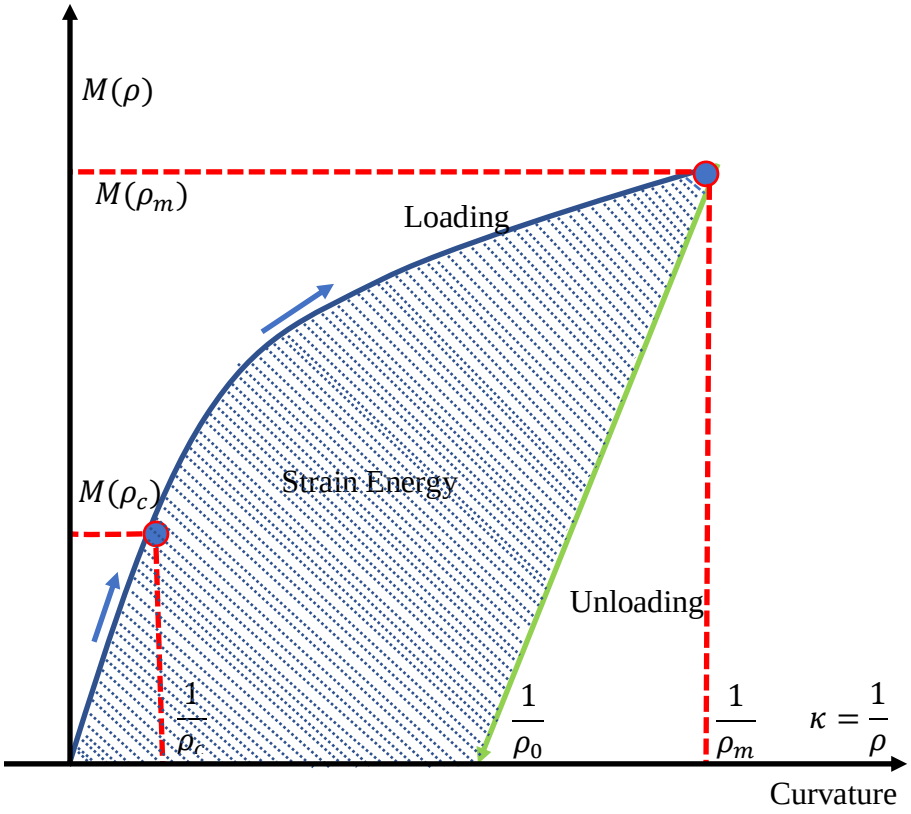

Figure 3.5. Schematic diagram of a nonlinear elastoplastic model and the loading and unloading moment-curvature relation of the ABJ arms

Based on the mechanisms of simple power-law strain-hardening elastoplastic material model, one of the major purpose of this study is to formulate a theoretical fracture model for determining more realistic and accurate fracture toughness of ABJs with large plastic deformations and afterward springback. This theoretical study based on material elastoplasticity is simply beyond several conventional modeling approaches based on nonlinear elastic model. Till now, a number of theoretical studies has been performed on determining the fracture toughness of ABJs, which fall short of more appreciable physical meaning due to either the consideration of less accurate material model or the addition of less proved ad hoc assumptions.

3.2.2. Elastoplastic Deformation of Beams

3.2.2.1. Radius of Curvature after Springback

The measured radii of curvature of the post-fracture adherends after complete unloading become larger than those corresponding to the maximum bending moment, at which crack propagation happens. According to the fundamental rigid-plane assumption of Euler-Bernoulli beams, the axial elastic strain in the adherend cross-section after complete elastic springback ρ_0 is

$$\Delta\varepsilon = y\left(\frac{1}{\rho_m} - \frac{1}{\rho_0}\right). \tag{3.5}$$

In the above, ρ_m represents the radius of curvature of the adherend neutral axis corresponding to the maximum bending moment. The residual plastic strain ε_p appears when $\sigma > \sigma_0$ and $\varepsilon > \varepsilon_0$, which can be expressed according to the power-law strain-hardening stress-strain relation in Fig. 3.2 as

$$\varepsilon_P = \frac{y}{\rho_m} - \frac{1}{{\varepsilon_0}^{n-1}}\left(\frac{y}{\rho_m}\right)^n. \tag{3.6}$$

In the above, when $n \to 1$, the residual plastic strain becomes $\varepsilon_p = 0$, a trivial outcome corresponding to the case of linearly elastic materials. The net bending moment in an arbitrary cross-section of the adherend after complete elastic springback is zero, which leads to a moment equilibrium equation such that

$$\int_{-y_c}^{y_c} E\varepsilon y dy + 2\int_{y_c}^{h/2} E(\varepsilon - \varepsilon_P) y dy = 0, \tag{3.7}$$

where the linear flexural strain is found from

$$\varepsilon = y/\rho_0\,. \tag{3.8}$$

It is noted from Eq. (3.7) that, the elastic region near the neutral axis of the adherend cross section keeps the similar stress condition whereas the elastoplastic region far from the linearly

elastic region switches the stress direction in order to maintain the global bending moment free of the adherend cross section. The radius of curvature after complete springback is determined by substituting Eqs. (3.6) and (3.8) into Eq. (3.7) and can be presented as

$$\frac{\eta_0}{\eta_m} = 1 - \left(1 - \frac{3}{n+2}\right)\left(\frac{\eta_m}{\varepsilon_0}\right)^{-3} - \frac{3}{n+2}\left(\frac{\eta_m}{\varepsilon_0}\right)^{n-1}. \tag{3.9}$$

Here, $\eta_m = h/(2\rho_m)$ and $\eta_0 = h/(2\rho_0)$. For n=1 (i.e., linearly elastic materials), becomes zero which leads to $\rho_0 \rightarrow \infty$ i.e., the adherends of ABJs recover their initial straight state. However, in the case of ideally elastoplastic materials, i.e., $n \rightarrow \infty$,

$$\frac{\eta_0}{\eta_m} = 1 - \left(\frac{\eta_m}{\varepsilon_0}\right)^{-3}. \tag{3.10}$$

The increase of the radii of curvature after complete springback ρ_0 depends on the decrease of the minimum radii of curvature at the maximum bending moment ρ_m to initiate the crack growth.

3.2.2.2. Moment Curvature Relation

With the aid of the constitutive law of the material as shown in Eq. (3.1), the bending moment corresponding to the resultant radius of curvature of the adherends is formulated as

$$\frac{M(\rho)}{EI/\rho} = \begin{cases} \left(1 - \frac{3}{n+2}\right)\left(\frac{\eta}{\varepsilon_0}\right)^{-3} + \frac{3}{n+2}\left(\frac{\eta}{\varepsilon_0}\right)^{n-1}, & (\eta > \varepsilon_0) \\ 1, & (0 \le \eta \le \varepsilon_0) \end{cases} \tag{3.11}$$

where, $\eta = h/(2\rho)$ and the moment of inertia of the adherend cross section is taken as $I=h^3/12$. Given a bending moment M, the resultant radius of curvature ρ of the adherend can be predicted by solving the nonlinear equation (3.11), where the maximum axial strain at both the top and bottom adherend is $h/(2\rho)$.

The bending moment per unit width for a given radius of curvature ρ ($\rho_m < \rho < \rho_0$) is determined similar to Eq. (3.11) as

$$\frac{M(\rho)}{EI/\rho_m} = \left(\frac{\eta}{\eta_m} - 1\right) + \left(1 - \frac{3}{n+2}\right)\left(\frac{\eta_m}{\varepsilon_0}\right)^{-3} + \frac{3}{n+2}\left(\frac{\eta_m}{\varepsilon_0}\right)^{n-1}, \tag{3.12}$$

where, $\eta = h/(2\rho)$ and in the case of linearly elastic material, i.e., n=1, the resultant bending moment is found as

$$M(\rho) = \frac{Eh^3}{12\rho}, \tag{3.13}$$

i.e., the trivial result of the elastic deflection of an *Euler-Bernoulli beam*.

In addition, for the case when n=∞, the resultant bending moment becomes

$$M(\rho) = EI\left(\frac{1}{\rho} - \frac{1}{\rho_m}\right) + \frac{2}{3}\frac{E{\rho_m}^2}{{\varepsilon_0}^{-3}}, \tag{3.14}$$

which represents the bending moment at any curvature M is a function of that curvature ρ and the minimum radii of curvature at the maximum bending moment ρ_m necessary to initiate the crack growth.

3.2.3. Fracture Toughness of ABJs with Large Plastic Deformations and Springback

3.2.3.1. Work Done by Moment

The fracture toughness of ABJs with large plastic deformations and elastic springback can be expressed as

$$\Gamma = \frac{\Delta W_1 + \Delta W_2 - \Delta U_1 - \Delta U_2}{\Delta l}, \tag{3.15}$$

where for a crack growth Δl, ΔW_i and ΔU_i (i=1,2) are the work done due to external bending moment and the strain energy stored in each arm of the ABJ adherend per width Δl, respectively. The maximum working moment can be determined using Eq. (3.11), provided that the impact fracture test is treated as a steady dynamic process. Therefore, for a crack growth Δl, the work done in each adherend arm due to the bending moment per unit width can be expressed as

$$\frac{\Delta W}{Eh\Delta l} = \left(\frac{1}{3} - \frac{1}{n+2}\right) {\varepsilon_0}^2 \left(\frac{\eta_m}{\varepsilon_0}\right)^{-1} + \frac{1}{n+2} {\varepsilon_0}^2 \left(\frac{\eta_m}{\varepsilon_0}\right)^{n+1}. \tag{3.16}$$

In the limiting case of linearly elastic material, i.e., n=1, the work done by moment for a crack growth Δl can be expressed as

$$\frac{\Delta W}{Eh\Delta l} = \frac{1}{3} {\varepsilon_0}^2 \left(\frac{\eta_m}{\varepsilon_0}\right)^2, \tag{3.17}$$

where, square times the increase of the radii of curvature at the maximum bending moment ρ_m contributes to the increase of the resultant work done ΔW per unit width of the adherend during the fracture process.

In the limiting case when n=∞, it becomes

$$\frac{\Delta W}{Eh\Delta l} = \frac{1}{3} {\varepsilon_0}^2 \left(\frac{\eta_m}{\varepsilon_0}\right)^{-1}, \tag{3.18}$$

where, the total work done by moment ΔW during the entire fracture process increases with the decrease of the minimum radii of adherend curvature ρ_m before complete springback happens.

3.2.3.2. Strain Energy Stored in Adherend Arm

Strain energy stored in each adherend arm after complete elastic springback is essential for more realistic prediction of the fracture toughness of ABJs. In view of this, the strain energy stored in each adherend arm (per unit width) taking the elastic springback effect into account is determined as

$$\Delta U = \left[\int_{\infty}^{\rho_c} \frac{Eh^3}{12\rho}\, d\left(\frac{1}{\rho}\right) + \int_{\rho_c}^{\rho_m} M(\rho)\, d\left(\frac{1}{\rho}\right) - \frac{1}{2} M(\rho_m)\left(\frac{1}{\rho_m} - \frac{1}{\rho_m}\right)\right] \Delta l\,. \tag{3.19}$$

Here, $\rho_0 = h/(2\varepsilon_0)$ is the radius of curvature of initial yielding, ρ_m is the minimum radius of curvature, and $M(\rho_m)$ is the maximum bending moment to drive the fracture process. The strain energy integration (3.19) is illustrated in Fig. 3.5, in which the 1st term signifies the strain energy

stored in the linearly elastic loading region, the 2nd term signifies the strain energy stored in the strain-hardening loading region where $M(\rho_m)$ is specified in Eq. (3.11), and the 3rd term denotes the released strain energy in the springback unloading region where $M(\rho)$ is denoted in Eq. (3.12). The total strain energy stored in each adherend arm of ABJs per unit width after complete elastic springback can be determined by substituting Eq. (3.9) and Eq. (3.11) into Eq. (3.19) as

$$\begin{aligned}\frac{\Delta U}{Eh\Delta l} = \quad & \frac{{\varepsilon_0}^2}{6} + \frac{{\varepsilon_0}^2}{3}\{-\varepsilon_0\left(1-\frac{3}{n+2}\right)({\eta_m}^{-1}-{\eta_c}^{-1}) \\ & + \frac{3}{(n+1)(n+2)}(\varepsilon_0)^{-(n+1)}\left[{\eta_m}^{(n+1)}-{\eta_c}^{(n+1)}\right]\} \\ & -\frac{1}{6}\,\eta_m(\eta_m-\eta_0)\left[\left(1-\frac{3}{n+2}\right){\varepsilon_0}^3{\eta_m}^{-3}+\frac{3}{n+2}\,{\varepsilon_0}^{-n+1}{\eta_m}^{n-1}\right]\end{aligned} \tag{3.20}$$

In the limiting case of linearly elastic materials, i.e., n=1, the strain energy stored in each arm can be presented as

$$\frac{\Delta U}{Eh\Delta l} = \frac{{\varepsilon_0}^2}{6} + \frac{1}{6}({\eta_m}^2-{\eta_c}^2) - \frac{1}{6}\,\eta_m(\eta_m-\eta_0)\,. \tag{3.21}$$

Furthermore, in the case when n=∞, it becomes

$$\frac{\Delta U}{Eh\Delta l} = \frac{{\varepsilon_0}^2}{6} - \frac{{\varepsilon_0}^3}{3}({\eta_m}^{-1}-{\eta_c}^{-1}) - \frac{1}{6}{\varepsilon_0}^3{\eta_m}^{-2}(\eta_m-\eta_0)\,. \tag{3.22}$$

3.2.3.3. Theoretical Fracture Toughness of ABJs

Fracture toughness is one of the mechanical properties, which designates the capability of a solid material to resist crack initiation and growth. Here, the energy dissipated by the adhesive layer to advance unit area crack growth can be determined by substituting work done by the wedge in Eq. (3.16) and the strain energy stored in each arm by plugging Eq. (3.20) into Eq. (3.15).

Therefore, the theoretical fracture toughness of the ABJs made of two identical elastoplastic adherends is

$$\frac{\Gamma}{2Eh} = \left(\frac{1}{3}-\frac{1}{n+2}\right){\varepsilon_0}^3{\eta_m}^{-1} + \frac{1}{n+2}{\varepsilon_0}^{-n+1}{\eta_m}^{n+1}$$
$$-\frac{{\varepsilon_0}^2}{6} - \frac{{\varepsilon_0}^2}{3}\left\{-\varepsilon_0\left(1-\frac{3}{n+2}\right)({\eta_m}^{-1}-{\eta_c}^{-1}) + \frac{3}{(n+1)(n+2)}(\varepsilon_0)^{-(n+1)}\left[{\eta_m}^{(n+1)}-{\eta_c}^{(n+1)}\right]\right\}$$
$$-\frac{1}{6}\eta_m(\eta_m-\eta_0)\left[\left(1-\frac{3}{n+2}\right){\varepsilon_0}^3{\eta_m}^{-3} + \frac{3}{n+2}\,{\varepsilon_0}^{-n+1}{\eta_m}^{n-1}\right]. \quad (3.23)$$

Here, $\eta_m = h/(2\rho_m)$ and $\eta_0 = h/(2\rho_0)$. In the case of linearly elastic materials, i.e., n=1, the corresponding fracture toughness is

$$\frac{\Gamma}{2Eh} = \frac{1}{3}{\eta_m}^2 - \frac{{\varepsilon_0}^2}{6} - \frac{1}{6}({\eta_m}^2-{\eta_c}^2) - \frac{1}{6}\eta_m(\eta_m-\eta_0)\,, \quad (3.24)$$

where, both the radii of curvature before and after complete springback are denoted as ρ_m and ρ_0, respectively, which are the functions of fracture toughness Γ. Increase of the elastic strain ε_0 after complete unloading contributes to the increase of the resultant fracture toughness Γ to dissipate the total strain energy during this entire loading and unloading process which can be predicted effectively using Eq. 3.24.

In addition, in the case when n=∞, the corresponding fracture toughness is reduced to

$$\frac{\Gamma}{2Eh} = \frac{1}{3}{\varepsilon_0}^3{\eta_m}^{-1} - \frac{{\varepsilon_0}^2}{6} + \frac{{\varepsilon_0}^3}{3}({\eta_m}^{-1}-{\eta_c}^{-1}) - \frac{1}{6}{\varepsilon_0}^3{\eta_m}^{-2}(\eta_m-\eta_0)\,. \quad (3.25)$$

Therefore, likewise the linearly elastic material case, both the radii of curvature before ρ_m and after complete springback ρ_0 are the functions with respect to the fracture toughness Γ. This theoretical fracture toughness Γ presents a nonlinear elastoplastic relationship with the elastic strain ε_0 after complete loading.

Compared to the fracture toughness formula (2.2) derived by Thouless et al. (1998) based on nonlinear elastic model, the present fracture toughness formula (3.23) based on generalized power-law strain-hardening elastoplastic model and taking into account the entire loading and unloading path of the elastoplastic materials is expected to be more realistic for extracting the accurate fracture toughness of ABJs with large plastic deformation and afterward springback. In order to employ Eq. (3.23), the first is to solve the nonlinear Eq. (3.9) to predict the minimum radius of curvature ρ_m at the steady working moment M based on the radius of curvature ρ_0 measured from the post-fracture specimen arms after complete elastic springback. Eq. (3.9) can be solved efficiently by applying general nonlinear numerical methods such as the Newton-Raphson method. The work done by moment ΔW and strain energy ΔU stored in each arm of the ABJs for crack growth Δl can be predicted by evoking Eq. (3.16) and Eq. (3.20) respectively.

3.2.4. Model Validation

Based on the measured radii of curvature of the post-fracture arms, Eq. (3.9) is used to predict the minimum radius of curvature of each arm when the working moment reaches the maximum value. To validate the present model, Eq. (3.23) is used to extract the fracture toughness based on the experimental data by Thouless et al. (1998) and to compare those predicted by other models available in the literature. Herein, both aluminum alloy and mild steel joints are used, and the mean values of their mechanical properties are considered (aluminum alloy: E= 69 GPa and σ_0=113 MPa, mild steel: E= 200 GPa and σ_0= 205 MPa); the measured radii of curvature after springback are taken from Thouless et al. (1998). Results of the fracture toughness of ABJs made of both aluminum alloy and mild steel joints are tabulated in Tables 3.1 and 3.2 respectively, in which ABJs with varying adhesive thickness, strain-hardening indices and radius of the curvature of the adherends after complete springback are considered. In addition, results of the fracture

toughness based on the simplified nonlinear elastic model by Thouless et al. (1998) and William's corrections (1998) based on the root rotation at the point of adhesion are tabulated in detail.

Table 3.1. Fracture toughness of aluminum-bonded adhesives A (LMD1142), B (XD3600) and C (Esses 73301).

h(mm)	Strain-hardening index n	R_p (mm)	Γ(kJ/m^2) (Thouless et al., 1998)	Γ(kJ/m^2) (Williams, 1998)	Γ(kJ/m^2) (Present Model)
Adhesive A					
1.01	0.271	10	1.69±0.25	3.2	3.77±0.12
1.31	0.234	14	1.92±0.30	4.2	3.86±0.14
1.61	0.270	19	2.13±0.32	4.1	5.16±0.22
Adhesive B					
1.01	0.271	13	1.33±0.20	2.4	3.08±0.19
1.31	0.234	19	1.30±0.21	2.6	2.89±0.12
1.61	0.270	24	1.56±0.23	2.8	4.20±0.16
Adhesive C					
1.01	0.271	18	0.83±0.12	1.4	2.19±0.09
1.31	0.234	27	0.80±0.12	1.5	2.05±0.05
1.61	0.270	37	0.96±0.14	1.4	2.85±0.06

Note: R_p is the weighted mean radius of curvature by Thouless et al. (1998) and Williams (1998). The fracture toughness based on the present model is calculated directly using the radii of curvature of aluminum alloy adherend arms where E= 69 GPa and σ_0= 113 MPa.

Table 3.2. Fracture toughness of steel-bonded adhesives A (LMD1142), B (XD3600) and C (Esses 73301).

h(mm)	Strain-hardening index n	R_p (mm)	Γ(kJ/m^2) (Thouless et al., 1998)	Γ(kJ/m^2) (Williams, 1998)	Γ(kJ/m^2) (Present Model)
Adhesive A					
0.91	0.158	12	1.14±0.17	2.7	1.82±0.08
1.14	0.131	15	1.14±0.17	3.1	2.15±0.06
1.41	0.124	22	1.33±0.20	4.4	2.25±0.06
Adhesive B					
0.91	0.158	16	0.86±0.13	1.5	1.46±0.06
1.14	0.131	21	0.83±0.12	1.9	1.37±0.04
1.41	0.124	32	0.79±0.12	2.0	1.27±0.08
Adhesive C					
0.91	0.158	28	0.42±0.06	0.8	0.87±0.05
1.14	0.131	43	0.31±0.08	1.4	0.59±0.01
1.41	0.124	75	0.34±0.10	0.7	1.28±0.13

Note: R_p is the weighted mean radius of curvature by Thouless et al. (1998) and Williams (1998). The fracture toughness based on the present model is calculated directly using the radii of curvature of steel adherend arms where E= 200 GPa and σ_0= 205 MPa.

It can be noted from Tables 3.1 and 3.2 that the present model does not evoke simplifications and *ad hoc* assumptions beyond the power-law strain-hardening model of elastoplastic solids and *Euler-Bernoulli beams* and is capable of predicting more reasonable and realistic fracture toughness of both aluminum-alloy and mild-steel ABJs. The results are also closed to William's correction which is based on the modification of root rotation at the point of adhesion and almost double the results as predicted by Thouless et al. (1998). In addition, the present model provides some overshoot values of the fracture toughness of ABJs. The potential reasons behind such deviations might be the test data collection, failure mechanisms beyond the assumptions of pure bending, or the dissipations of strain energy which are not entirely used for driving the growth of crack/ fracture process.

3.2.5. Scaling Analyses of Fracture Toughness of ABJs

Let us further examine the dependencies of the nonlinear loading and unloading moment-curvature diagrams upon the ABJ geometries and material properties. In the computational investigation, the minimum radius of curvature at the maximum bending moment $M(\rho_{min})$ is assumed as 25 mm. The adherend beams of aluminum alloy (beam thickness t= 1, 2, 3 and 4, yield stress σ_0= 113 MPa, Young's modulus E= 69 GPa, and strain hardening index n=0.0, 0.1, 0.2, 0.3, 0.5) and mild steel (beam thickness t=1, 2, 3 and 4, yield stress σ_0= 205 MPa, Young's modulus E=200 GPa, and strain hardening index n= 0.0, 0.1, 0.2, 0.3, 0.5) with unit beam width are utilized in the numerical process. All these adherend geometries and material properties are taken in the range of the experimental studies conducted by Thouless et al. (1998). Numerical simulation and scaling analyses are conducted here based on the nonlinear elastoplastic loading and unloading moment –curvature relations (3.11) and (3.12).

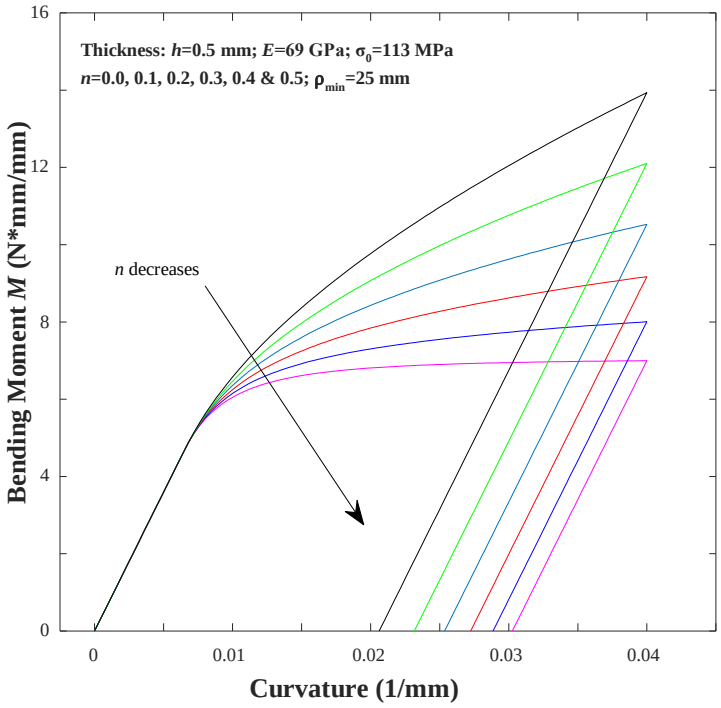

(a)

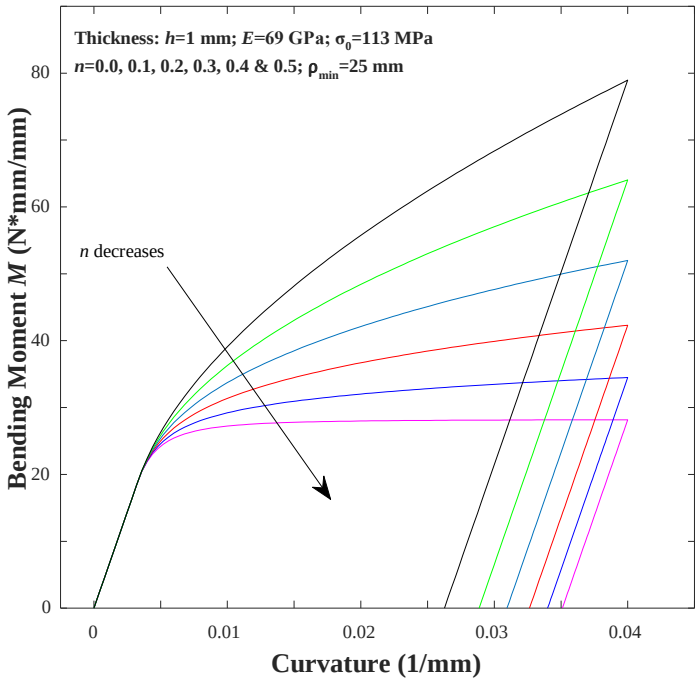

(b)

Figure 3.6. Nonlinear elastoplastic loading and unloading moment-curvature diagrams of aluminum alloy beams with varying hardening index *n*

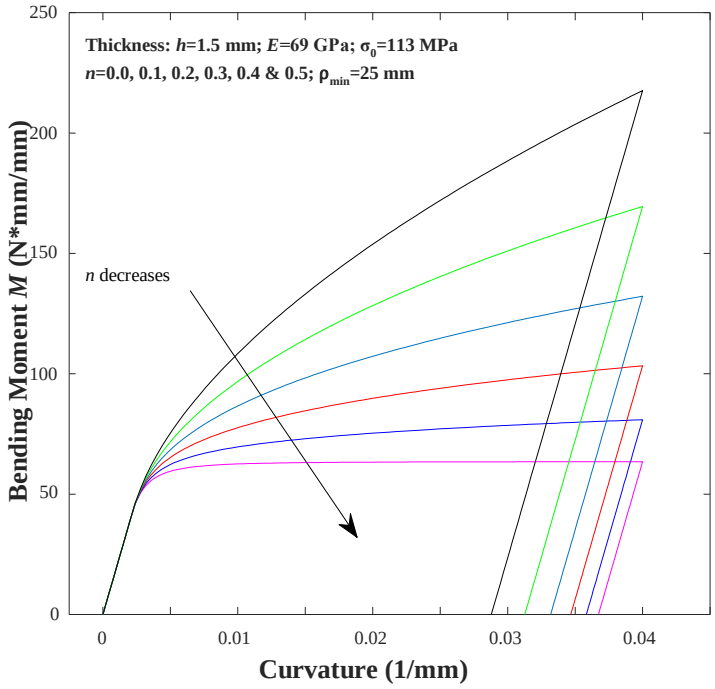

(c)

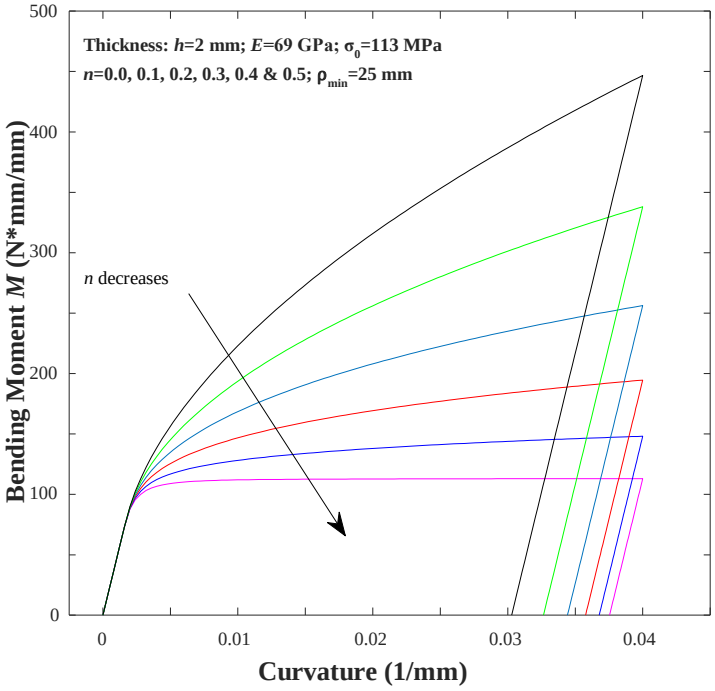

(d)

Figure 3.6. Nonlinear elastoplastic loading and unloading moment-curvature diagrams of aluminum alloy beams with varying hardening index *n* (continued)

Figs. 3.6 and 3.7 represent the nonlinear elastoplastic moment curvature diagrams for aluminum alloy and mild steel beams, respectively. It is noted that, both types of beams show the similar moment –curvature behaviors with varying hardening indices *n*. Each moment-curvature diagram can be described in terms of three regions, i.e. in the beginning, a linear elastic region, the power-law strain-hardening region, and finally elastic unloading of elastic springback. Given the hardening index *n*, the increase of the beam thickness *t* results in the increase of loading moment *M* in terms of beam curvature $1/\rho$. Then, for given the beam thickness *t*, the decrease of the hardening index *n* results in the decrease of the loading moment in terms of curvature $1/\rho$, due to the softening behavior of materials with decreasing *n*. However, in the case of idealized elastoplastic solid, i.e., $n = 0$, the bending moment *M* of both aluminum and mild steel beams tend to be constant after yielding. In addition, it is also noticed from Figs. 3.6 and 3.7 that, the effect of springback decreases with decreasing hardening index *n*. In conclusion, a large hardening index *n* corresponds to a large elastic springback, i.e., a large strain energy release in the unloading range.

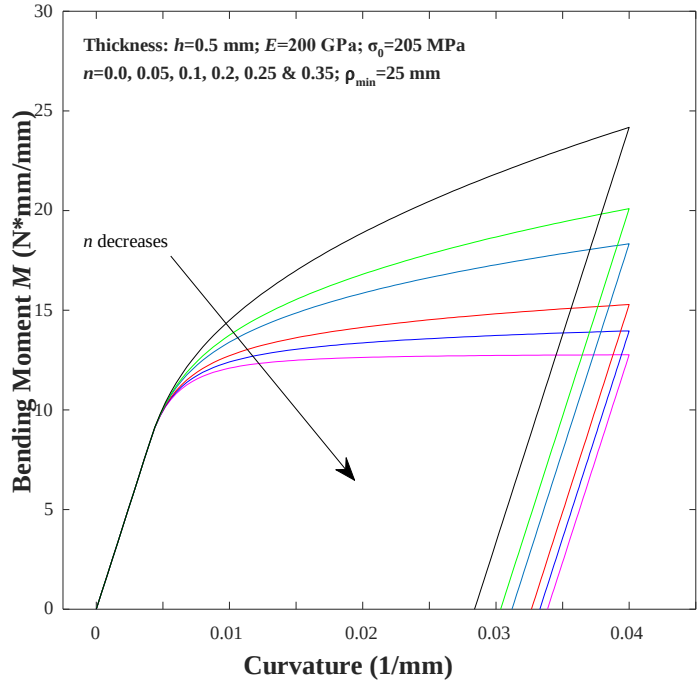

(a)

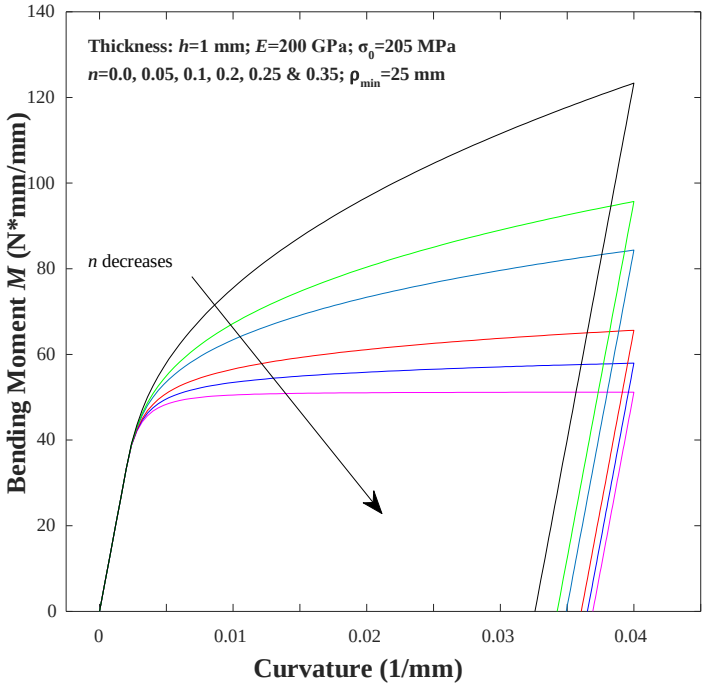

(b)

Figure 3.7. Nonlinear elastoplastic loading and unloading moment-curvature diagrams of mild steel beams with varying hardening index *n*

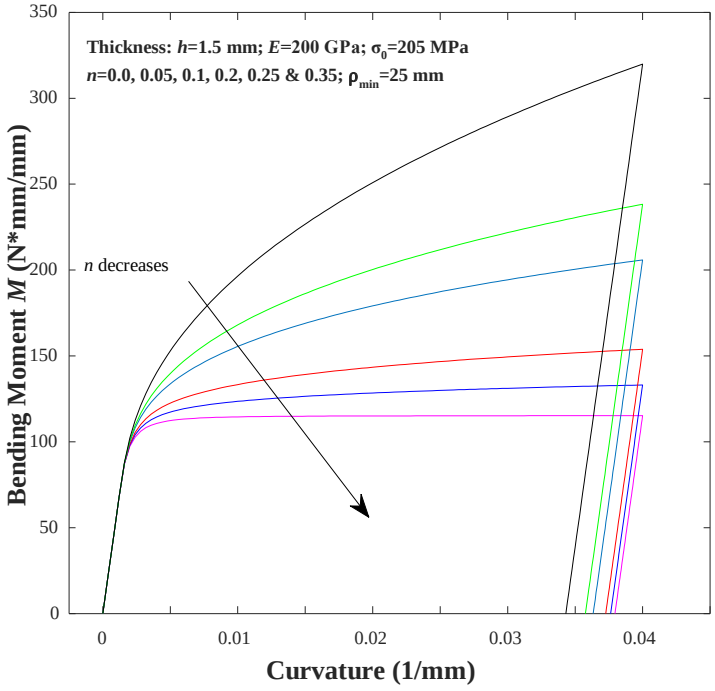

(c)

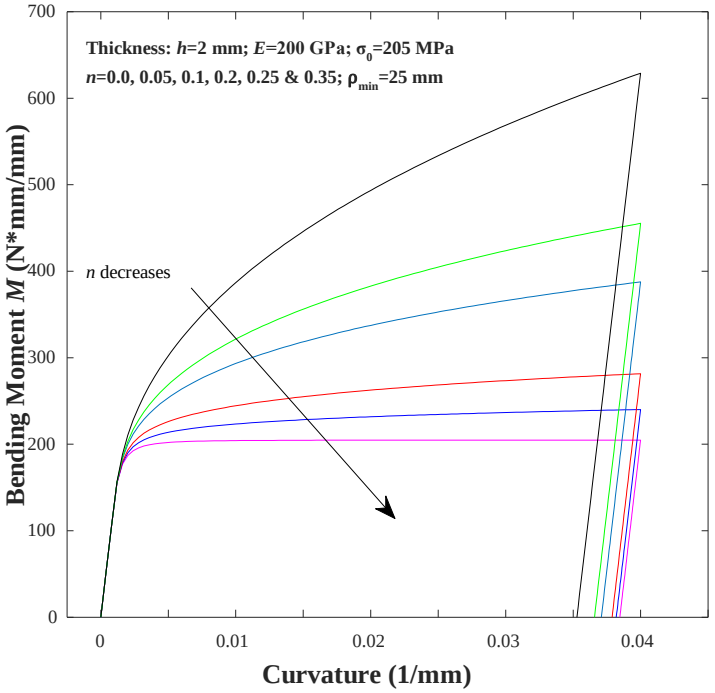

(d)

Figure 3.7. Nonlinear elastoplastic loading and unloading moment-curvature diagrams of mild steel beams with varying hardening index *n* (continued)

The present elastoplastic beam model is further used to perform the scaling analysis of the springback of ABJs made of aluminum alloy and mild steel beams with varying strain hardening indices *n*. Eq. (3.9) is employed for the numerical simulations to determine the correlation of the minimum radius of the curvature ρ_m at the maximum bending moment $M(\rho_m)$ to the radius after complete springback ρ_0. Figures 3.8 and 3.9 show the diagrams of ρ_m as a function of ρ_0 at varying index *n* of the aluminum alloy and mild steel beams, respectively.

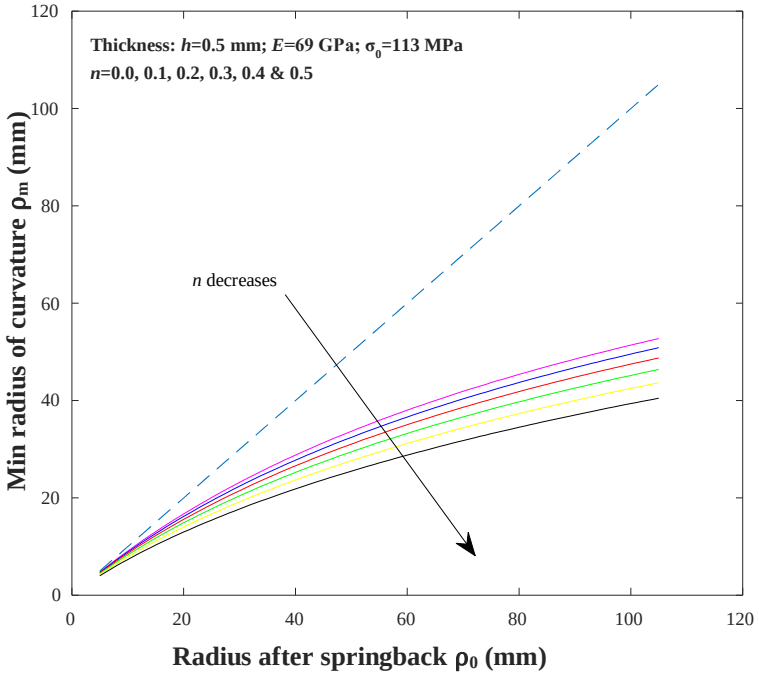

(a)

Figure 3.8. Variations of the minimum radius of curvature ρ_m with respect to the radius after springback ρ_0 of aluminum alloy beams with varying hardening index *n* (Dashed line represents the diagonal for comparison)

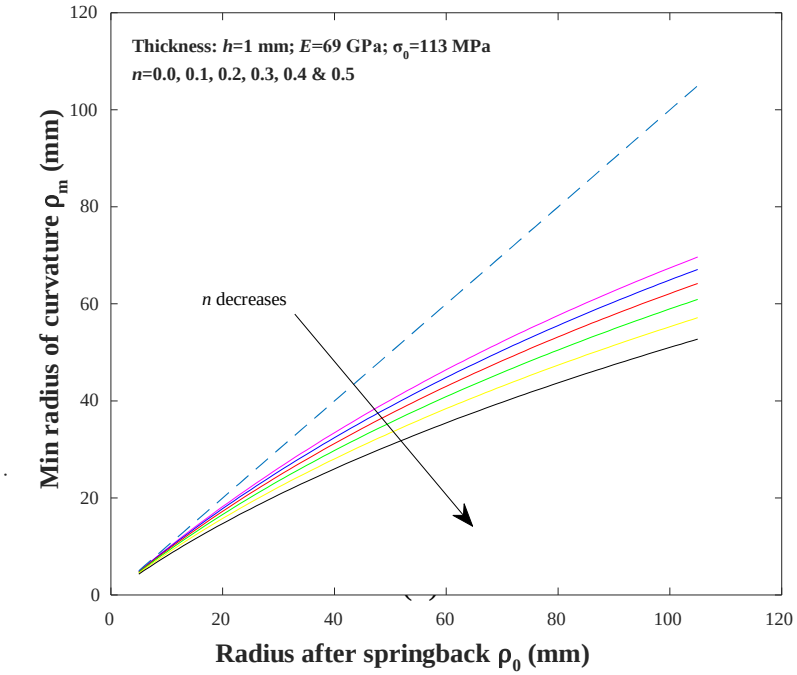

(b)

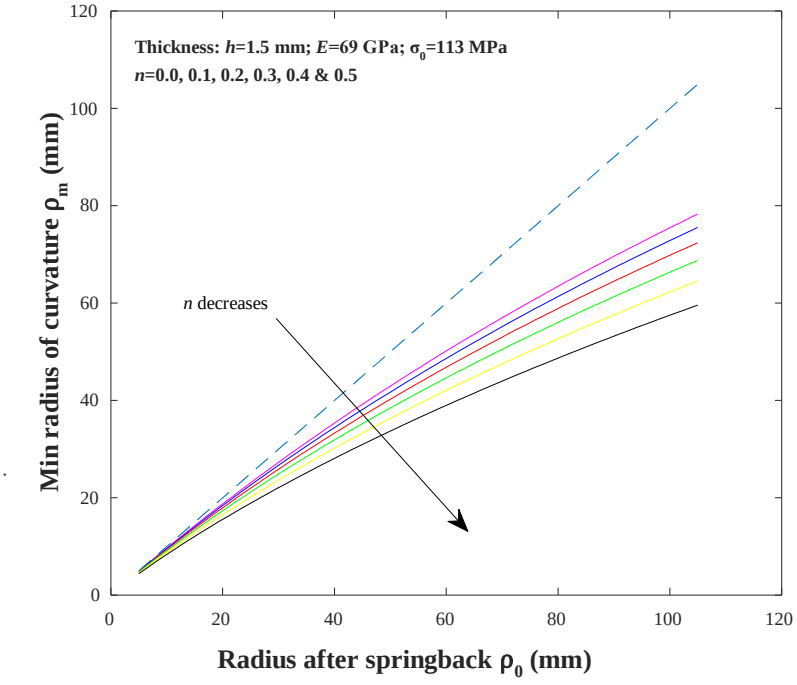

(c)

Figure 3.8. Variations of the minimum radius of curvature ρ_m with respect to the radius after springback ρ_0 of aluminum alloy beams with varying hardening index n (Dashed line represents the diagonal for comparison) (continued)

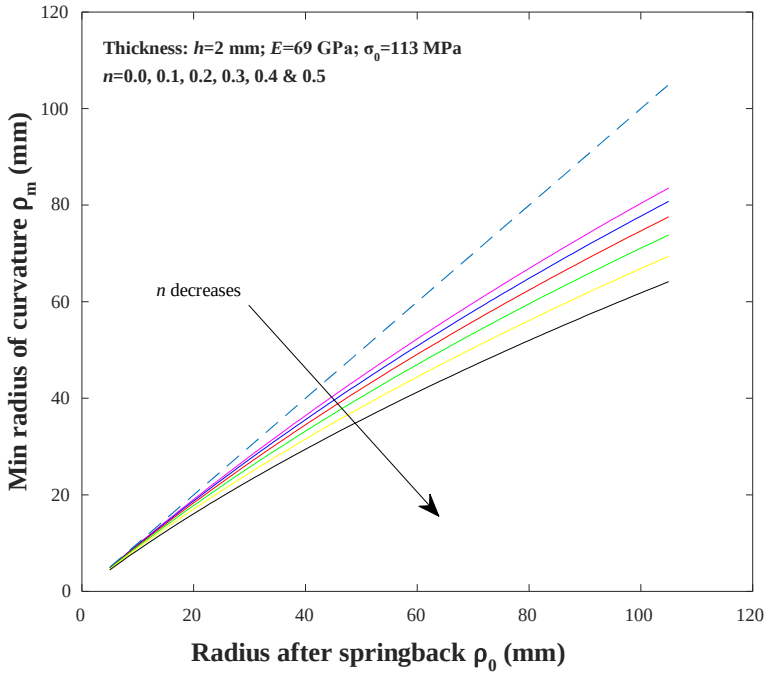

(d)

Figure 3.8. Variations of the minimum radius of curvature ρ_m with respect to the radius after springback ρ_0 of aluminum alloy beams with varying hardening index n (Dashed line represents the diagonal for comparison) (continued)

All the beam geometries and material properties are taken as the same as those used in Figs. 3.6 and 3.7. It can be noted from Figs. 3.8 and 3.9 that the tendency of general variations are similar for both the aluminum alloy and mild steel ABJs. When the radius after complete springback ρ_0 and the thickness of the arm t are fixed, the increase of the hardening index n results in the increase of minimum radius of curvature ρ_m at the maximum bending moment M. This is due to the fact that, a lower value of the hardening index n represents a lower increase of stress level or a more plastically deformed ABJ, i.e., a lower ρ_m. In addition, when the radius after springback ρ_0 and the material hardening index n are fixed, the increase of the arm thickness t results in the increase of minimum radius of curvature ρ_m at the maximum bending moment M. This is quite reasonable as the thicker the elastoplastic specimens are, the higher the chance to

exhibit more noticeable springback. In the limiting case of idealized elastoplastic solid, i.e., n= 0, the minimum springback appears and in the limiting case of linearly elastic solids (n= 1) or nonlinearly elastic solids, after unloading, the adherends completely recover the original configuration, i.e., the maximum springback.

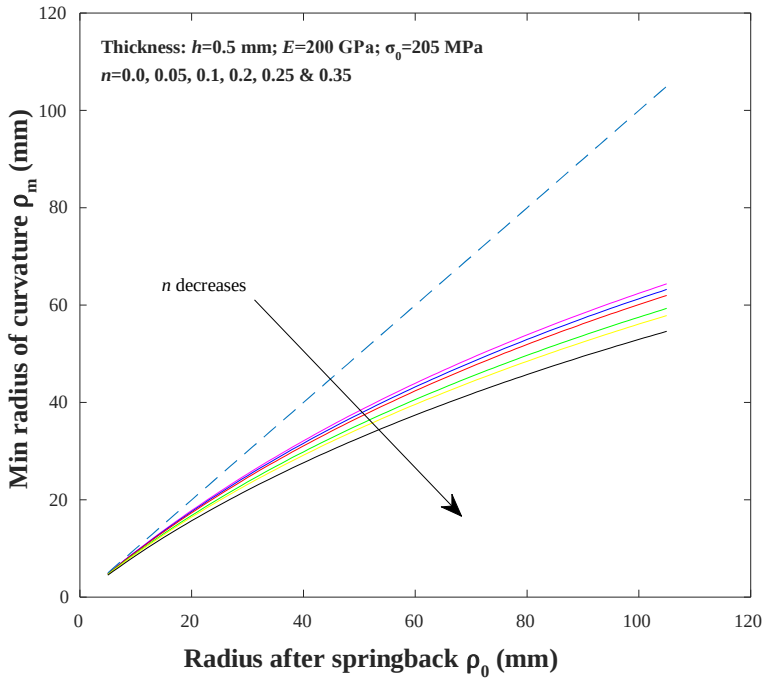

(a)

Figure 3.9. Variations of the minimum radius of curvature ρ_m with respect to the radius after springback ρ_0 of mild steel beams with varying hardening index n (Dashed line represents the diagonal for comparison)

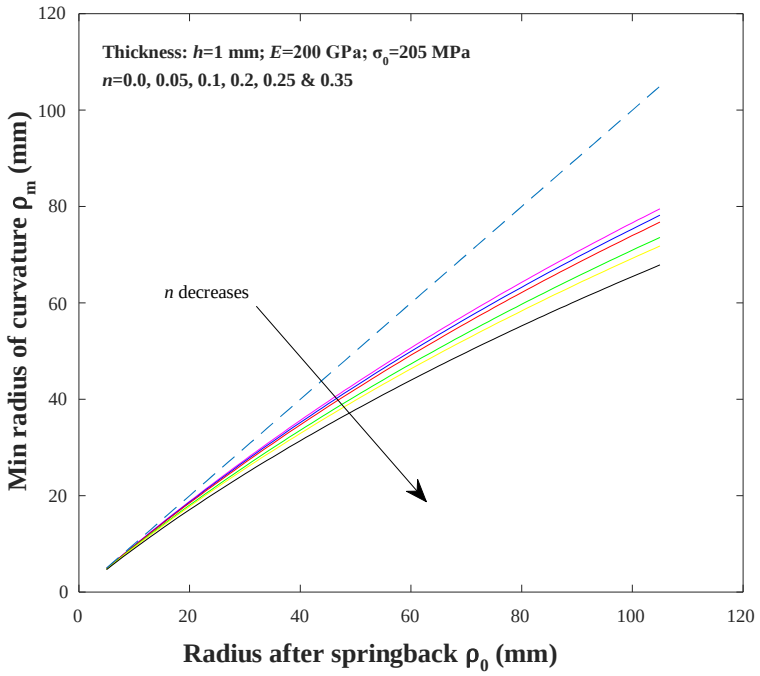

(b)

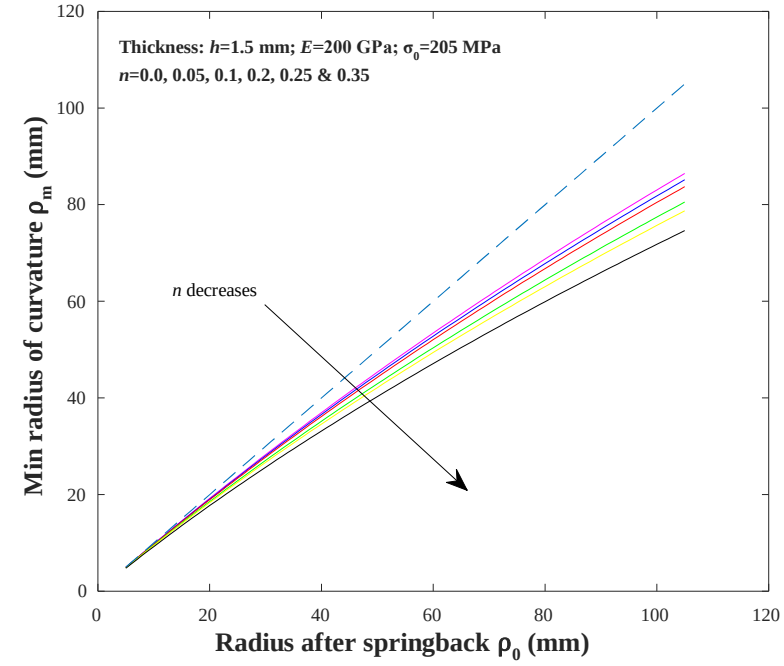

(c)

Figure 3.9. Variations of the minimum radius of curvature ρ_m with respect to the radius after springback ρ_0 of mild steel beams with varying hardening index n (Dashed line represents the diagonal for comparison) (continued)

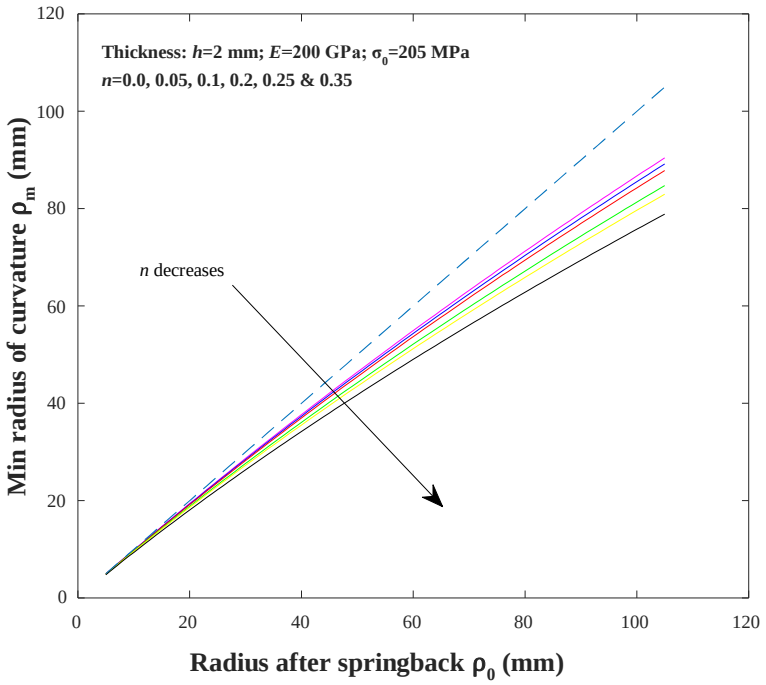

(d)

Figure 3.9. Variations of the minimum radius of curvature ρ_m with respect to the radius after springback ρ_0 of mild steel beams with varying hardening index n (Dashed line represents the diagonal for comparison) (continued)

Finally, the present model is also used to determine the fracture toughness of ABJs made of aluminum alloy and mild steel beams with varying hardening indices n. The numerical simulations herein are conducted according to relation (3.23) of the theoretical fracture toughness of ABJs Γ per unit width l of the specimen beam and radius after complete springback ρ_0. Figures 3.10 and 3.11 show the diagrams of Γ as a function of ρ_0 at varying index n of the aluminum alloy and mild steel beams, respectively.

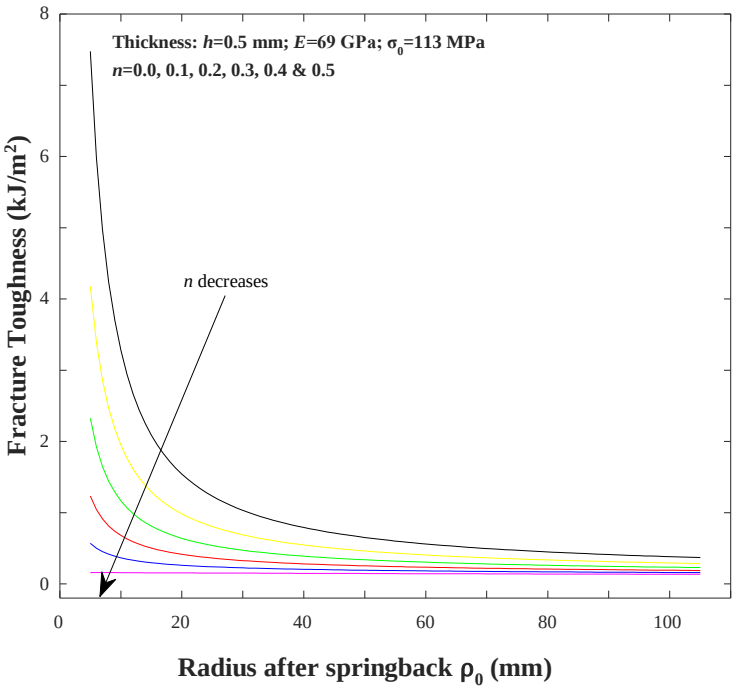

(a)

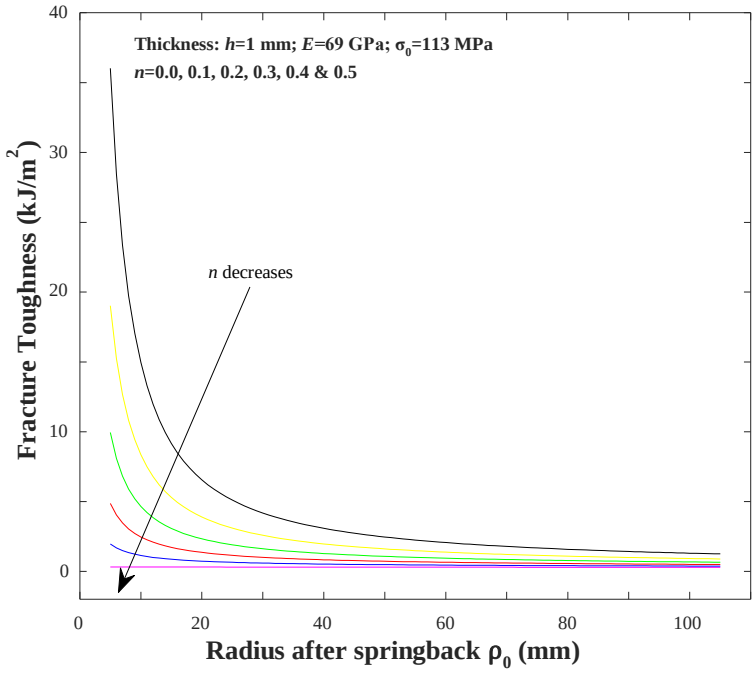

(b)

Figure 3.10. Variations of the fracture toughness Γ with respect to the radius after springback ρ_m of aluminum alloy beams with varying hardening index *n*

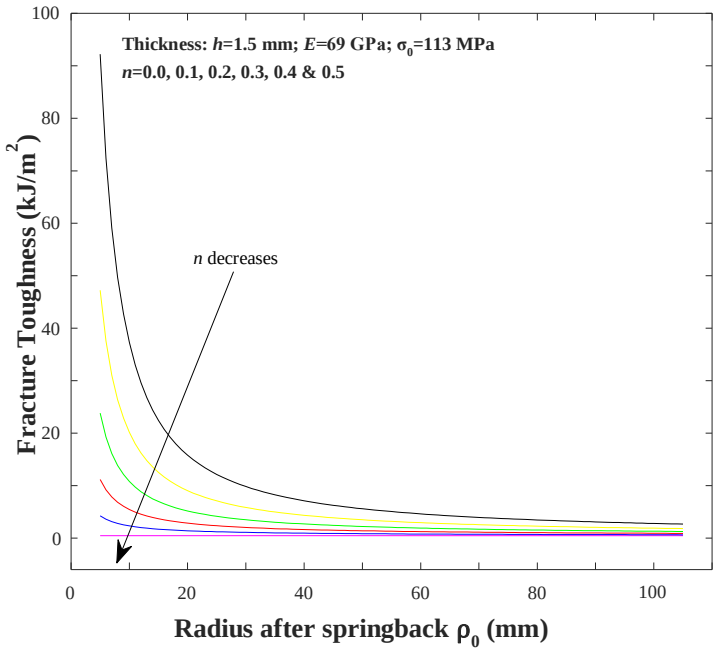

(c)

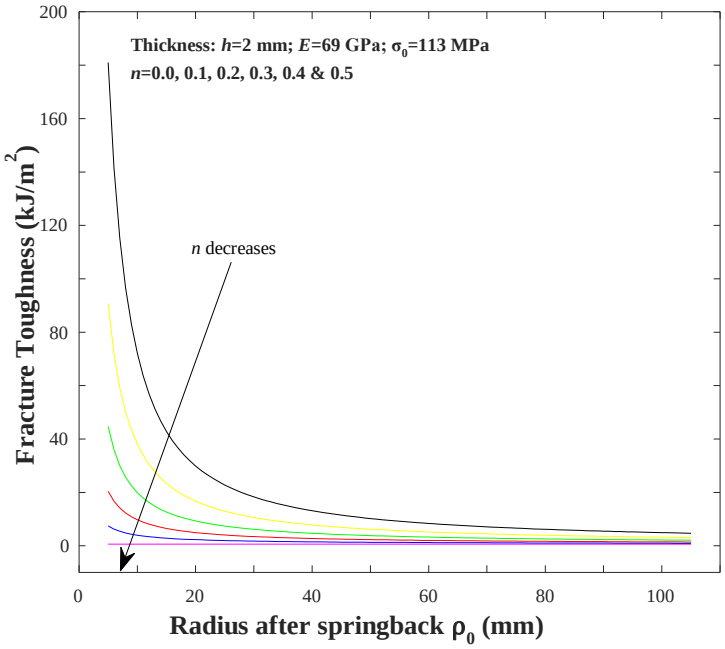

(d)

Figure 3.10. Variations of the fracture toughness Γ with respect to the radius after springback ρ_m of aluminum alloy beams with varying hardening index *n* (continued)

All the adherend geometries and material properties are taken as the same as those used in Figs. 3.8 and 3.9. It can be noted from Figs. 3.10 and 3.11 that the tendency of general variations are similar for both the aluminum alloy and mild steel ABJs. When the radius after springback ρ_0 and the thickness of the arm t are fixed, the increase of the hardening index n results in the increase of fracture toughness of the ABJs Γ. This is due to the fact that, a higher value of hardening index n implies a higher $M(\rho_m)$ is required to generate the given ρ_0. In addition, when the radius of curvature after springback ρ_0 and the material hardening index n are fixed, the increase of the adherend thickness t results in the increase of fracture toughness of the ABJs Γ due to the fact that a thicker elastoplastic specimen requires the higher $M(\rho_m)$ to advance the crack growth and hence a higher value of fracture toughness Γ is involved.

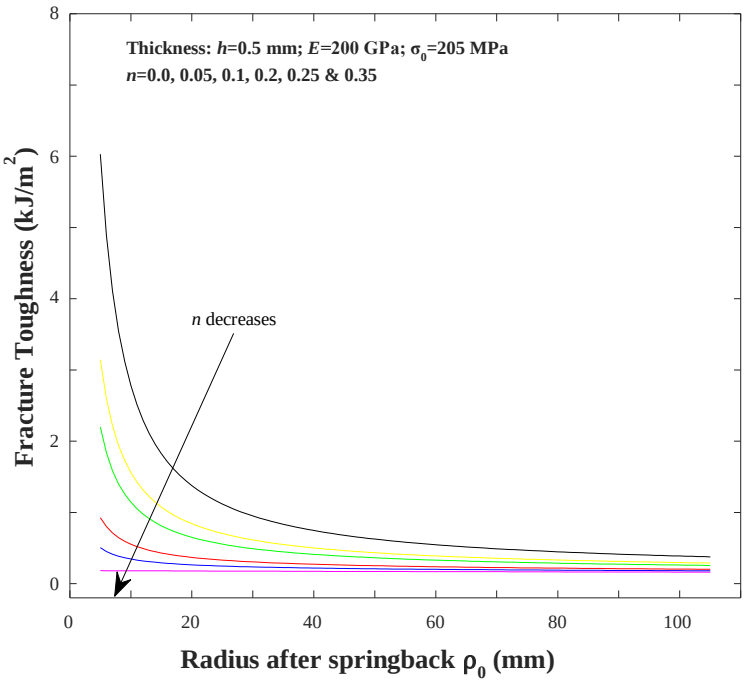

(a)

Figure 3.11. Variations of the fracture toughness Γ with respect to the radius after springback ρ_m of mild steel beams with varying hardening index n

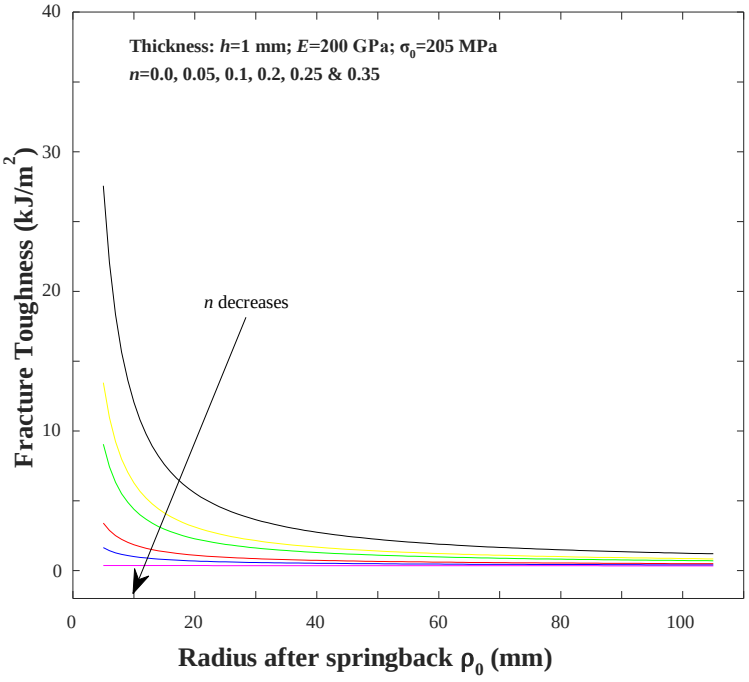

(b)

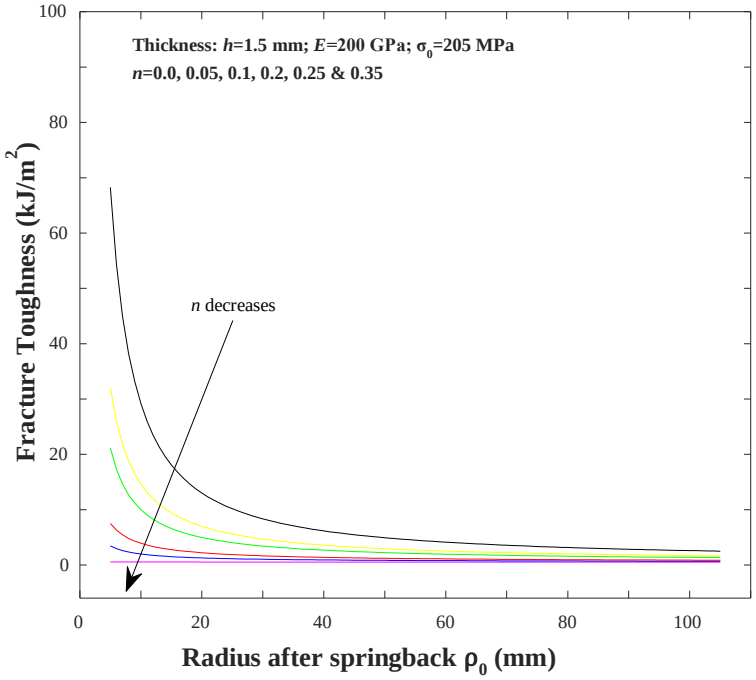

(c)

Figure 3.11. Variations of the fracture toughness Γ with respect to the radius after springback ρ_m of mild steel beams with varying hardening index *n* (continued)

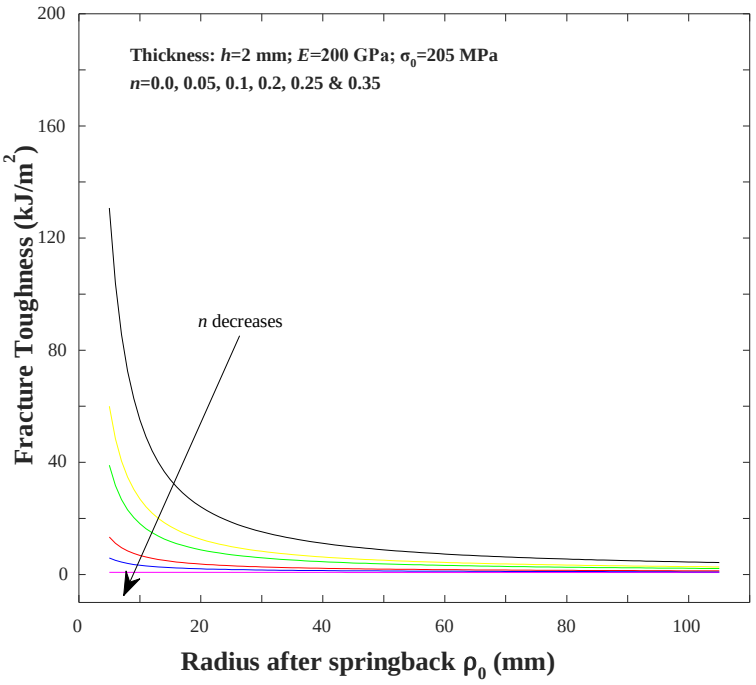

(d)

Figure 3.11. Variations of the fracture toughness Γ with respect to the radius after springback ρ_m of mild steel beams with varying hardening index *n* (continued)

3.3. Concluding Remarks

A nonlinear elastoplastic model has been formulated for the determination of the fracture toughness of ABJs with large plastic deformations and afterward springback. Aluminum alloy and mild steel beams with varying thickness *t* and strain hardening indices *n* have been considered as the example ABJs for the present study. In the present model, the maximum curvature $1/\rho_m$ and its corresponding maximum bending moment M (ρ_m) have been calculated based on the measured radius of curvature ρ_0 after complete elastic springback, which are considerably different from those given by other nonlinear elastic models with the springback effect neglected. The strain energy stored in the elastoplastic adherends of the ABJs can be determined into three stages, i.e., the linear loading, nonlinear elastoplastic loading, and springback or linear unloading stages.

Without additional *ad hoc* simplifications and assumptions, the present model is capable of predicting the accurate value of fracture toughness of ABJs as the present ABJ model has rationally taken into account the effects of the accurate elastoplastic deformations and elastic springback after complete unloading. The present elastoplastic ABJ model has several advantages superior to those available in the literature: (1) the power-law strain-hardening elastoplastic material model can accurately describe the elastoplastic behavior of metal ABJs including those made of aluminum alloys and mild steels in this study, (2) Both the maximum bending moment M (ρ_m) to drive the crack growth and the maximum curvature $1/\rho_m$ after complete unloading have been determined with taking into account the elastic springback effect; (3) The maximum curvature $1/\rho_m$ has been used to determine the accurate fracture toughness of ABJs based on the work ΔW done by the driving moment and the strain energy ΔU stored in the adherends in the present model.

Furthermore, the present elastoplastic model has been used for detailed scaling analysis of the effect of the geometries and mechanical properties on elastic springback and the predicted fracture toughness of ABJs with varying adherend thickness t and hardening index n. This present model is useful to determine the effects of the governing parameters on the failure and design of ABJs with improved accuracy. This model can also be useful for the analysis of adhesive failure and fracture analysis of thin metallic structures and films with large nonlinear plastic deformation and afterward springback such as, metal machining, peeling in coatings, and failure of thin ductile metals, among others.

4. CZM-BASED COMPUTATIONAL SIMULATIONS OF THE FULL-RANGE DEBONDING PROCESS OF ABJS

4.1. Introduction

High stress concentration at the free edges of ABJs is responsible for debonding failure in ABJs when subjected to an external thermal and/or mechanical loading. In this chapter of the thesis, CZM based FEA is to be used for investigating the full range debonding initiation and propagation process of ABJs. In specific, the effects of geometries, material properties, and debonding toughness of adhesive layers on the global load carrying capacity of an adhesively bonded single-sided strap joint (ABSSSJ) are examined in detail. The debonding initiation at the free edges of ABJs is governed by the cohesive law in terms of the critical peeling and shearing debonding toughness. The results of this computational study show that the critical tensile force to trigger the debonding initiation of ABSSSJs increases with the increase of debonding toughness whereas decreases slightly with the increase of adhesive layer thickness. However, the effective longitudinal stiffness of the ABSSSJs remains nearly independent of adhesive elastic modulus and decreases with the increase of adhesive layer thickness. In addition, the characteristic load-displacement diagram of ABSSSJs when subjected to an external tensile loading, exhibits a flat yield range corresponding to the stable debonding process which represents the excellent mechanical strength and durability of ABSSSJs during the entire debonding failure process. The present computational studies demonstrate the capability of CZM-based FEA for the prediction of effective load-carrying capacity of ABJs during the entire process of debonding initiation and propagation till to the final failure, which are practically important for the exploration and determination of failure mechanisms, design and manufacturing, and extension of the mechanical durability of ABJs.

4.2. Problem Formulation and Solutions

In this computational study, without loss of generality, an adhesively bonded single-sided strap joints (ABSSSJs) made of two adhesively bonded structural steel and aluminum alloy adherends is considered. As illustrated in Fig. 4.1, the upper adherend has the length 2L, thickness h_1 and width b; the lower adherend has the length much larger than L, thickness h_2 and width b; the thickness of the adhesive is allowed to vary for the scaling analysis of the force-displacement behaviors of the ABSSSJs.

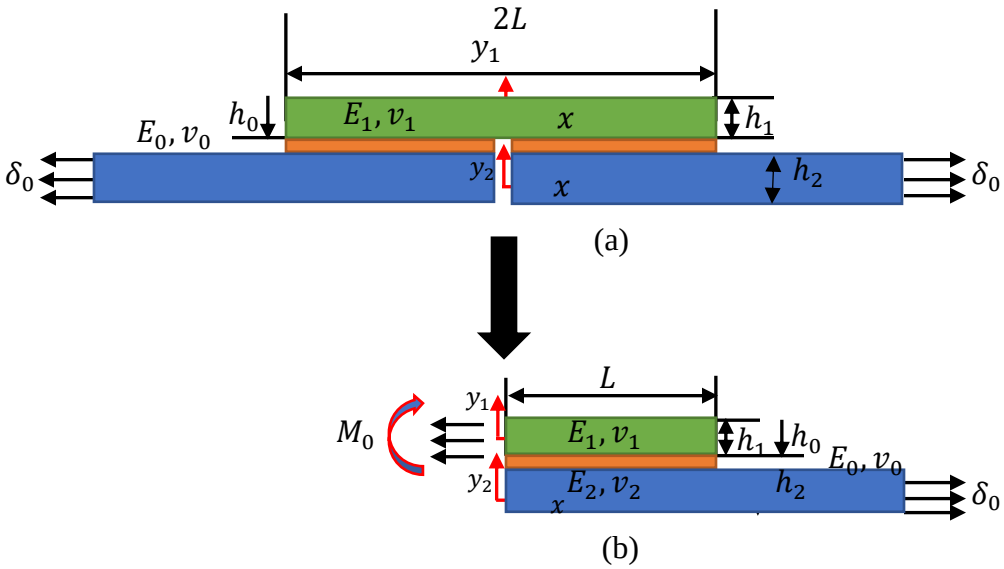

Figure 4.1. Schematic of (a) adhesively bonded single-sided strap joint (ABSSSJ), and (b) reduced half symmetric portion for analysis

Axial elongation is applied through the centroidal axis of the two lower adherends and the movement in tangential direction has been set as 0 (zero). The computational simulation is conducted only on the right half portion of ABSSSJ due to its symmetric geometries and boundary conditions. The characteristic force-displacement behaviors of ABSSSJ at varying material properties and geometries are determined during the entire debonding process. However, before

this, most of the literature studies were concentrated on determining the stress field and stress concentrations of ABJs subjected to the applied thermal and mechanical loads.

4.2.1. Model Formulation and Implementation

Due to the symmetry of the ABSSSJ, the analysis is performed on the right-half portion of the entire geometric structure. In principle, the high interfacial peeling and shear stresses are responsible for the failure of ABSSSJs, which rely on the external loads as well as the geometries and material properties of the bonded materials. In the present study, plane stress state is assumed and no temperature change is considered. Mixed-mode debonding criterion is used and cohesive zone is implied along the upper and lower bonding lines. Uniform refined mesh with assembly level meshing technique has been adopted where the minimum size for mesh smoothing is used as 0.16 mm. Scaling analysis of the force-displacement relation at varying adhesive thickness and material properties during the entire debonding process of ABSSSJs is conducted.

4.2.2. Scaling Analyses of the Force-Displacement Behaviors of ABSSSJs

The interfacial shear and normal stresses at both the upper and lower interfaces between the adherends and adhesive layer are responsible for the debonding failure and, which have been determined accurately by means of various theoretical and computational methods including the recent high-efficient, accurate stress-function variational methods by Wu and Jenson (2011) and Wu and Zhao (2013) as shown in Fig. 4.2. These studies represent the fact that normal stresses are much higher in the upper interface compared to that of lower interface which provide some rational understandings of the fact that the region for potential failure might exist in the upper adherend-adhesive layer interface. Although, accurate stress analyses can be performed using stress-function

variational method, full-range debonding initiation and growth process in ABJs is still beyond the reach of this model which the present computational study tries to resolve using CZM-based FEM.

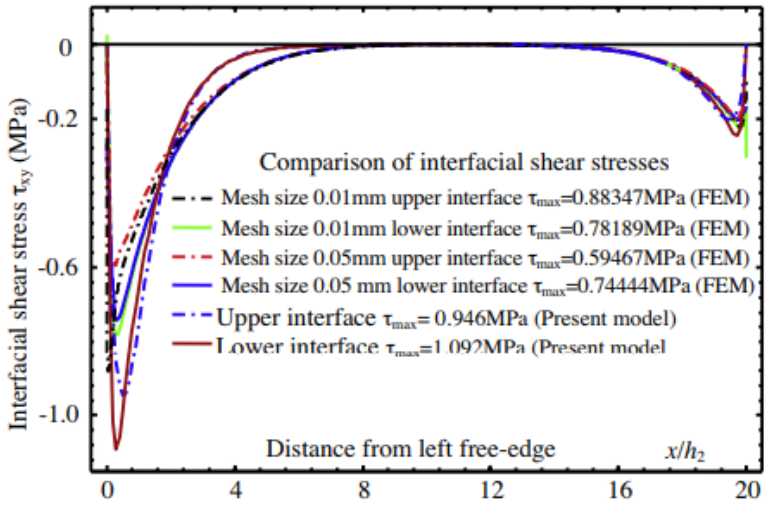

(a)

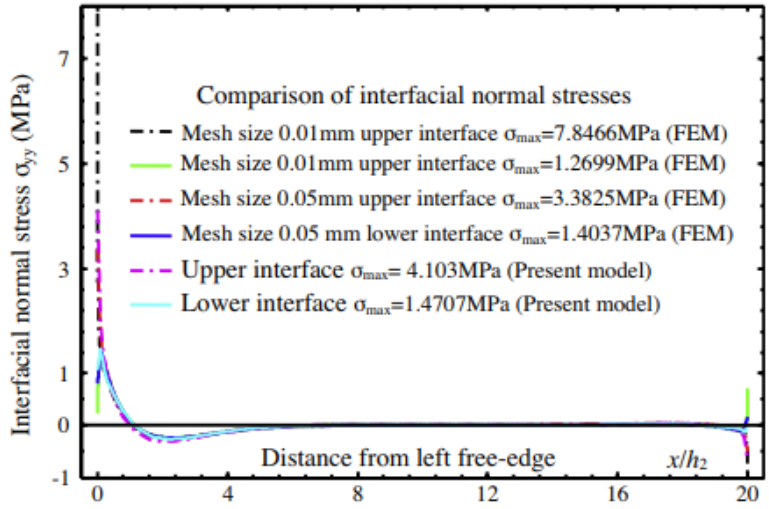

(b)

Figure 4.2. Validation of the stress-function variational method by FEA: (a) interfacial shear stress τ and (b) interfacial normal stress σ (Wu and Jenson, 2011; Wu and Zhao, 2013)

In this study, the main focus is made on determination of the full-range force-displacement relation during the entire debonding process of ABSSSJs. CZM is adopted at the upper and lower

bonding lines of the ABSSSJ under the current consideration. Commercially available FEA software package ANSYS^{TM} is utilized for the present CZM-based FEA of the debonding process of the ABSSSJs. The material dimensions of both adhesive and adherends for this CZM-based FEA are taken from Wu and Zhao (2013) and can be shown in Fig. 4.3.

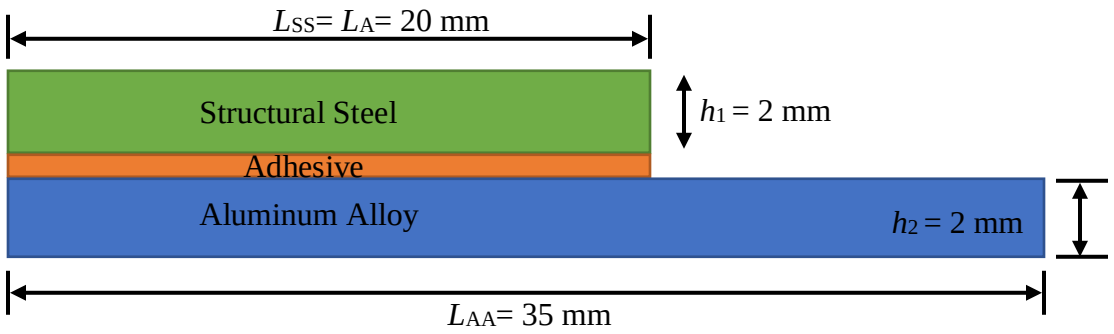

Figure 4.3. Schematic of the ABSSSJ specimen used for CZM-based FEA

During the computational modeling, the material properties of the adherends and the adhesive layers of the ABSSSJs are treated as linearly elastic materials as follows:

(a) Upper adhered: Structural steel- with Young's modulus 210 GPa and Poisson's ratio 0.3;

(b) Adhesive layers: Epoxy with yield strength 40 MPa, Poisson's ratio (0.48), and Young's modulus varying in different simulation cases.

(c) Lower adherends: Aluminum alloy – with Young's modulus 71 GPa and Poisson's ratio 0.33.

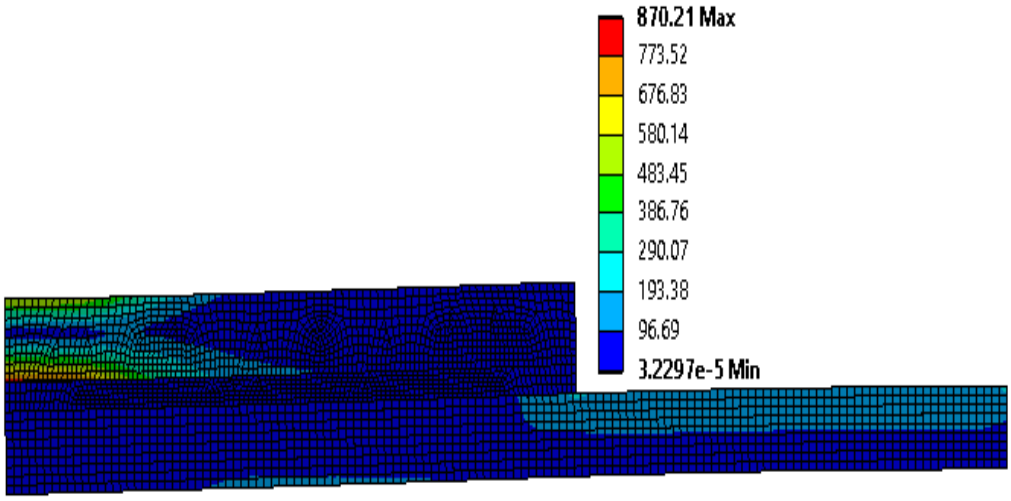

Figure 4.4. Stress contour of single sided adhesively bonded joints before crack initiates

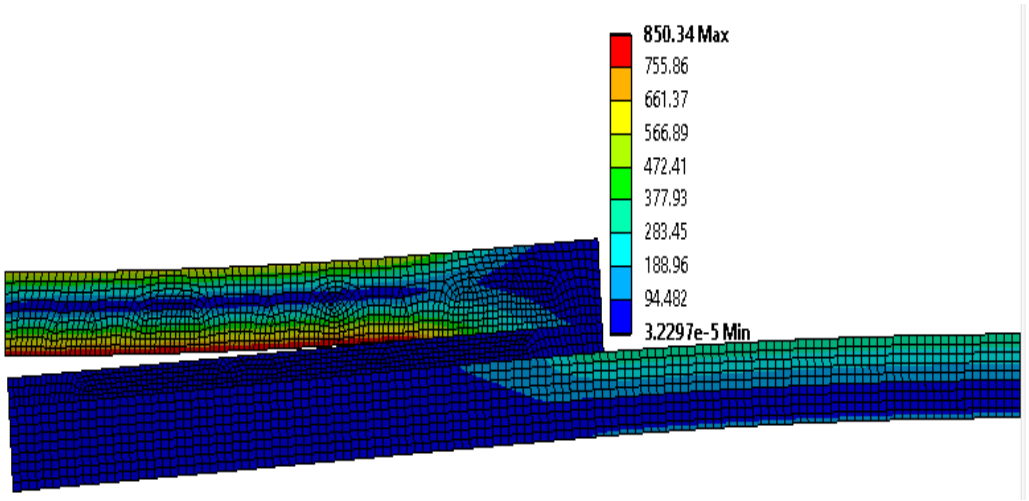

Figure 4.5. Typical stress contour of a debonded ABSSSJ

To implement the CZM-based FEA of the ABSSSJs by using ANSYS®, plane-stress 4-node structural solid elements (ANSYS 182) with quadrilateral uniform refined meshes are employed at the regions at the upper and lower bonding lines. The present CZM-based FEA is made such that the bonding interface gradually detaches with increasing axial elongation according to debonding criterion designated by the cohesive law of bonding interfaces. Peak cohesive stress

during the simulation is specified as the yield stress (40 MPa) of the adhesive. ANSYS® uses finite element method to solve contact nonlinearity problems via two basic theories. One of them is penalty formulation method, and the other is known as Lagrange multipliers method. Although they are different in their approaches, both of them lead to a desired solutions (Stefancu et al, 2011). Therefore, in this study, pure penalty formulation method with uniform refined mesh size is applied in the cohesive zone along the bonding lines of ABSSSJs. Besides, the criterion for convergence, stiffness of element, number of steps and all object nonlinearity options are set as default programs in ANSYS®.

4.2.2.1. Force-Displacement Relations at Varying Cohesive Fracture Energy

The Von-Mises stress contour presented in Fig. 4.5 indicates that the debonding initiation is happened in the upper adherend and adhesive layer interface rather than the interface between adhesive layer and lower adherend which clearly supports the stress-function variational method proposed by (Wu and Jenson, 2011; Wu and Zhao, 2013). Fracture toughness has a noticeable impact on the characteristic force-displacement behavior of ABJs. For instance, single-sided adhesively bonded joints have the relationship between the cohesive fracture toughness and the corresponding tensile failure force can be expressed as

$$G_c = \frac{\pi {\sigma_f}^2 a}{E}, \tag{4.1}$$

$$\sigma_f = \frac{F}{A}, \tag{4.2}$$

where G_c denotes the critical energy release rate (fracture toughness) or cohesive fracture energy and σ_f denotes the peak cohesive strength. Therefore, increase of the cohesive energy leads to the increase of cohesive force to initiate the crack growth and therefore contributes to the final failure.

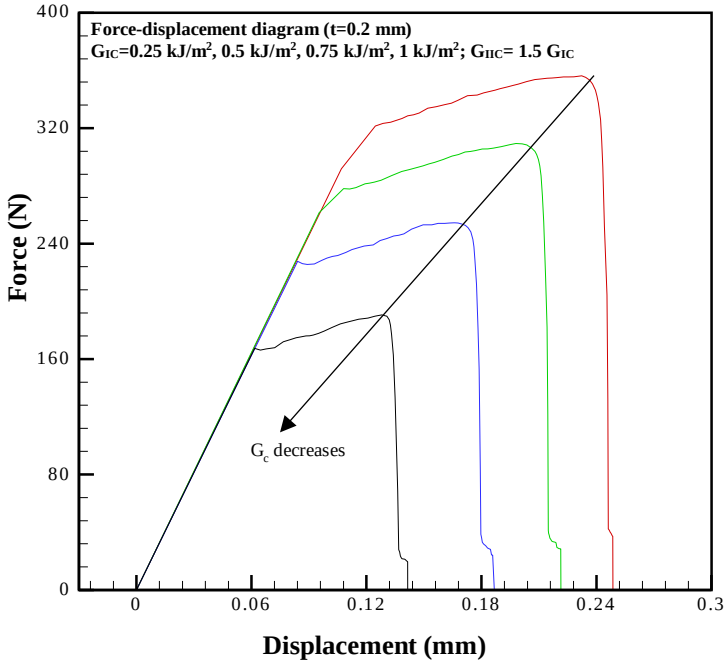

(a)

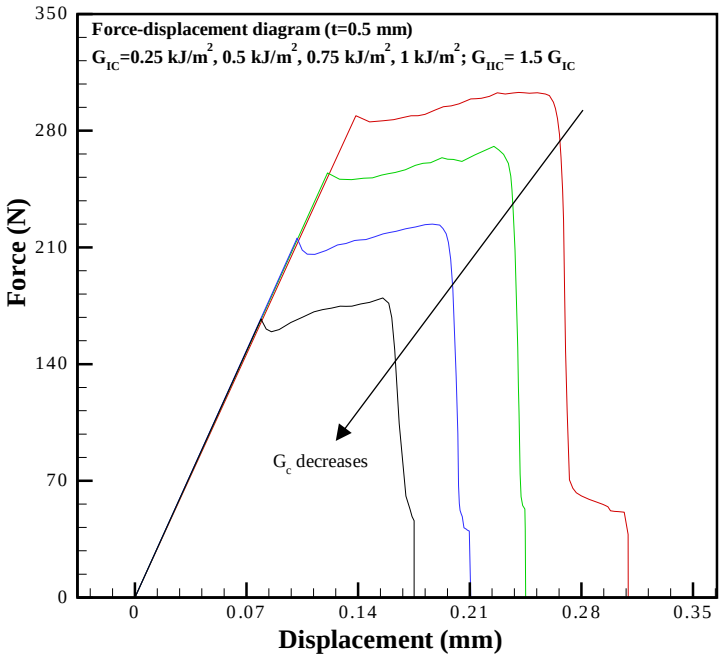

(b)

Figure 4.6. Predicted force-displacement diagrams of ABSSSJs with varying fracture toughness *G*c

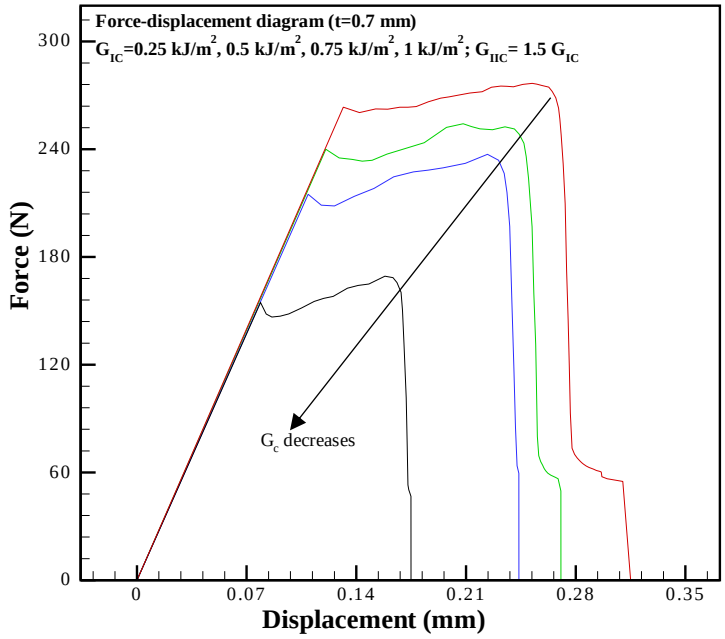

(c)

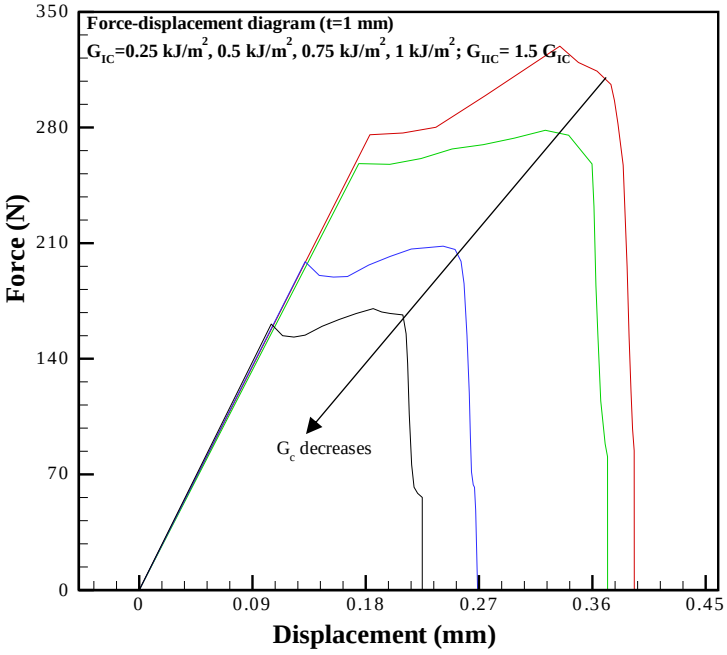

(d)

Figure 4.6. Predicted force-displacement diagrams of ABSSSJs with varying fracture toughness *G*c (continued)

Varying cohesive energy of ($G_{IC} = 0.25\frac{kJ}{m^2}, G_{IIC} = 1.5G_{IC}\frac{kJ}{m^2}$); ($G_{IC} = 0.5\frac{kJ}{m^2}, G_{IIC} = 1.5G_{IC}\frac{kJ}{m^2}$); ($G_{IC} = 0.75\frac{kJ}{m^2}, G_{IIC} = 1.5G_{IC}\frac{kJ}{m^2}$) and ($G_{IC} = 1.0\frac{kJ}{m^2}, G_{IIC} = 1.5G_{IC}\frac{kJ}{m^2}$) are applied whereas the adhesive elastic modulus E=10 GPa and other cohesive properties are considered as fixed. The peak cohesive stress of the cohesive zone model is assumed to be the same as adhesive yield strength 40 MPa. Increase of fracture toughness G_C increases the peak cohesive force of the joint. ABSSSJ with $G_{IC} = 1.0\frac{kJ}{m^2}, G_{IIC} = 1.5G_{IC}\frac{kJ}{m^2}$ behaves the highest yield and ultimate force whereas ABSSSJ with $G_{IC} = 0.25\frac{kJ}{m^2}, G_{IIC} = 1.5G_{IC}\frac{kJ}{m^2}$ predicts the lowest (Fig. 4.6). Varying adhesive thicknesses (t= 0.2 mm, 0.5 mm, 0.7 mm and 1 mm) are further taken into account. In each case of the adhesive thickness, the characteristic force-displacement behavior shows the consistent and similar behaviors as the thinner adhesive layers. Thus, based on the variations of cohesive fracture energy, the present scaling study shows that the adhesive layer with a lower thickness is essential for higher material strength and therefore, to provide the higher load-carrying capacity before catastrophic failure of the joints.

4.2.2.2.Force-Displacement Relations at Varying Adhesive Elastic Modulus

Elastic modulus is a fundamental material property that influences the joint design and failure. Elastic modulus of a certain material and cohesive strength of a certain system are related to each other as

$$\sigma_C = \sqrt{\frac{E\gamma_s}{x_0}}, \tag{4.3}$$

$$E = \frac{{\sigma_f}^2 x_0}{\gamma_s}, \tag{4.4}$$

where, σ_c denotes the cohesive stress, E denotes the elastic modulus of the material, γ_s is the surface energy density and x_0 is the gauge length of the cohesive spring. Therefore, the above relation indicates that the increase of material elastic modulus contributes to the increase of peak cohesive stress and hence, increases the peak cohesive force or yield force. Validation of this conceptual understanding with the numerical simulations and the corresponding scaling analysis results is discussed below.

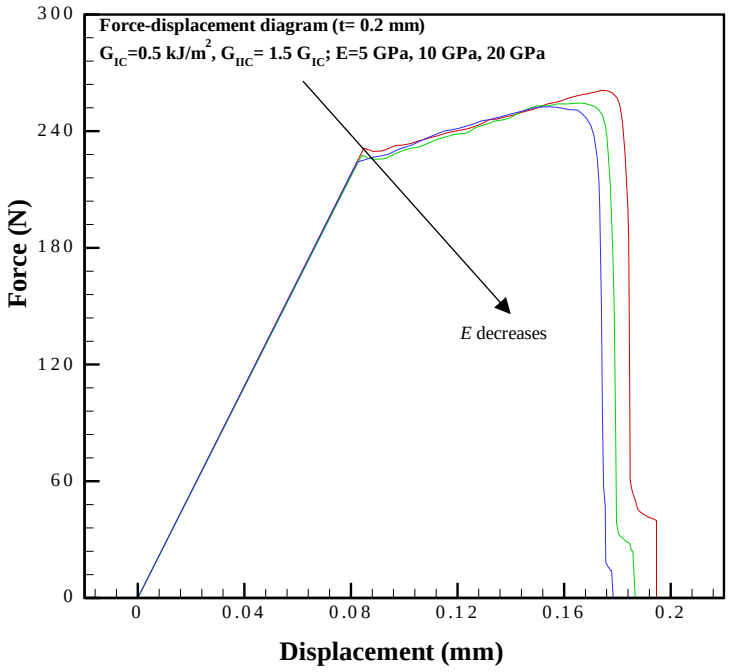

(a)

Figure 4.7. Predicted force-displacement diagrams at varying adhesive elastic modulus *E*

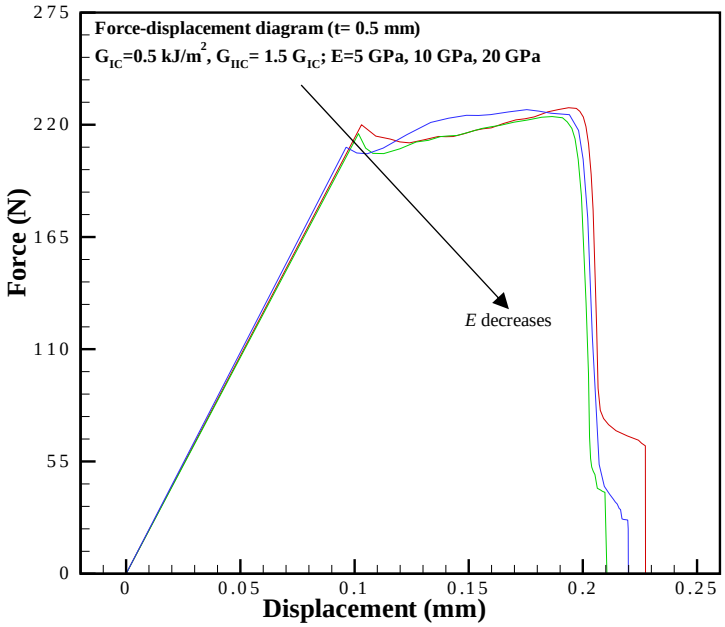

(b)

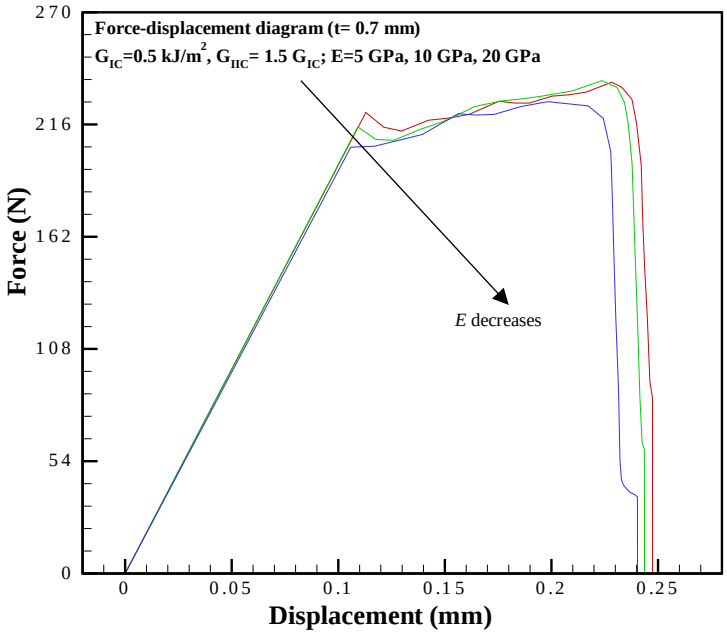

(c)

Figure 4.7. Predicted force-displacement diagrams at varying adhesive elastic modulus *E* (continued)

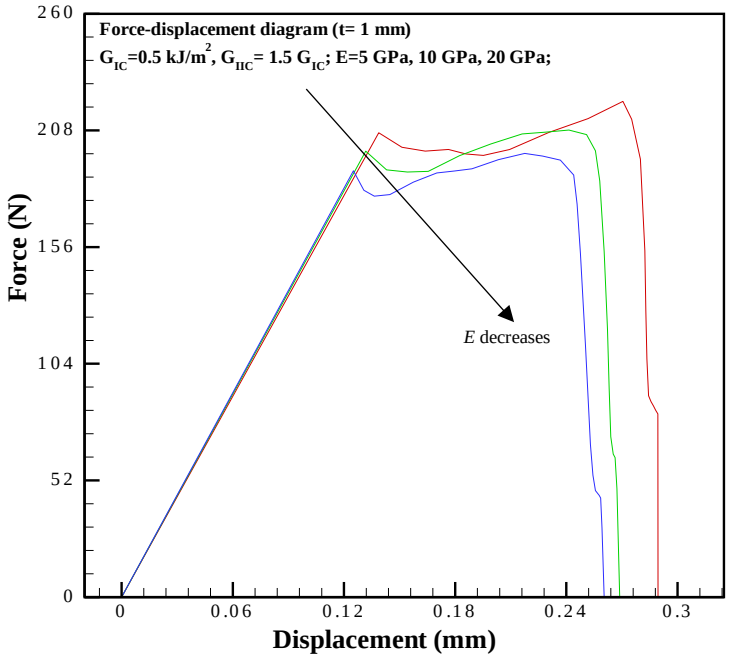

(d)

Figure 4.7. Predicted force-displacement diagrams at varying adhesive elastic modulus *E* (continued)

The present scaling analysis predicts that ABSSSJ with the highest adhesive elastic modulus correlates to the highest yield force though the variation of the yield force with the adhesive elastic modulus is not significant. Varying adhesive elastic moduli (*E*= 5 GPa, 10 GPa and 20 GPa) are implemented in the CZM-based FEA of the ABSSSJs with varying adhesive layer thickness (*t*= 0.2 mm, 0.5 mm, 0.7 mm and 1 mm, respectively). As shown in Fig. 4.7, the tensile force increases with increasing axial displacement in the elastic region till debonding initiates. Upon debonding, the tensile force drops with increasing axial displacement and then increases nonlinearly for the entire debonding process until the ultimate tensile force is reached, corresponding to the final failure of the joint. Besides, at the fixed adhesive layer thickness and axial displacement of the joint, the tensile force slightly decreases with increasing elastic modulus

of the adhesive layer; at the fixed adhesive elastic modulus and axial displacement of the joint, the tensile force decreases with increasing adhesive layer thickness. Although the tensile force varies with varying elastic modulus property and adhesive layer thickness, the dependencies of the force-displacement diagrams upon the elastic modulus and thickness of the adhesive layer is not significant compared to that of the interfacial debonding/fracture toughness.

4.2.2.3. Force-Displacement Relations at Varying Adhesive Thickness

Structural design of joints with high accuracy and efficiency requires an accurate understanding of the adhesive layer thickness. The current scaling analysis of the influence of adhesive thickness on the force-displacement behaviors can be an effective guideline for both computer-aided design (CAD) and practical implications.

Material thickness plays an important role in prediction of the failure process and lifetime of various bonded joints. Therefore, this study is further extended to examine the effects of adhesive layer thickness t on the force-displacement diagrams and the failure of ABJs by detailed computational analysis of the ABSSSJs in which a higher adhesive thickness corresponds to a lower tensile force to initiate debonding and therefore, a larger displacement is required to result in the complete debonding failure of bonded joint structures, i.e., a thicker adhesive layer corresponding to a tougher ABJ.

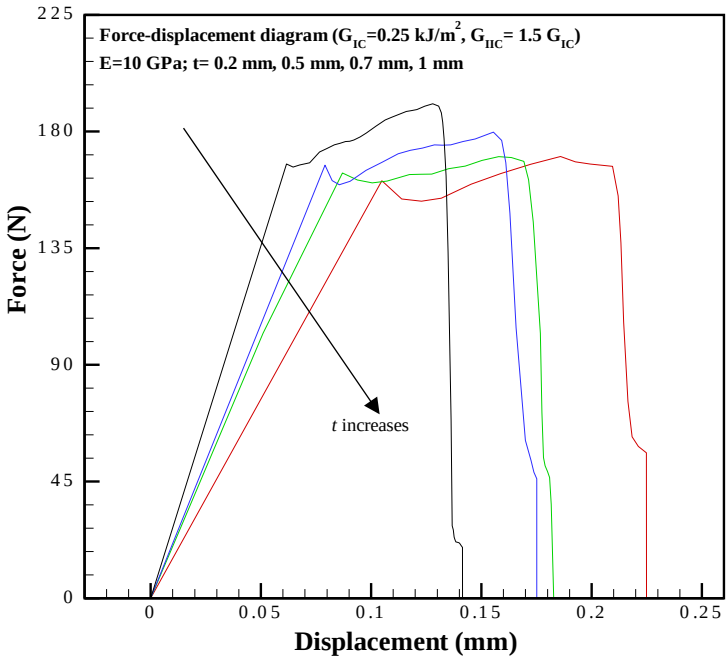

(a)

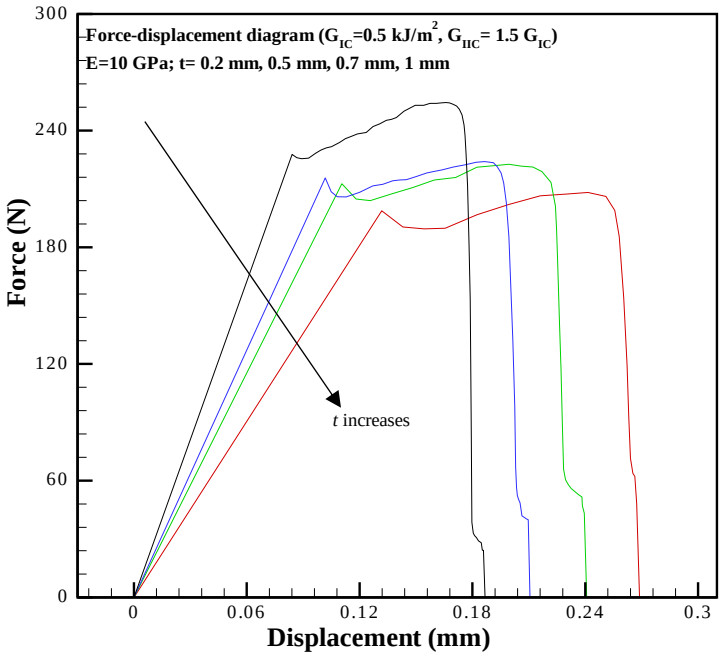

(b)

Figure 4.8. Predicted force-displacement diagrams at varying adhesive thickness *t*

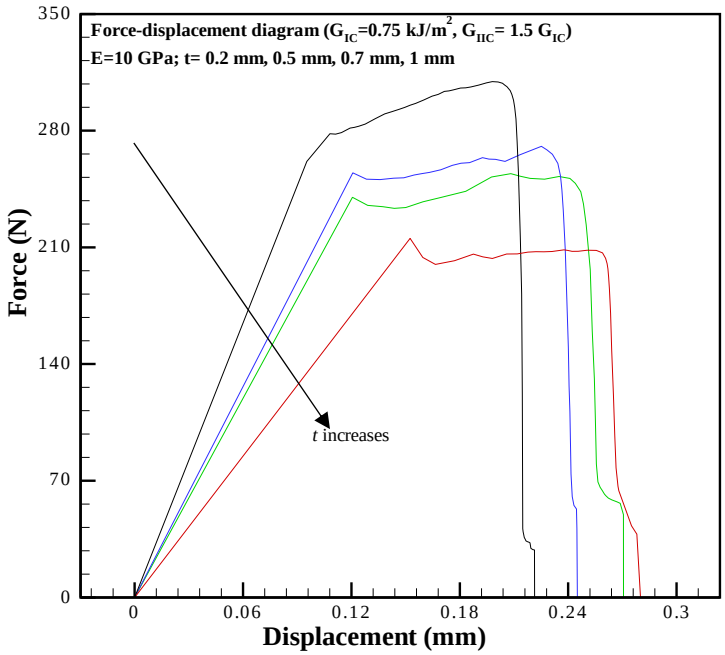

(c)

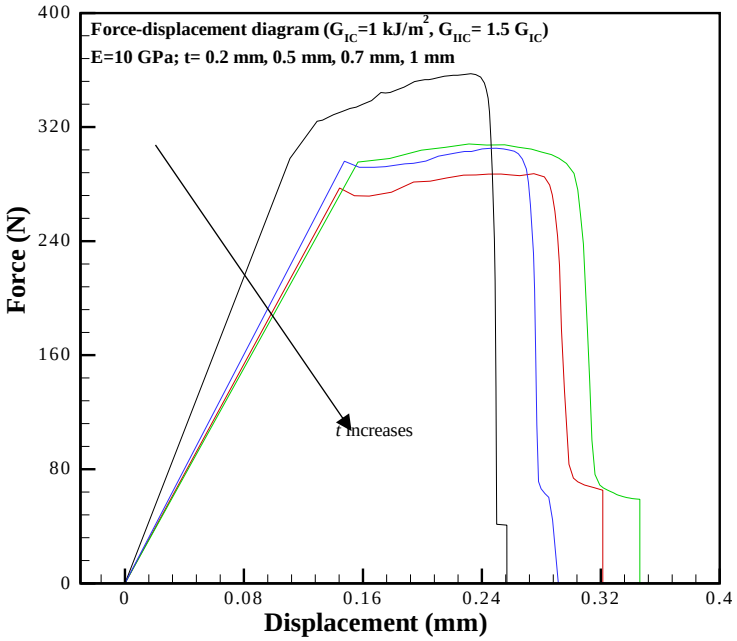

(d)

Figure 4.8. Predicted force-displacement diagrams at varying adhesive thickness *t* (continued)

Varying cohesive energies are considered such that ($G_{IC} = 0.25\frac{kJ}{m^2}, G_{IIC} = 1.5G_{IC}\frac{kJ}{m^2}$); ($G_{IC} = 0.5\frac{kJ}{m^2}, G_{IIC} = 1.5G_{IC}\frac{kJ}{m^2}$); ($G_{IC} = 0.75\frac{kJ}{m^2}, G_{IIC} = 1.5G_{IC}\frac{kJ}{m^2}$) and ($G_{IC} = 1.0\frac{kJ}{m^2}, G_{IIC} = 1.5G_{IC}\frac{kJ}{m^2}$); meanwhile the adhesive thickness varies such that *t*= 0.2 mm, *t*= 0.5 mm, *t*= 0.7 mm and *t*= 1 mm. The characteristic force-displacement diagrams during the entire debonding process of the joint are plotted at varying adhesive layer thickness and fixed adhesive elastic modulus and debonding toughness. The detailed scaling analysis here provides the clear evidence of the impact of the adhesive layer thickness on the full-range force-displacement diagram and the failure of bonded joints. The computational scaling analysis indicates that ABJs with the lower adhesive layer thickness provides better debonding strength and mechanical properties.

4.2.2.4. Dependencies of Debonding Toughness on Initial Failure and Ultimate Load

In this section, the dependencies of debonding toughness on the initial failure and ultimate load at varying adhesive thickness *t* are summarized based on the above scaling analysis. The elastic modulus *E* of the adhesive layer is kept constant whereas the values of the initial failure (yield force) and ultimate load (ultimate force) are taken from Fig. 4.8(a&b) and Fig. 4.8 (c&d), respectively. The adhesive layer thickness is taken as *t*= 0.2 mm, 0.5 mm and 0.7 mm.

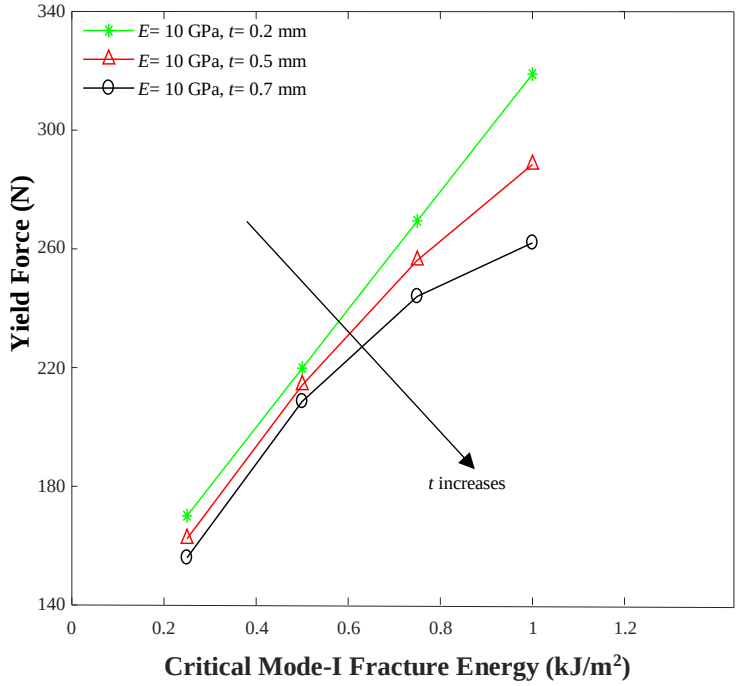

(a)

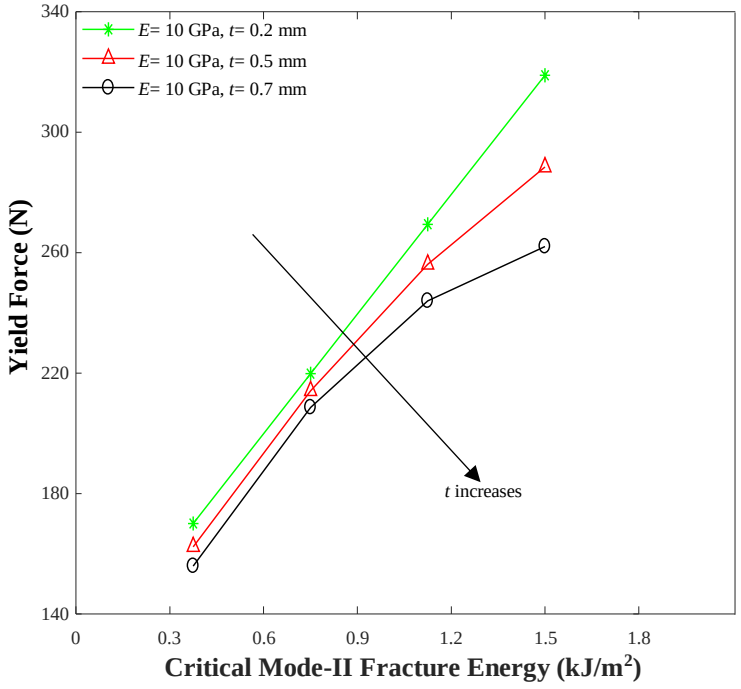

(b)

Figure 4.9. Variations of the tensile force to initiate debonding and ultimate tensile force with varying cohesive fracture energies

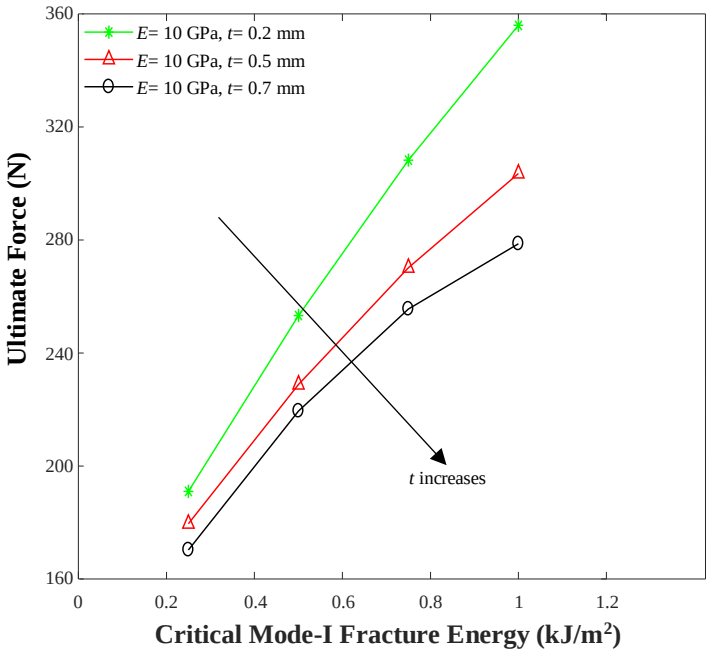

(c)

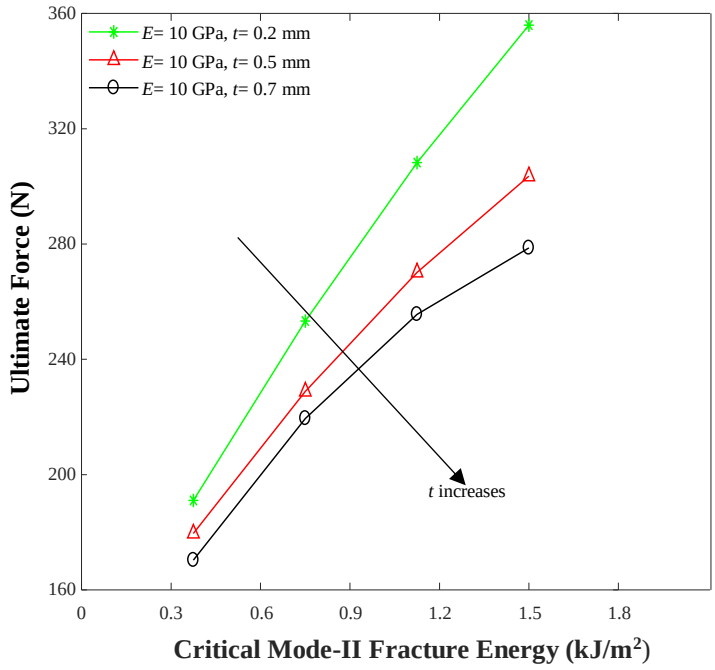

(d)

Figure 4.9. Variations of the tensile force to initiate debonding and ultimate tensile force with varying cohesive fracture energies (continued)

In the case of ABSSSJs, at fixed elastic modulus E and thickness t of the adhesive layer, the critical tensile force to initiate the debonding failure increases with increasing debonding toughness as shown in Figs. 4.9(a) & (b). In principle, at fixed elastic modulus E and thickness t of the adhesive layer, a higher tensile force is needed to generate a higher strain energy release rate corresponding to the higher debonding toughness for initiating the crack growth. Furthermore, at fixed elastic modulus E and debonding toughness G_C of the adhesive layer, the critical tensile force to initiate the debonding decreases with increasing adhesive thickness t. This observation is owing to the fact that under the action of the same tensile force, a relatively thicker adhesive layer can store/release the higher strain energy than the thinner ones, which implies that a lower critical tensile force is needed to generate the strain energy release rate for initiating the crack growth in the condition of the same level of debonding toughness of the joint. The similar scenarios can also be applied for reasoning the dependency of ultimate load upon the debonding toughness at varying adhesive layer thickness as shown in Figs. 4.9 (c) & (d).

4.3. Concluding Remarks

Cohesive zone model has been implemented effectively for detailed scaling analysis of the characteristic full-range force-displacement diagrams of ABSSSJs at varying thickness and material properties of the adhesive layer. By using CZM model, the present computational approach is able to clearly determine the influence of the material properties and design parameters, e.g., the cohesive fracture energy, adhesive elastic modulus, and adhesive layer thickness, on the critical tensile force and toughness of ABJs. It is found that both adhesive elastic modulus E and cohesive fracture energy G_c positively influence the toughness and load-carrying capacity of ABJs under consideration. Though the present computational study was conducted

based on simple ABSSSJs, the outcomes of this study can hold well for other ABJs. The present CZM-based FEA provides a rational computational approach for strength and toughness analysis of ABJs, which are critical to the design and failure analysis of various ABJs and bonded structures and exploration of the effects of material properties and geometries on the load-carrying capacity and toughness extension of broad bonded joints and ABJs.

5. CZM-BASED COMPUTATIONAL SIMULATIONS OF THE FULL-RANGE ELASTOPLASTIC BEHAVIOR OF PNCS

5.1. Introduction

In this chapter, cohesive zone model (CZM) is integrated into FEM to simulate the full-range elastoplastic failure process of PNCs and to examine the effects of the process parameters, e.g., the aspect ratio and clay particle volume fraction, on the mechanical behavior and elastoplastic failure process of PNCs. Bilinear CZM available in the commercially available FEM software package (ANSYS®) is employed in the simulations, where clay distribution pattern, particle aspect ratio and volume fraction are considered as the model parameters. During the numerical process, two clay particle distribution patterns, i.e., the stack and stagger distribution patterns, and several aspect ratios and volume fractions of the clay particles are utilized. In addition, the clay particles are treated as linearly elastic solid while the polymeric resin is treated as idealized elastoplastic solid.

5.2. Problem Formulation and Solutions

Nanoclays are generally stiff and carry high strength in contrast to polymeric resins. Therefore, clay nanoparticles remain in the elastic deformation region until the catastrophic failure of the polymeric matrix. In the present CZM-based FEA study, 2D plane-strain state is considered. All the clay nanoparticles are assumed to distribute in the polymeric matrix in either stack or stagger configuration. In addition, the effect of the roundness at the edges of the clay nanoparticles on the stress field is also examined.

In PNC processing, three clay particle configurations can exhibit in polymeric resins to form polymer clay composites, depending upon the varying extent of exfoliation of the clay

particles, i.e., conventional particles, intercalated nanoparticles and exfoliated nanoparticles, as shown in Fig. 5.2. For the purpose of examining the impact of the process parameters on the mechanical properties of the resulting PNCs, both stack and stagger configurations of the nanoparticle distribution are considered as shown in Figs. 5.3 and 5.4. In addition, process parameters including clay particle volume fraction of 2.5%, 5%, 7.5% and10% and aspect ratio of 5, 7.5, 10 and 20 are utilized in the computational simulations, and their effects on the full-range effective stress-strain diagrams of the resulting PNCs are examined. During the CZM-based FEM modeling, symmetrical boundary condition is generated to mimic the periodic boundaries; constant uniaxial tension strain is applied along with the clay particle direction onto the boundaries of the representative area element (RAE). 2D quadrilateral 4-node elements available in ANSYS® are used. Pure penalty formulation method has been adopted for this nonlinear analysis which is a must for dealing with the contact nonlinearity (Stefancu et al., 2011). In addition, the nonlinear convergence criterion, number of steps and substeps along with all the other nonlinear options are set as program by defaults. In a broader view, not only the process parameters govern the potential failure characteristics of PNCs, but also do the clay particle orientation and shear strength between the clay and polymeric resin. The computational scaling analyses of the effective stress-strain behavior of PNCs and the impact of process parameters on the effective mechanical properties of PNCs can elucidate the selection of nanoclay and polymeric resin for optimal mechanical properties of PNCs. In-depth CZM-based FEA of PNCs is performed for this purpose.

5.2.1. Material Models

In this computational study, clay particles are assumed as linearly elastic solid whereas the polymeric matrix is taken as idealized elastoplastic solid. Effects of clay particle volume fraction and aspect ratio are taken into account to explore the full-range elastoplastic failure process of

PNCs. Scaling analyses of the effect stress-strain behaviors of the resulting PNCs are conducted based on the uniaxial tensile deformation applied to the boundaries of the RAEs.

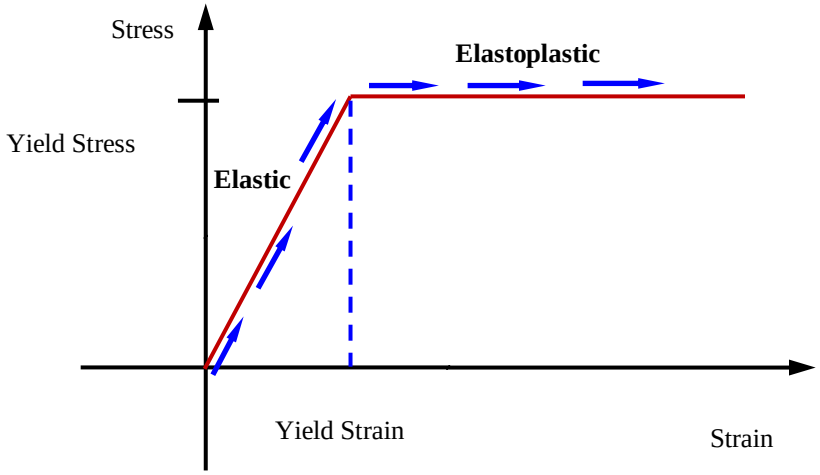

Figure 5.1. Schematic diagram of the stress-strain relation of idealized elastoplastic materials

The yield stress of the polymeric matrix is taken as 79 MPa while the Young's modulus and Poisson's ratio are assumed as 2.75 GPa and 0.41, respectively; the Young's modulus and Poisson's ratio of clay platelets are taken as 178 GPa and 0.28, respectively (Rahman and Wu, 2017).

5.2.2. Representative Area Element of Material Models

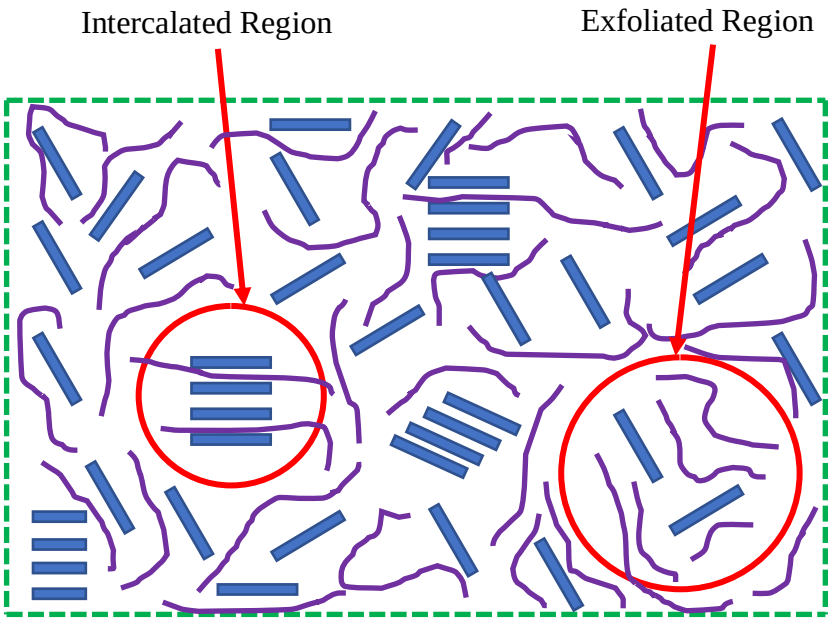

Figure 5.2. Schematic of clay particles dispersions in polymeric matrix

In this study, bilinear CZM is used for the PNCs, in which the representative area elements (RAEs) of both the stack and stagger configurations are utilized for exploring both the failure process and the full-range effective stress-strain behaviors of PNCs with varying clay particle aspect ratios and volume fractions. Mixed-mode debonding criterion is used for this CZM-based FEA of PNCs. Effect of the edge roundness of the clay particles on the stress field of PNCs is also investigated. The implementation of bilinear CZM-based FEA and the computational results of the scaling analysis of the full-range effective stress-strain behaviors at varying clay particle distribution pattern, aspect ratio and volume fraction are given in the following.

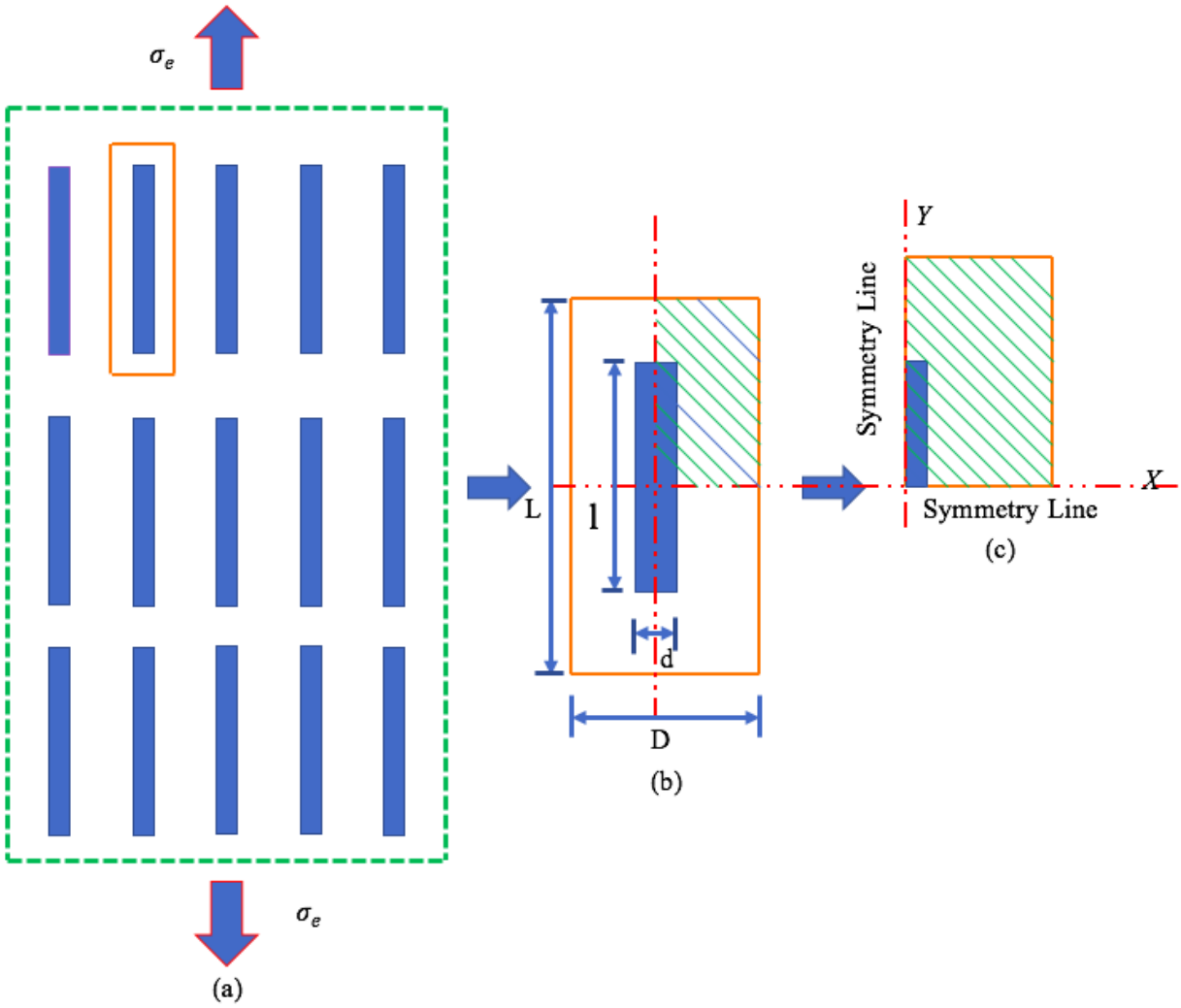

Figure 5.3. Schematic of a representative area element (RAE) of a stack configuration of PNCs for the present CZM-based FEA. (a) Stacked clay particles; (b) a RAE; and (c) a quarter symmetric RAE for FEA simulation

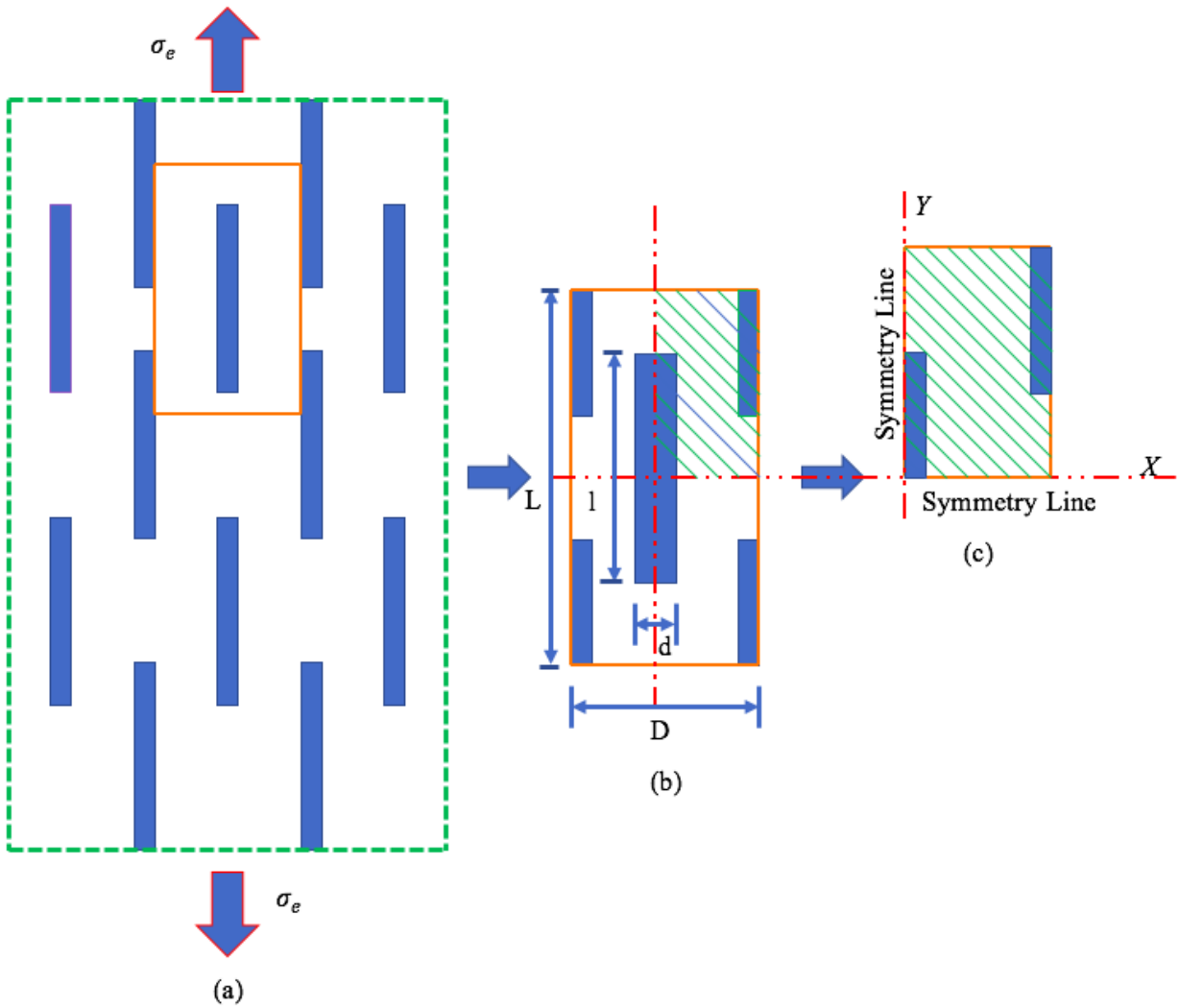

Figure 5.4. Schematic of a representative area element (RAE) of a stagger configuration of PNCs for the present CZM-based FEA. (a) Staggered clay particles; (b) a RAE; and (c) a quarter symmetric RAE for FEA simulation

5.2.3. CZM-based FEA for Computational Analysis of the Effective Mechanical Behaviors of PNCs

A computational micromechanics model is adopted in this study for the nonlinear failure analysis of the PNCs with a broad range of clay platelets volume fraction (V_f= 2.5%, 5%, 7.5% and 10%) and aspect ratio (ρ= 5, 7.5, 10 and 20) (Rahman and Wu, 2017). Two clay particle distributions, i.e., the stack and stagger distribution patterns are considered, and the effect of the edge roundness of the clay particles are also taken into account. The influence of CZM in the effective stress-strain relationship is examined and compared with those obtained via regular FEA without adoption of CZM. The effective elastic moduli extracted from the effective stress-strain diagram (Figs. 5.8 & 5.9) of both the stack and stagger models shows very good consistence and nearly the same values, especially in the cases of low volume fractions of clay particles. According to linear elastic micromechanics, the effective elastic modulus of PNCs is roughly independent of either the stack or stagger clay-particle distribution pattern though a small variation is identified due to varying plastic deformations and clay-particle interaction of the two models. As a result, the present numerical results are consistent with those based on classic linearly elastic micromechanics models. In addition, the present study also indicates that at the low volume fraction of clay particles in resins, the effective ultimate tensile strength of the PNCs does not show noticeable difference based on the computational micromechanics models with and without CZM.

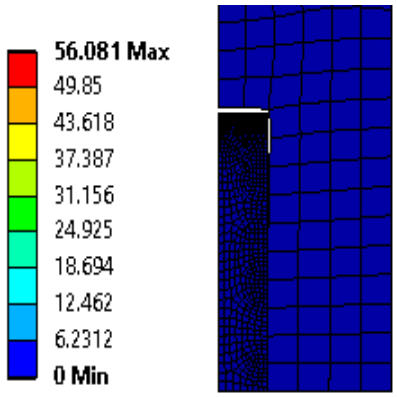

(a)

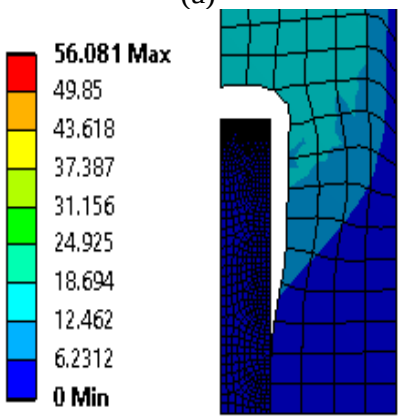

(b)

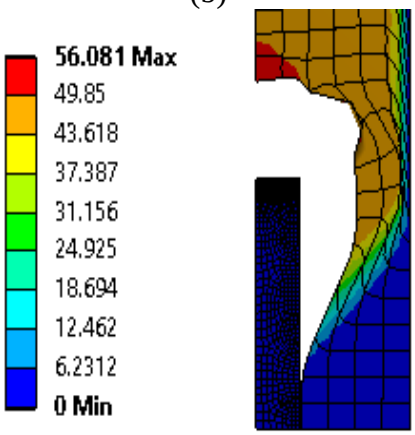

(c)

Figure 5.5. Deformation contour at the crack tip of a clay particle in polymeric matrix: (a) crack initiates, (b) crack propagates, and (c) crack growth reaches the final state

During this study, the values of the effective elastic modulus and corresponding ultimate tensile strengths are taken from the initial slope of the linearly elastic region of the effective stress-strain diagrams of all the computational cases. However, there is no significant variations noticed between the round and sharp edges of the clay platelets of PNCs in terms of both effective modulus and ultimate tensile strength. Such observations at varying clay particle geometric configurations can be validated by the FEA simulations (Figs. 5.5 & 5.18) and their results (Figs. 5.8 & 5.13; Figs. 5.19 & 5.20). Besides, a comparative study between CZM-based FEA and FEA without CZM is conducted at varying process parameters, i.e., the clay particle volume fraction and aspect ratio (Figs. 5.6 and 5.7). It shows that FEA of PNCs without CZM exhibits a slightly higher load-carrying capacity than that predicted by CZM-based FEA at fixed clay particle aspect ratio and volume fraction. In addition, Figs. 5.9 and 5.14 show that no significant differences between the effective stress-strain diagrams of PNCs predicted by CZM-based FEA and regular FEA without CZM based on the stagger model. Therefore, the rest analyses are based only on the stack model of PNCs.

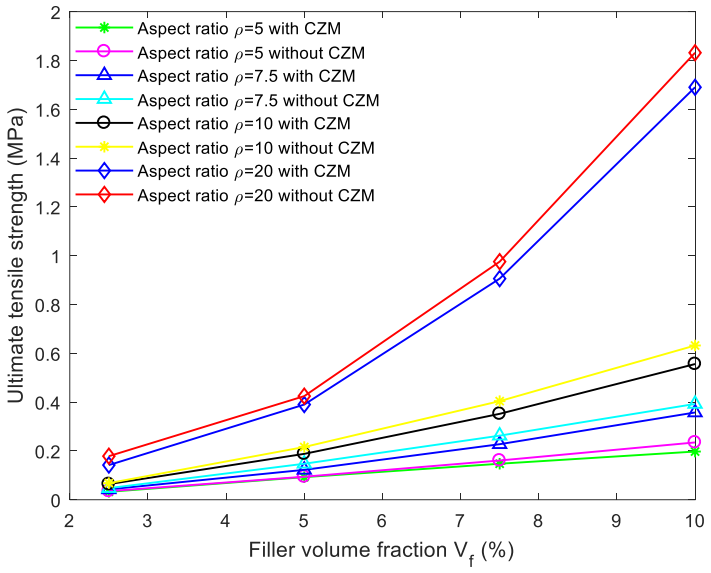

Figure 5.6. Variations of the ultimate tensile stress σ_{ult} with respect to the particle volume fraction V_f at varying clay particle aspect ratios, ρ= 5, 7.5, 10 and 20

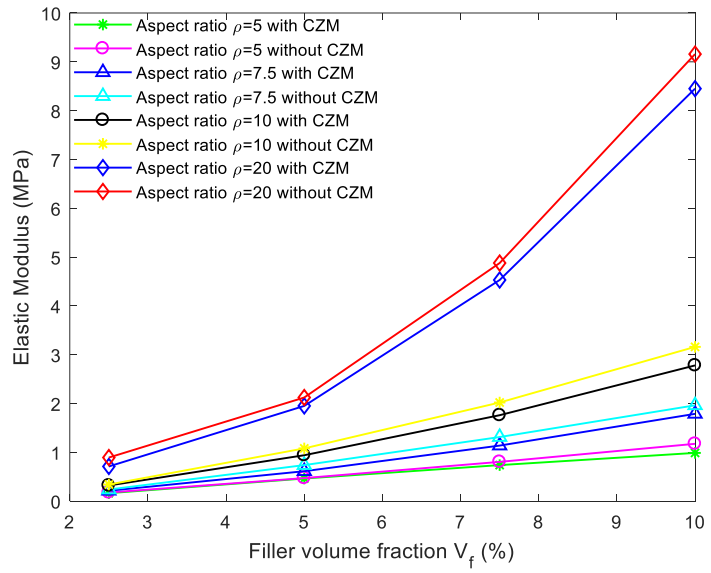

Figure 5.7. Variations of the elastic modulus E_e with respect to the particle volume fraction V_f at varying clay particle aspect ratios ρ= 5, 7.5, 10 and 20

The CZM-based FEA predicts both the effective elastic modulus and ultimate tensile strength slightly lower than those based on regular FEA without CZM at varying clay particle volume fraction and aspect ratio as shown in Figs. 5.6 and 5.7. Therefore, CZM-based FEM model works better for PNCs, in which the clay platelets are in the nanometer range and their volume fraction is relatively smaller. The effective elastic modulus of the PNCs is extracted from the initial slope of the linearly elastic region of the effective stress-strain diagrams. The numerical results indicate a very good consistence with the linearly elastic stress-strain relation as expected.

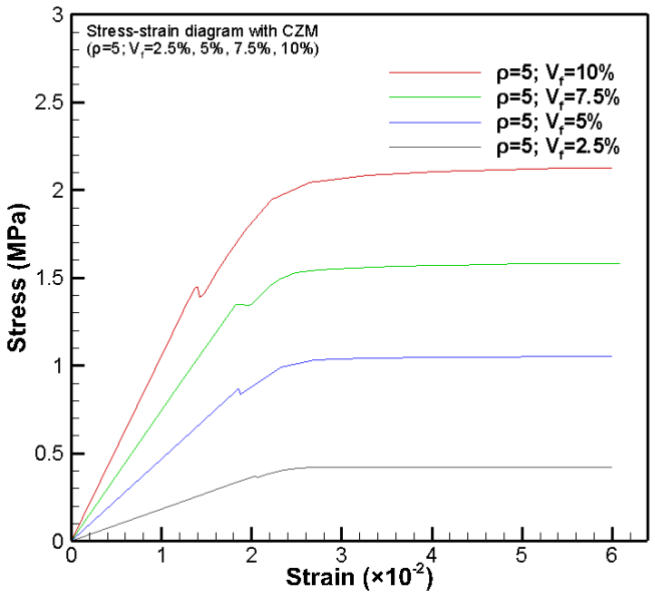

Figure 5.8. Effective stress-strain diagrams of the PNCs (stack model) predicted by CZM-based FEA at varying particle volume fractions V_f= 2.5%, 5%, 7.5% and 10% and the clay particle aspect ratio ρ= 5

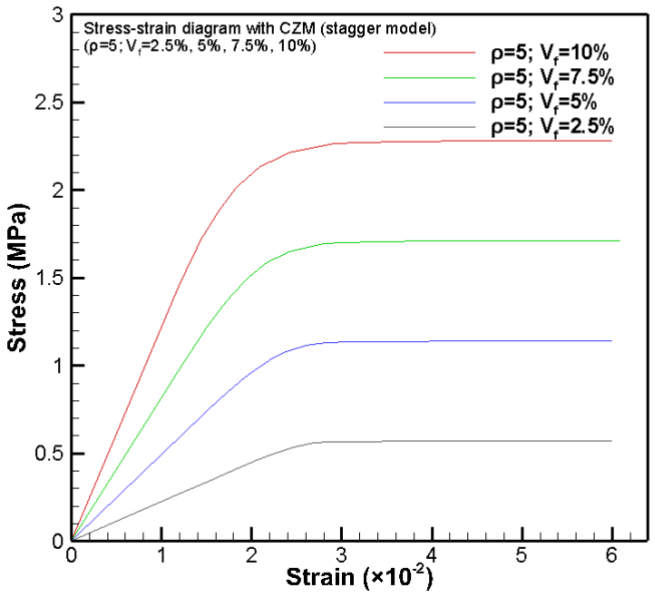

Figure 5.9. Effective stress-strain diagrams of the PNCs (stagger model) predicted by CZM-based FEA at varying particle volume fractions V_f= 2.5%, 5%, 7.5% and 10% and the clay particle aspect ratio ρ= 5

Each effective stress-strain diagram consists of three regions, i.e., (1) the beginning linearly elastic region, (2) the second crack initiation region, and (3) the final region of complete clay particle debonding. Similar to the mechanical behavior of the idealized elastoplastic resins, the effective tensile stress increases linearly with increasing effective tensile strain till to the yield strain of the polymeric matrix, after which the effective tensile stress becomes nearly constant as shown in Figs. 5.8-5.12 and 5.19.

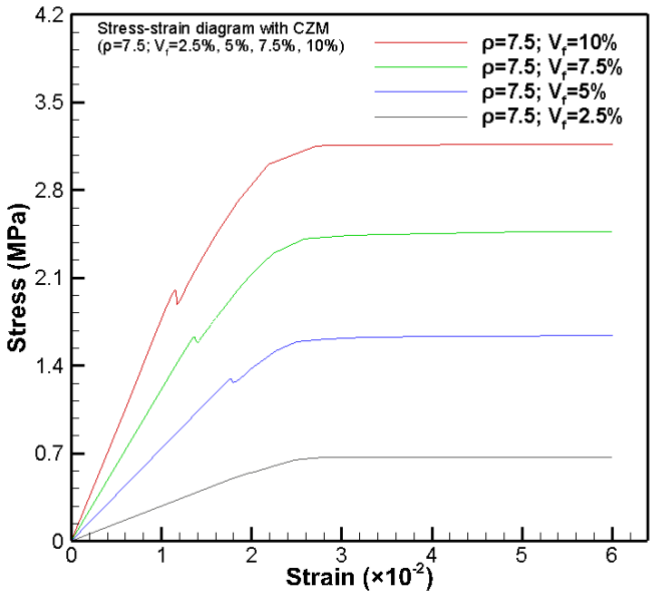

Figure 5.10. Effective stress-strain diagrams of the PNCs (stack model) predicted by CZM-based FEA at varying particle volume fractions V_f= 2.5%, 5%, 7.5% and 10% and the clay particle aspect ratio ρ= 7.5

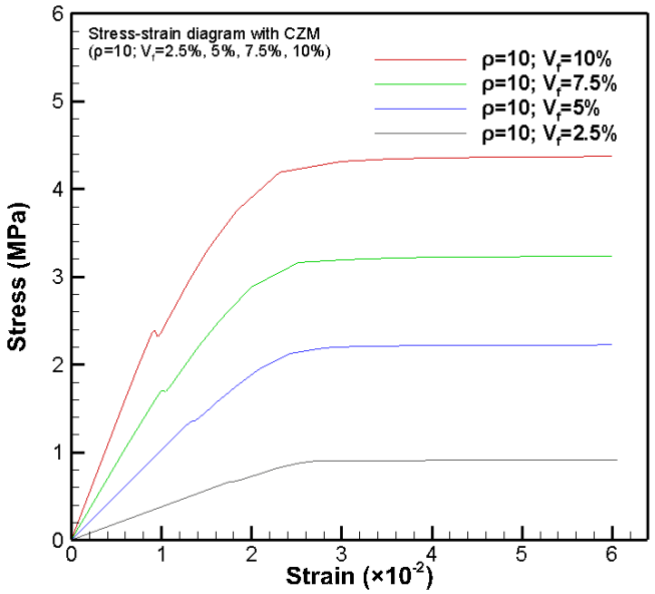

Figure 5.11. Effective stress-strain diagrams of the PNCs (stack model) predicted by CZM-based FEA at varying particle volume fractions V_f= 2.5%, 5%, 7.5% and 10% and the clay particle aspect ratio ρ= 10

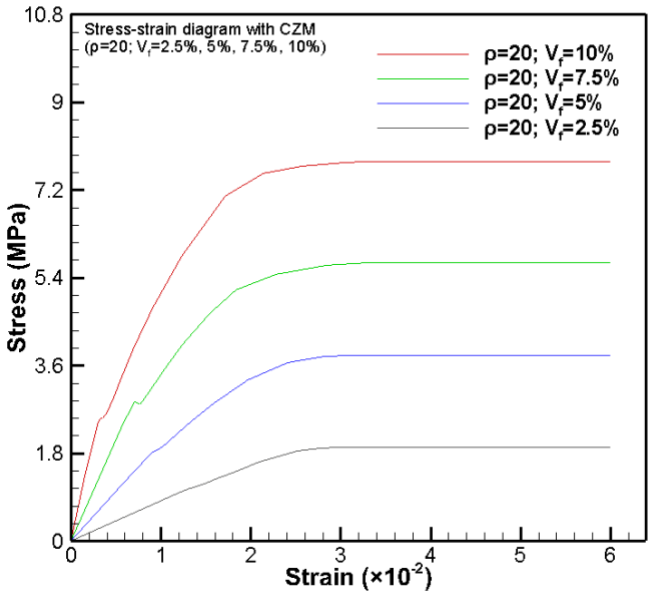

Figure 5.12. Effective stress-strain diagrams of the PNCs (stack model) predicted by CZM-based FEA at varying particle volume fractions V_f= 2.5%, 5%, 7.5% and 10% and the clay particle aspect ratio ρ= 20

Figs. 5.8-5.12 and 5.19 indicated that PNCs behave as linearly elastic solids when the effective tensile strain is nearly below the yield strain of the resin. A softening behavior is noticed due to the plastic deformation near the sharp edge of the clay platelets where stress concentration exists. The present numerical studies are based on a simple micromechanics model, and the complicated physical and chemical properties relating the interfaces between clay particles and polymeric resins are simplified. Such complicated interfacial phenomena in PNCs are beyond the research scope of the present investigation.

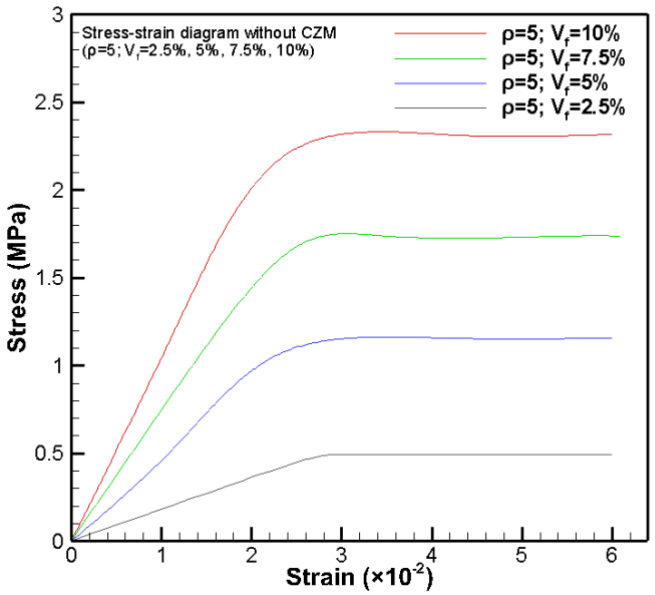

Figure 5.13. Effective stress-strain diagrams of the PNCs (stack model) predicted by FEA without CZM at varying particle volume fractions V_f= 2.5%, 5%, 7.5% and 10% and the clay particle aspect ratio ρ= 5

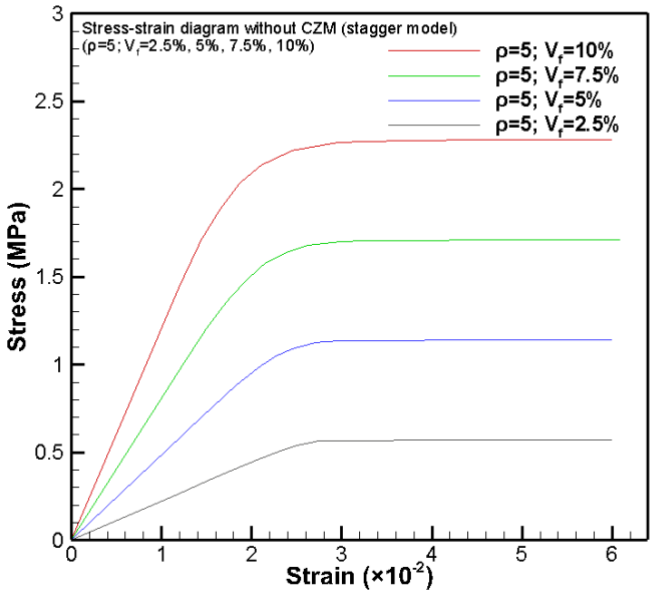

Figure 5.14. Effective stress-strain diagrams of the PNCs (stagger model) predicted by FEA without CZM at varying particle volume fractions V_f= 2.5%, 5%, 7.5% and 10% and the clay particle aspect ratio ρ= 5

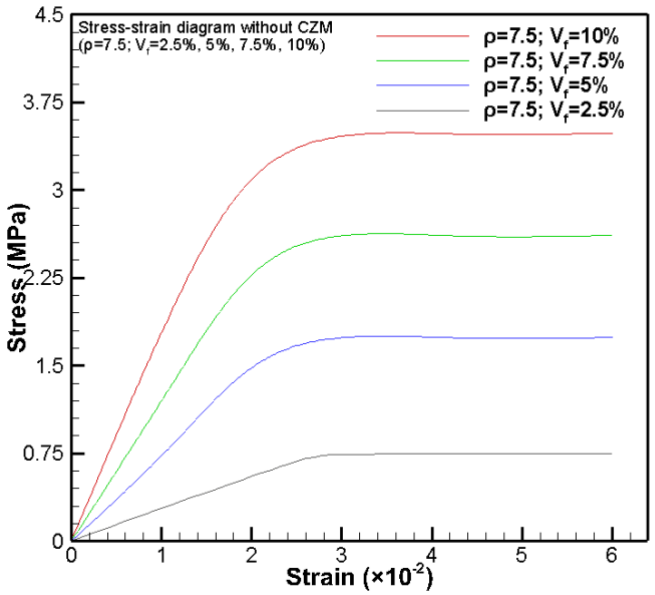

Figure 5.15. Effective stress-strain diagrams of the PNCs (stack model) predicted by FEA without CZM at varying particle volume fractions V_f= 2.5%, 5%, 7.5% and 10% and the clay particle aspect ratio ρ= 7.5

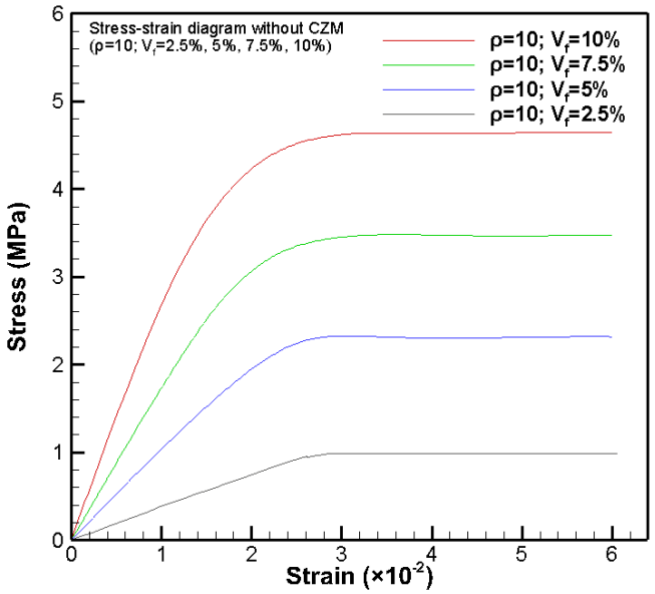

Figure 5.16. Effective stress-strain diagrams of the PNCs (stack model) predicted by FEA without CZM at varying particle volume fractions V_f= 2.5%, 5%, 7.5% and 10% and the clay particle aspect ratio ρ= 10

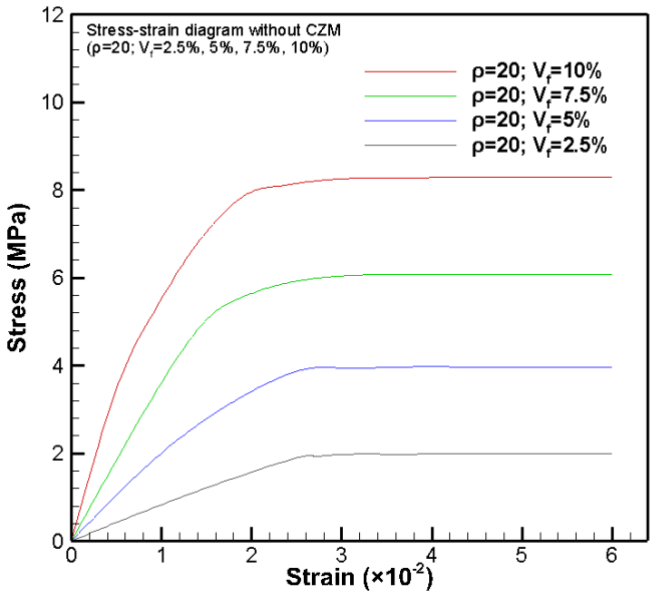

Figure 5.17. Effective stress-strain diagrams of the PNCs (stack model) predicted by FEA without CZM at varying particle volume fractions V_f= 2.5%, 5%, 7.5% and 10% and the clay particle aspect ratio ρ= 20

From the above computational results, it can be concluded that at low volume fractions or low aspect ratios, no significant improvement of the ultimate tensile strength is detected as shown in Fig. 5.7 based on both the stack and stagger clay-particle distribution patterns. In the above computational cases, the yield strength of polymeric matrices dominates the ultimate tensile strength of the PNCs and its effect on the load-carrying capacity is negligible. Such observation can be interpolated such that the dilute clay particles dispersed in polymeric matrices are unable to form load transferring bridges and therefore have no noticeable influence on strengthening the resulting PNCs. However, with increasing either the clay particle volume fraction or the aspect ratio, the effective tensile strength starts to increase nonlinearly and a significant variation in the ultimate tensile strength corresponding to the resin yield strain is noticed. For example, at aspect ratio ρ= 7.5 and volume fractions V_f = 7.5%, the ultimate tensile strength of PNC is improved 97%.

Moreover, at aspect ratio ρ= 10 and volume fraction of V_f= 10%, a more significant improvement of the ultimate tensile strength of PNC is detected. These values are higher than those reported in the literature. The clay-particle orientation, polymer-clay interface, and clay particle waviness may work behind the reduction of these predicted values.

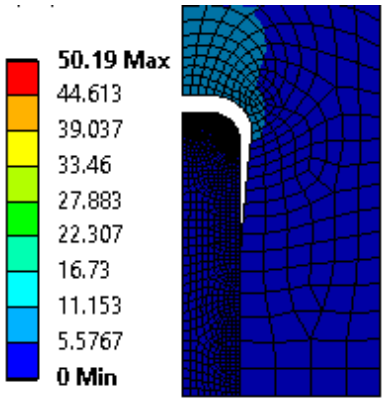

(a)

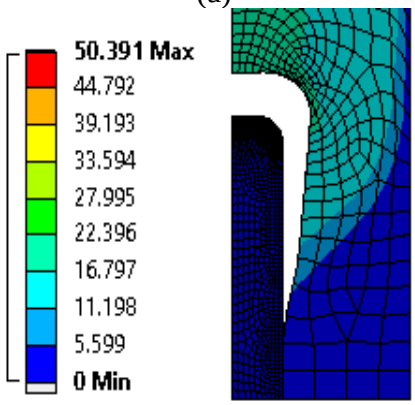

(b)

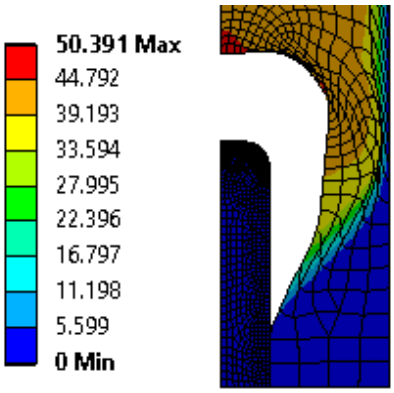

(c)

Figure 5.18. Deformation contour at the crack tip of a clay particle (round clay-particle edge) in polymeric matrix: (a) Crack initiates, (b) crack propagates, and (c) crack growth reaches the final state

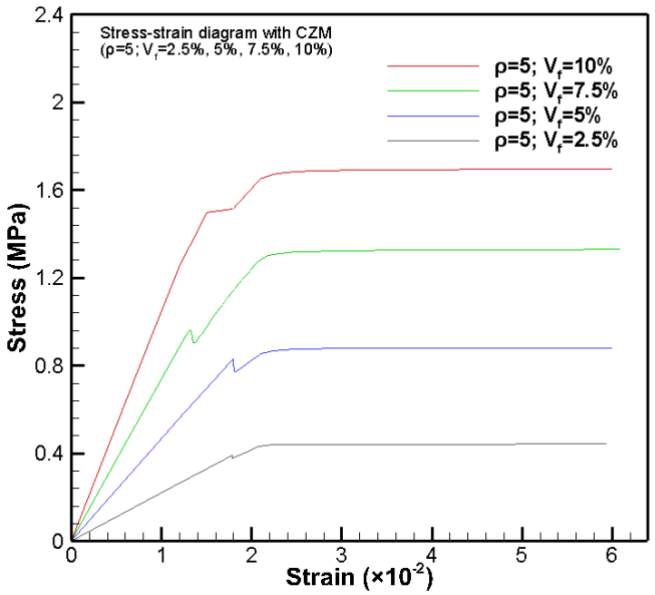

Figure 5.19. Effective stress-strain diagrams of the PNCs (round clay-particle edge) predicted by CZM-based FEA at varying particle volume fractions V_f= 2.5%, 5%, 7.5% and 10% and the clay particle aspect ratio ρ= 5

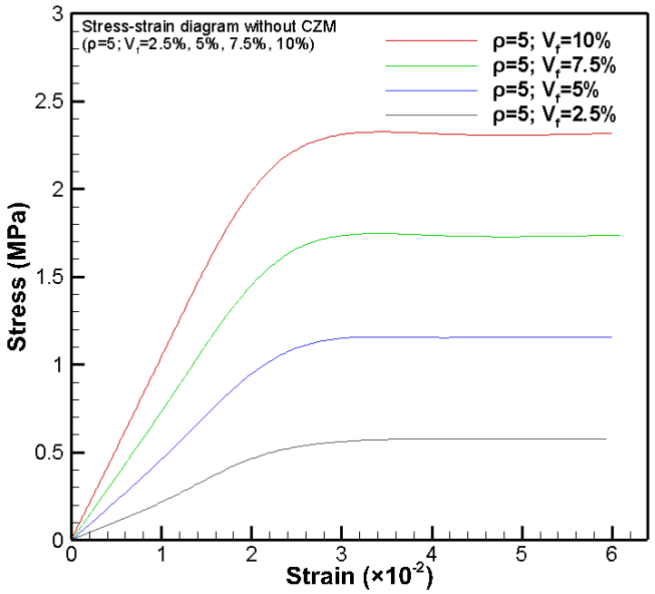

Figure 5.20. Effective stress-strain diagrams of the PNCs (curve in the sharp edge of the clay geometry) predicted by FEA without CZM at varying particle volume fractions V_f= 2.5%, 5%, 7.5% and 10% and the clay particle aspect ratio ρ= 5

However, in addition to the simple micromechanics stack model with sharp-edged clay particles, round-edged clay particles in the polymeric resin are also examined as shown in Fig. 5.18. The purpose to use round-edged instead of sharp-edged clay particles is to remove the potential unrealistic stress singularity at the shape corner. Improvement in the effective tensile stress of the PNCs is noticed with increasing both the clay particle volume fraction and aspect ratio. The effective tensile strength of PNCs predicted by CZM-based FEA shows slightly higher than that predicted by FEA without CZM as illustrated in Figs. 5.19 and 5.20. As a matter of fact, no substantial variation is founded in the effective stress-strain diagrams between the computational RAEs with sharp-edged and round-edged clay platelets as shown in Figs. 5.8 and 5.19, though the latter provides a more reasonable physical understanding. As no significant variation is noticed above, a simple micromechanics model based on the RAE of sharp-edged clay-platelets is employed for the entire computational simulations either in the stack or stagger clay-particle distribution pattern.

Consequently, the present computational study uses relatively low aspect ratios compared to those observed in realistic PNCs. However, the conclusions drawn from the present computational studies will be very useful to understand the nonlinear elastoplastic failure behavior of PNCs with varying process parameters. For example, when the particle aspect ratio is very high, a significant impact of the CZM on the load carrying-capacity of PNCs is observed. To date, substantial efforts to enhance the processing techniques are still desired for controlling the clay particle orientation and aspect ratio in polymeric matrices. In addition, the present numerical study is conducted based on a simple micromechanics model for varying geometric configurations. The numerical results provide the detailed insight to predict the mechanical and physical properties of the resulting PNCs. Such computational study can be further extended to explore the mechanisms

of failure in metal peeling, bone cracking and to observe the potential impact of the failure parameters in fiber-reinforced composites for predicting their accurate mechanical behaviors.

5.3. Concluding Remarks

CZM-based FEM is implemented efficiently for predicting the full-range failure process along with in-depth understanding of the effective stress-strain behaviors of PNCs and their dependency upon the PNC processing parameters. The present computational process can be conveniently utilized for examining the influence of the process parameters (e.g., aspect ratio and particle volume fraction) on the mechanical properties and failure mechanisms of PNCs. The present numerical results clarify the stiffening and toughening effects of both the aspect ratio and clay particle volume fraction. Noticeable variations are noticed in the resulting stress-strain behaviors predicted by both CZM-based FEA and regular FEA without CZM for the RAEs with stack clay-particle distribution pattern. Slightly higher effective stresses and ultimate tensile strengths of PNCs are predicted by CZM-based FEA at higher clay particle volume fractions (V_f = 10, in the present case) at fixed clay aspect ratio. On the other hand, when the clay-particle volume fraction becomes lower; the effective stress and ultimate tensile strength predicted by FEA with and without CZM show no obvious difference at a fixed clay-particle aspect ratio. The present CZM-based FEA study of PCNs can be further extended to complex nanocomposites with additional material and process parameters, which provides an effective computational tool for the efficient computer-aided nanocomposite design for the purpose of achieving targeted mechanical and physical properties as well as desired PNC processing.

6. CONCLUSIONS

Adhesively bonded joints (ABJs) and polymer nanoclay composites (PNCs) have been successfully integrated into broad applications in aerospace, aeronautical and ground vehicles. Efficient and reliable analysis of the fracture toughness and failure mechanisms of ABJs and PNCs plays a crucial role in optimal structural design, low-cost manufacturing and reliable prediction of their mechanical performance including the mechanical strength, fracture toughness, and fatigue durability, among others. The research of this thesis has successfully addressed the fracture toughness, failure mechanisms and entire failure process of ABJs made of thin ductile metal adherends (i.e., aluminum alloys and mild steels) and PNCs via formulating a reliable fracture model and computational micromechanics cohesive-zone model (CZM) based finite element method (FEM). The summary of this research along with their theoretical and computational results can be summarized as follows.

- Theoretical formulation and validation of a new nonlinear fracture model have been performed for effective, accurate extraction of the fracture/debonding toughness of thin-layered metal ABJs with large plastic deformations and elastic springback. New explicit expression of fracture toughness (Γ) is obtained, which successfully takes into account the significant springback of power-law strain-hardening elastoplastic metals (e.g., aluminum alloys, mild steels etc.) after large plastic deformations. The validation of the new nonlinear fracture model is implemented by using the experimental ABJ fracture data available in the literature.
- Detailed scaling analysis based on the new fracture model of ABJs is performed to explore the dependencies of the ABJ debonding toughness upon their material properties and

geometries. Such in-depth analysis is useful to explore the effects of varying structural and material parameters on the failure behavior of ABJs made of thin ductile metal adherends for better ABJ design, manufacturing, and failure prediction.

- Successful integration of CZM into FEM is also presented to simulate the debonding process in ABJs, which lays the basis for elucidating the failure mechanisms and the full-range nonlinear mechanical behavior of ABJs during the entire debonding process under external loads.
- Besides, CZM-based FEM is further extended for exploring the full-range elastoplastic behavior of PNCs with clay-particle debonding and parameter dependencies. Till now, no similar work is reported in the literature on the failure process of PNCs where debonding between clay particles and polymer resin is considered.

Therefore, the present theoretical and computational studies provide valuable understandings of the fracture toughness of ABJs with large plastic deformations and springback, the failure mechanisms and full-range debonding process of both ABJs and PNCs. The results of these studies are particularly useful for the predictions of more realistic fracture toughness, the full-range characteristic load-displacement behavior for better ABJ design, optimization, manufacturing and failure analysis, as well as the full-range elastoplastic behaviors of PNCs associated with the failure process and effective stress-strain relations for controlled processing and characterization of PNCs. The outcome of this research opens up new research directions and strategies for better structural design and optimization of ABJ and PNC, which may include

- Extension of the present theoretical fracture model for exploring the material removal mechanisms of metal machining.

- Investigation of the dynamic, thermal, and viscoelastic effects of adhesive layers on data reduction of the debonding toughness of thin-layered metal ABJs.
- Development of user-defined cohesive zone model (CZM, e.g., the trapezoidal cohesive law in ANSYS ® and similar) in commercial FEA software packages for enhanced computational accuracy.
- Application of CZM-based FEM models to explore the failure mechanisms in fiber-reinforced composites, coatings/metal peeling, bone cracking, etc.
- Validation of CZM-based FEM results based on novel instrumented experiments, and so on.

REFERENCES

Alexandre, M. and Dubois, P., 2000. Polymer-Layered Silicate Nanocomposites: Preparation, Properties and Uses of a New Class of Materials. Materials Science and Engineering: R: Reports, 28(1-2), Pp.1-63.

Alfano, M., Furgiuele, F., Leonardi, A., Maletta, C. and Paulino, G.H., 2007. Cohesive Zone Modeling of Mode I Fracture in Adhesive Bonded Joints. In Key Engineering Materials (Vol. 348, Pp. 13-16). Trans Tech Publications.

Almansoori, A., Majewski, C. and Rodenburg, C., 2017. Nanoclay/Polymer Composite Powders for Use in Laser Sintering Applications: Effects of Nanoclay Plasma Treatment. JOM, 69(11), Pp.2278-2285.

Barenblatt, G.I., 1962. The mathematical theory of equilibrium cracks in brittle fracture. In Advances in applied mechanics, 7, Pp. 55-129).

Blackman, B.R.K., Hadavinia, H., Kinloch, A.J. and Williams, J.G., 2003. The Use of a Cohesive Zone Model to Study the Fracture of Fibre Composites and Adhesively-Bonded Joints. International Journal of Fracture, 119(1).Pp.25-46.

Camacho, G.T. and Ortiz, M., 1996. Computational Modelling of Impact Damage in Brittle Materials. International Journal of Solids and Structures, 33(20-22), Pp.2899-2938.

Camanho, P.P., Davila, C.G. and De Moura, M.F., 2003. Numerical Simulation of Mixed-Mode Progressive Delamination in Composite Materials. Journal of Composite Materials, 37(16), Pp.1415-1438.

Campilho, R.D.S.G., De Moura, M.F.S.F., Pinto, A.M.G., Morais, J.J.L. and Domingues, J.J.M.S., 2009. Modelling the Tensile Fracture Behaviour of CFRP Scraf Repairs. Composites Part B: Engineering, 40(2), Pp.149-157.

Campilho, R.D.S.G., De Moura, M.F.S.F., Ramantani, D.A.., Morais, J.J.L. and Domingues, J.J.M.S., 2009. Buckling Behaviour of Carbon-Epoxy Adhesively-Bonded Scarf Repairs. Journal of Adhesion Science and Technology, 23(10-11), Pp.1493-1513.

Carlsson, L.A., Adams, D.F. and Pipes, R.B., 2002. Experimental Characterization of Advanced Composite Materials. CRC Press.

Cavalli, M.N. and Thouless, M.D., 2001. The Effects of Damage Nucleation on the Toughness of an Adhesive Joint. The Journal of Adhesion, 76(1), Pp.75-92.

Chan, M.L., Lau, K.T., Wong, T.T., Ho, M.P. and Hui, D., 2011. Mechanism of Reinforcement in a Nanoclay/Polymer Composite. Composites Part B: Engineering, 42(6), Pp.1708-1712.

Chen, Y., Chen, H. and Shi, J., 2013. In Vivo Bio-safety Evaluations and Diagnostic/Therapeutic Applications of Chemically Designed Mesoporous Silica Nanoparticles. Advanced Materials, 25(23), Pp.3144-3176.

Da Silva, L.F. and Campilho, R.D., 2012. Advances in Numerical Modelling of Adhesive Joints. Springer, Berlin, Heidelberg, Pp.1-93.

Da Silva, L.F., Das Neves, P.J., Adams, R.D. and Spelt, J.K., 2009. Analytical Models of Adhesively Bonded Joints—Part I: Literature Survey. International Journal of Adhesion and Adhesives, 29(3), Pp.319-330.

Da Silva, L.F., Das Neves, P.J., Adams, R.D., Wang, A. and Spelt, J.K., 2009. Analytical Models of Adhesively Bonded Joints—Part II: Comparative Study. International Journal of Adhesion and Adhesives, 29(3), Pp.331-341.

Davidson, B.D., Hu, H. and Schapery, R.A., 1995. An Analytical Crack-Tip Element for Layered Elastic Structures. Journal of Applied Mechanics, 62(2), Pp.294-305.

Davis, M. and Bond, D., 1999. Principles and Practices of Adhesive Bonded Structural Joints and Repairs. International Journal of Adhesion and Adhesives, 19(2-3), Pp.91-105.

Dong, Y. and Bhattacharyya, D., 2010. A Simple Micromechanical Approach to Predict Mechanical Behaviour of Polypropylene/Organoclay Nanocomposites Based on Representative Volume Element (RVE). Computational Materials Science, 49(1), Pp.1-8.

Dugdale, D.S., 1960. Yielding of steel sheets containing slits. Journal of the Mechanics and Physics of Solids, 8(2), Pp.100-104.

Elices, M.G.G.V., Guinea, G.V., Gomez, J. and Planas, J., 2002. The Cohesive Zone Model: Advantages, Limitations and Challenges. Engineering Fracture Mechanics, 69(2), Pp.137-163.

Grant, L.D.R., Adams, R.D. and Da Silva, L.F., 2009. Effect of the Temperature on the Strength of Adhesively Bonded Single Lap and T Joints for the Automotive Industry. International Journal of Adhesion and Adhesives, 29(5), Pp.535-542.

Guo, F., Aryana, S., Han, Y. and Jiao, Y., 2018. A Review of the Synthesis and Applications of Polymer–Nanoclay Composites. Applied Sciences, 8(9), p.1696.

Gustafson, P.A. and Waas, A.M., 2009. The Influence of Adhesive Constitutive Parameters in Cohesive Zone Finite Element Models of Adhesively Bonded Joints. International Journal of Solids and Structures, 46(10), Pp.2201-2215.

Hafiz, T.A., Wahab, M.A., Crocombe, A.D. and Smith, P.A., 2010. Mixed-Mode Fracture of Adhesively Bonded Metallic Joints under Quasi-Static Loading. Engineering Fracture Mechanics, 77(17), Pp.3434-3445.

Harper, P.W. and Hallet, S.R., 2008. Cohesive Zone Length in Numerical Simulations of Composite Delamination. Engineering Fracture Mechanics, 75(16), Pp.4774-4792.

Heslehurst, R. and Hart-Smith, L.J., 2002. The Science and Art of Structural Adhesive Bonding. Sample Journal, 38(2), Pp.60-71.

Higgins, A., 2000. Adhesive Bonding of Aircraft Structures. International Journal of Adhesion and Adhesives, 20(5), Pp.367-376.

Hu, H., Onyebueke, L. and Abatan, A., 2010. Characterizing and Modeling Mechanical Properties of Nanocomposites-Review and Evaluation. Journal of Minerals and Materials Characterization and Engineering, 9(04), p.275.

Hutchinson, J.W. and Suo, Z., 1991. Mixed Mode Cracking in Layered Materials. In Advances in Applied Mechanics (Vol. 29, Pp. 63-191). Elsevier.

Jin, Z.H., Paulino, G.H. and Dodds Jr, R.H., 2003. Cohesive Fracture Modeling of Elastic–Plastic Crack Growth in Functionally Graded Materials. Engineering Fracture Mechanics, 70(14), Pp.1885-1912.

Johnson, W.S., 1988. Adhesively Bonded Joints: Testing, Analysis, and Design (Vol. 981). ASTM International.

Khoramishad, H., Crocombe, A.D., Katnam, K.B. and Ashcroft, I.A., 2010. Predicting Fatigue Damage in Adhesively Bonded Joints using A Cohesive Zone Model. International Journal of Fatigue, 32(7), Pp.1146-1158.

Kim, K.S. and Aravas, N., 1988. Elastoplastic analysis of the peel test. International Journal of Solids and Structures, 24(4), Pp.417-435.

Kim, K.S. and Kim, J., 1988. Elasto-Plastic Analysis of the Peel Test for Thin Film Adhesion. Journal of Engineering Materials and Technology, 110(3), Pp.266-273.

Kinloch, A.J. and Williams, J.G., 1998. Comments on 'Determining the Toughness of Plastically Deforming Joints'. Journal of Materials Science Letters, 17(10), Pp.813-814.

Kinloch, A.J. and Williams, J.G., 1999. Further Comments on 'Determining the Toughness of Plastically Deforming Joints'. Journal of Materials Science Letters, 18(24), Pp.2049-2049.

Kojima, Y., Usuki, A., Kawasumi, M., Okada, A., Kurauchi, T. and Kamigaito, O., 1993. Synthesis of Nylon 6–Clay Hybrid by Montmorillonite Intercalated with E-caprolactam. Journal of Polymer Science Part A: Polymer Chemistry, 31(4), Pp.983-986.

Kumar, S., Nehra, M., Dilbaghi, N., Tankeshwar, K. and Kim, K.H., 2018. Recent Advances and Remaining Challenges for Polymeric Nanocomposites in Healthcare Applications. Progress in Polymer Science.

Li, S., Thouless, M.D., Waas, A.M., Schroeder, J.A. and Zavattieri, P.D., 2005. Use of Mode-I Cohesive-Zone Models to Describe the Fracture of an Adhesively-Bonded Polymer-Matrix Composite. Composites of Science and Technology, 65(2), Pp.281-293.

Li, S., Thouless, M.D., Waas, A.M., Schroeder, J.A. and Zavattieri, P.D., 2006. Mixed-Mode Cohesive-Zone Models for Fracture of an Adhesively Bonded Polymer-Matrix Composite. Engineering Fracture Mechanics, 73(1), Pp.64-78.

Li, X.F. and Lee, K.Y., 2016. Fracture of a Thin Power-Law Nonlinear Material with a Crack Using the DCB Model. International Journal of Fracture, 201(1), Pp.119-125.

Li, W. and Siegmund, T., 2002. An Analysis of Crack Growth in Thin-Sheet Metal via a Cohesive Zone Model. Engineering Fracture Mechanics, 69(18), Pp.2073-2093.

Menard, E., 2005. Techniques D'impression et Matériaux Semiconducteurs Pour L'électronique Plastique (Doctoral Dissertation, Université Pierre et Marie Curie-Paris VI).

Mittal, K.L., 2012. Adhesive Joints: Formation, Characteristics, and Testing. Springer Science & Business Media.

Nitya, G., Nair, G.T., Mony, U., Chennazhi, K.P. and Nair, S.V., 2012. In Vitro Evaluation of Electrospun PCL/Nanoclay Composite Scaffold for Bone Tissue Engineering. Journal of Materials Science: Materials in Medicine, 23(7), Pp.1749-1761.

Park, S.Y., Choi, W.J., Choi, H.S., Kwon, H. and Kim, S.H., 2010. Recent Trends in Surface Treatment Technologies for Airframe Adhesive Bonding Processing: A Review (1995–2008). The Journal of Adhesion, 86(2), Pp.192-221.

Paul, D.R. and Robeson, L.M., 2008. Polymer Nanotechnology: Nanocomposites. Polymer, 49(15), Pp.3187-3204.

Rahman, A. and Wu, X.F., 2017. Computational Study of the Effects of Processing Parameters on the Nonlinear Elastoplastic Behavior of Polymer Nanoclay Composites. Journal of Composites Science, 1(2), p.16.

Roesler, J., Paulino, G.H., Park, K. and Gaedicke, C., 2007. Concrete Fracture Prediction Using Bilinear Softening. Cement and Concrete Composites, 29(4), Pp.300-312.

Schadler, L.S., Brinson, L.C. and Sawyer, W.G., 2007. Polymer Nanocomposites: A Small Part of the Story. Jom, 59(3), Pp.53-60.

Schapery, R.A. and Davidson, B.D., 1990. Prediction of Energy Release Rate for Mixed-Mode Delamination Using Classical Plate Theory. Applied Mechanics Reviews, 43(5S), Pp.S281-S287.

Shim, D.J., Paulino, G.H. and Dodds, R.H., 2006. J Resistance Behavior in Functionally Graded Materials Using Cohesive Zone and Modified Boundary Layer Models. International Journal of Fracture, 139(1), Pp.91-117.

Song, S.H., Paulino, G.H. and Buttlar, W.G., 2006. A Bilinear Cohesive Zone Model Tailored for Fracture of Asphalt Concrete Considering Viscoelastic Bulk Material. Engineering Fracture Mechanics, 73(18), Pp.2829-2848.

Song, S.H., Paulino, G.H. and Buttlar, W.G., 2006. Simulation of Crack Propagation in Asphalt Concrete Using an Intrinsic Cohesive Zone Model. Journal of Engineering Mechanics, 132(11), Pp.1215-1223.

Stefancu, A.I., Melenciuc, S.C. and Budescu, M., 2011. Penalty based Algorithms for Frictional Contact Problems. Buletinul Institutului Politehnic din lasi. Sectia Constructii, Arhitectura, 57(3), Pp.119.

Sun, C., Thouless, M.D., Waas, A.M., Schroeder, J.A. and Zavattieri, P.D., 2008. Ductile-Brittle Transitions in the Fracture of Plastically-Deforming, Adhesively-Bonded Structures. Part I: Experimental Studies. International Journal of Solids and Structures, 45(10), Pp.3059-3073.

Sundararaman, V. and Davidson, B.D., 1997. An Unsymmetric Double Cantilever Beam Test for Interfacial Fracture Toughness Determination. International Journal of Solids and Structures, 34(7), Pp.799-817.

Suo, Z. and Hutchinson, J.W., 1990. Interface Crack between Two Elastic Layers. International Journal of Fracture, 43(1), Pp.1-18.

Thouless, M.D., Adams, J.L., Kafkalidis, M.S., Ward, S.M., Dickie, R.A. and Westerbeek, G.L., 1998. Determining the Toughness of Plastically Deforming Joints. Journal of Materials Science, 33(1), Pp.189-197.

Tjong, S.C., 2006. Structural and Mechanical Properties of Polymer Nanocomposites. Materials Science and Engineering: R: Reports, 53(3-4), Pp.73-197.

Tsai, J. and Sun, C.T., 2004. Effect of Platelet Dispersion on the Load Transfer Efficiency in Nanoclay Composites. Journal of Composite Materials, 38(7), Pp.567-579.

Tucker III, C.L. and Liang, E., 1999. Stiffness Predictions for Unidirectional Short-Fiber Composites: Review and Evaluation. Composites Science and Technology, 59(5), Pp.655-671.

Turon, A., Camanho, P., Costa, J. and Silva, C.G., 2006. A Damage Model for the Simulation of Delamination in Advanced Composites under Variable-Mode Loading. Mechanics of Materials, 38(11), Pp.1072-1089.

Usuki, A., Kojima, Y., Kawasumi, M., Okada, A., Fukushima, Y., Kurauchi, T. and Kamigaito, O., 1993. Synthesis of Nylon 6-Clay Hybrid. Journal of Materials Research, 8(5), Pp.1179-1184.

Xu, X.P. and Needleman, A., 1994. Numerical Simulations of Fast Crack Growth in Brittle Solids. Journal of Mechanics and Physics of Solids, 42(9), Pp.1397-1434.

Wang, J. and Qiao, P., 2005. Analysis of Beam-Type Fracture Specimens with Crack-Tip Deformation. International Journal of Fracture, 132(3), Pp.223-248.

Weon, J.I. and Sue, H.J., 2005. Effects of Clay Orientation and Aspect Ratio on Mechanical Behavior of Nylon-6 Nanocomposite. Polymer, 46(17), Pp.6325-6334.

Williams, J.G., 1998. Friction and Plasticity Effects in Wedge Splitting and Cutting Fracture Tests. Journal of Materials Science, 33(2), Pp.5351-5357.

Worlton, D.C., 1961. Experimental Confirmation of Lamb Waves at Megacycle Frequencies. Journal of Applied Physics, 32(6), Pp.967-971.

Wu, X.F. and Jenson, R.A., 2011. Stress-Function Variational Method for Stress Analysis of Bonded Joints under Mechanical and Thermal Loads. International Journal of Engineering Science, 49(3), Pp.279-294.

Wu, X.F. and Jenson, R.A., 2014. Semianalytic Stress-Function Variational Approach for the Interfacial Stresses in Bonded Joints. Journal of Engineering Mechanics, 140(11), p.04014089.

Wu, X.F., Jenson, R.A. and Zhao, Y., 2014. Stress-Function Variational Approach to the Interfacial Stresses and Progressive Cracking in Surface Coatings. Mechanics of Materials, 69(1), Pp.195-203.

Wu, X.F. and Yarin, A.L., 2013. Recent Progress in Interfacial Toughening and Damage Self-healing of Polymer Composites Based on Electrospun and Solution-blown Nanofibers: An Overview. Journal of Applied Polymer Science, 130(4), Pp.2225-2237.

Yang, Q.D. and Thouless, M.D., 1999. Reply to 'Comments on "Determining the Toughness of Plastically Deforming Joints"'. Journal of Materials Science Letters, 18(24), Pp.2051-2053.

Yang, Q.D., Thouless, M.D. and Ward, S.M., 1999. Numerical Simulations of Adhesively-Bonded Beams Failing with Extensive Plastic Deformation. Journal of the Mechanics and Physics of Solids, 47(6), Pp.1337-1353.

Yang, Q.D., Thouless, M.D. and Ward, S.M., 2000. Analysis of the Symmetrical 90-Peel Test with Extensive Plastic Deformation. The Journal of Adhesion, 72(2), Pp.115-132.